

**THE MICROSTRUCTURE OF DENSE PROTEIN SYSTEMS  
IN BIOPHARMACEUTICAL APPLICATIONS**

by

Stijn H. S. Koshari

A dissertation submitted to the Faculty of the University of Delaware in partial fulfillment of the requirements for the degree of Doctor of Philosophy in Chemical Engineering

Fall 2018

© 2018 Stijn H. S. Koshari  
All Rights Reserved

**THE MICROSTRUCTURE OF DENSE PROTEIN SYSTEMS  
IN BIOPHARMACEUTICAL APPLICATIONS**

by

Stijn H. S. Koshari

Approved: \_\_\_\_\_  
Eric M. Furst, Ph.D.  
Chair of the Department of Chemical and Biomolecular Engineering

Approved: \_\_\_\_\_  
Levi T. Thompson, Ph.D.  
Dean of the College of Engineering

Approved: \_\_\_\_\_  
Douglas Doren, Ph.D.  
Interim Vice Provost for Graduate & Professional Education

I certify that I have read this dissertation and that in my opinion it meets the academic and professional standard required by the University as a dissertation for the degree of Doctor of Philosophy.

Signed:

---

Norman J. Wagner, Ph.D.  
Professor in charge of dissertation

I certify that I have read this dissertation and that in my opinion it meets the academic and professional standard required by the University as a dissertation for the degree of Doctor of Philosophy.

Signed:

---

Abraham M. Lenhoff, Ph.D.  
Professor in charge of dissertation

I certify that I have read this dissertation and that in my opinion it meets the academic and professional standard required by the University as a dissertation for the degree of Doctor of Philosophy.

Signed:

---

Eric M. Furst, Ph.D.  
Member of dissertation committee

I certify that I have read this dissertation and that in my opinion it meets the academic and professional standard required by the University as a dissertation for the degree of Doctor of Philosophy.

Signed:

---

Yun Liu, Ph.D.  
Member of dissertation committee

I certify that I have read this dissertation and that in my opinion it meets the academic and professional standard required by the University as a dissertation for the degree of Doctor of Philosophy.

Signed:

---

Christopher J. Roberts, Ph.D.  
Member of dissertation committee

I certify that I have read this dissertation and that in my opinion it meets the academic and professional standard required by the University as a dissertation for the degree of Doctor of Philosophy.

Signed:

---

Isidro E. Zarraga, Ph.D.  
Member of dissertation committee

## ACKNOWLEDGMENTS

Come here and let me tell you all, the story of a boy, who growing up in a magical land, was timid though had joy. Despite his inner silence and sarcasm besides, there were those who stayed with him, throughout the struggles of life's strides. In his youth he had the luck of stumbling on a Nymph godsend, a girl who laughed and talked and talked, and hence made him a lifelong friend. Then there was a Vampire, a false disciple of sin, but who always had twinkling eyes and truly a pure heart within. Last he met a Manticore, a philosopher of the mind, who traveled around and disappeared, always hard to find. He adventured with them all throughout the land to learn and laugh and grieve, but at some point the boy had to learn more and so he had to leave.

One day he packed his bags and fared across the rising seas, where he landed on a distant shore and crossed the beach with unease. He fell there in the sparkling sand and felt quite all alone, he missed his family and his friends who were waiting for him at home. His Mother and his Father, who always cared for him with love and pride, and his Brother and Sister who, though annoying, kept his heart occupied. But then two Wise Men came along and gave him each a hand, and with a good look up and down, pulled him out of the rough sand. One of them smiled reassuringly and cracked a scientific joke, while the other laughed jovially and created mysterious smoke. They brought him along and introduced him into their Guilds of magic, where their disciples tried to cure the world of all that's wrong and tragic. Welcomed among their inner ranks he joined to become somewhat wise, and hence they sent him on an

epic quest to find a secret prize. He traversed the newfound continent in search of the Institute of old, where he expected to find the ancient artifact of which he was told. Once he reached his destination two Titans came suddenly forth, and they taught him that the artifact simply stands for knowing what you're worth.

Back at the Guilds he realized soon he was on route to what he sought, but he still missed something in his life, which made him feel distraught. Then out of thin air quite unexpectedly a Fairy Godmother appeared, and she brought him to her Society of Stars where the eternal celestial motions were revered. He noticed dancing among the Stars the brightest of all there, a Seraph shining fiery light, radiating beauty everywhere. He feared he had to vanquish the two brave Guardians at her side, but they quickly ridiculed his nervousness and smilingly let him approach his future bride. A soft tremble and then music, fire, flowers, rainbows of explosions in the sky, one soul, one love, one destiny, that merge and mystify. The silly boy didn't know what happened here, maybe he went insane, but dancing in each other's arms they ascended from the earthen plane.

My deepest gratitude for the help, love, and support of the following people:

- The Nymph, Vampire, and Manticore: my lifelong friends, Melina Sève, Maxim De Schepper, and Pierre Hansquine, and all others who have accompanied me
- The Mother, Father, Brother, and Sister: my parents and siblings, Leen Coosemans and Reza, Yonas, and Esther Koshari, and the rest of my family, I left but you are always with me
- The Wise Men and their Guilds: my advisers Norm Wagner and Bramie Lenhoff, and the Wagner and Lenhoff research groups, in particular Simon Rogers, Dan Greene, and Ohnmar Khanal for their help and companionship
- The Titans at the Institute: my managers during my internship at Genentech, Karthik Rajagopal and Dan Zarraga, mentors throughout my project
- The Fairy Godmother and the Society of Stars: Pat Grim and all the members of the University of Delaware Ballroom Dance Team, a home away from home
- The Guardians: my newfound friends, Kelly Burke and Naomi Chang, and the rest of the gang (including *all* the Kevins)
- The Seraph: my wife, Mitali Desai

I would like to thank Jean Ross for her help with microscopy, Daniel Ferraro for his help with implementing the PTA algorithm and performing simulations, and Debby Chang and Purnendu Nayak for preparing samples and all the thoughtful discussions. I would also like to thank the various instrument scientists who guided me during neutron experiments, including Yun Liu, Katie Weigandt, Paul Butler, and Ron Jones. Genentech is gratefully acknowledged for their financial support and for providing the monoclonal antibodies, fragment antibodies, and PLGA rods used throughout this work, and Amgen is gratefully acknowledged for donating the monoclonal antibody used in Chapter 2. The work in Chapter 2 was supported by the National Science Foundation under Agreement No. CBET-1263966. The support of the National Institute of Standards and Technology, U.S. Department of Commerce, is acknowledged in providing the neutron research facilities used in this work. This work utilized neutron facilities supported in part by the National Science Foundation under Agreement No. DMR-0944772. Gel permeation chromatography equipment was supported by the Delaware COBRE program, with a grant from the National Institute of General Medical Sciences – NIGMS (1 P30 GM110758-01) from the National Institutes of Health. Microscopy access was supported by grants from the NIH-NIGMS (P20 GM103446), the NSF (IIA-1301765), and the State of Delaware. Microscopy equipment was acquired with the Delaware INBRE Grant P20 GM103446.

## TABLE OF CONTENTS

LIST OF TABLES .....	xiii
LIST OF FIGURES .....	xvi
ABSTRACT .....	xxiii

### Chapter

1	BACKGROUND AND INTRODUCTION .....	1
1.1	Rise of the Biopharmaceutical Industry .....	1
1.2	Monoclonal Antibody Products.....	3
1.3	Dense Protein Systems .....	4
1.4	Dissertation Objectives and Outline.....	6
2	EFFECTS OF RESIN ARCHITECTURE AND PROTEIN SIZE ON NANOSCALE PROTEIN DISTRIBUTION IN ION-EXCHANGE MEDIA	10
2.1	Introduction .....	10
2.2	Experimental Section.....	13
2.2.1	Materials .....	13
2.2.1.1	Buffers .....	13
2.2.1.2	Protein Solutions .....	13
2.2.1.3	Chromatographic Media.....	14
2.2.1.4	Sample Preparation.....	15
2.2.1.5	Sample Compositions.....	16
2.2.2	Methods .....	18
2.2.2.1	Small-Angle Neutron Scattering .....	18
2.2.2.2	Structural Models .....	20
2.2.2.3	Protein Form Factors .....	23
2.2.2.4	Model Fitting of Neat Resins .....	25
2.2.2.5	Model Fitting of Protein-Laden Resins .....	26
2.3	Results and Discussion .....	26
2.3.1	Scattering Patterns of Neat Resins .....	27

2.3.2	Nano-to-Mesoscale Architecture of Neat Resins .....	29
2.3.3	Scattering Patterns of Protein-Laden Resins .....	32
2.3.4	Protein Distribution in S HyperCel .....	38
2.3.5	Protein Distribution in Sepharose FF and XL .....	41
2.3.6	Protein Distribution in Capto S .....	43
2.4	Conclusions .....	44
3	<b>CHARACTERIZATION OF PROTEIN-EXCIPIENT MICROHETEROGENEITY IN BIOPHARMACEUTICAL SOLID- STATE FORMULATIONS BY CONFOCAL FLUORESCENCE MICROSCOPY .....</b>	<b>45</b>
3.1	Introduction .....	45
3.2	Materials and Methods .....	49
3.2.1	Materials .....	49
3.2.2	Conjugation with Fluorescent Dye .....	50
3.2.3	Spray-Drying .....	51
3.2.4	Lyophilization.....	51
3.2.5	Moisture Content Determination .....	52
3.2.6	Size-Exclusion Chromatography.....	52
3.2.7	Scanning Electron Microscopy.....	53
3.2.8	Confocal Fluorescence Microscopy .....	53
3.3	Results .....	54
3.4	Discussion.....	59
3.5	Conclusions .....	63
4	<b><i>IN SITU</i> CHARACTERIZATION OF THE MICROSTRUCTURAL EVOLUTION OF BIOPHARMACEUTICAL SOLID-STATE FORMULATIONS WITH IMPLICATIONS FOR PROTEIN STABILITY ..</b>	<b>64</b>
4.1	Introduction .....	64
4.2	Experimental Section.....	68
4.2.1	Materials and Sample Preparation.....	68
4.2.2	Small-Angle Neutron Scattering .....	69
4.2.3	Vapor Cell .....	71
4.3	Results and Discussion .....	72
4.3.1	Static Microstructure .....	73
4.3.2	Microstructural Changes under Cyclic Humidification .....	75

4.3.3	Comparison between mAbs and Fabs .....	82
4.3.4	Comparison between Lyophilization and Spray-Drying.....	84
4.3.5	Relation between Microstructural Changes and Aggregation.....	85
4.4	Conclusions .....	89
5	DATA-DRIVEN DEVELOPMENT OF PREDICTIVE MODELS FOR SUSTAINED DRUG RELEASE .....	91
5.1	Introduction .....	91
5.2	Methodology.....	94
5.2.1	Mathematical Model.....	94
5.2.2	Experimental Data .....	98
5.2.3	Parallel Tempering Algorithm.....	98
5.2.4	Implementation.....	99
5.3	Results and Discussion .....	101
5.3.1	Detecting Overfitting.....	101
5.3.2	Critical Parameters and Model Sensitivity .....	105
5.3.3	Model Predictions.....	107
5.4	Conclusions .....	111
6	DESIGN OF SUSTAINED RELEASE BIOPHARMACEUTICAL SYSTEMS THROUGH MODEL PREDICTIONS .....	113
6.1	Introduction .....	113
6.2	Materials and Methods .....	116
6.2.1	Materials .....	116
6.2.2	Mixed Solvent Depot Preparation .....	117
6.2.3	Rod Design .....	118
6.2.4	Spray-Drying and Characterization of FITC-Dextran.....	120
6.2.5	Extrusion of Rods .....	121
6.2.6	Experimental Setup of Rods .....	122
6.2.7	Measurement of Drug Release from Rods .....	122
6.2.8	Water Uptake and Rod Erosion Measurements.....	123
6.2.9	Polymer Degradation by Gel Permeation Chromatography.....	124
6.2.10	Confocal Fluorescence Microscopy .....	124
6.3	Results and Discussion .....	125

6.3.1	Designing a Linear Release Profile .....	125
6.3.2	Predicting the Release of PLGA Rods .....	132
6.3.3	Experimental Results for the PLGA Rods.....	134
6.3.4	Relation between Rod Microstructure and First-Phase Release	140
6.3.5	Capturing First-Phase Release.....	148
6.4	Conclusions .....	150
7	CONCLUSIONS AND RECOMMENDATIONS.....	152
	BIBLIOGRAPHY .....	157
Appendix		
A	SMALL-ANGLE NEUTRON SCATTERING DATA FOR PROTEIN ADSORPTION ON CHROMATOGRAPHIC RESINS .....	172
A.1	Selection of Structural Models .....	172
A.2	Model Fitting Ranges in Protein-Laden Resins.....	173
A.3	Model Parameters in Protein-Laden Resins .....	173
A.4	Protein Contribution in Protein-Laden Resins .....	174
A.5	Low- <i>Q</i> Upturn in Protein-Laden Resins.....	175
B	CONFOCAL FLUORESCENCE MICROSCOPY IMAGES OF ADDITIONAL SAMPLES .....	184
C	FULL-RANGE SMALL-ANGLE NEUTRON SCATTERING PATTERNS FOR SOLID-STATE FORMULATIONS IN A VAPOR CELL.....	186
D	OPTIMAL PARAMETER VALUES FOR PARALLEL TEMPERING ALGORITHM .....	189
E	PERMISSIONS .....	191
E.1	Chapter 2 Reprint Permission.....	191
E.2	Chapter 3 Reprint Permission.....	192

## LIST OF TABLES

Table 2.1:	Fitting parameters of the generalized Guinier-Porod model and fitting values for neat and protein-laden S HyperCel.....	28
Table 2.2:	Fitting parameters of the polydisperse cylinder model and fitting values for neat agarose-based resins. ....	29
Table 2.3:	Peak positions in the scattering patterns of the protein monomer contributions.....	38
Table 3.1:	Overview of the composition and process conditions of the samples investigated.....	50
Table 4.1:	Overview of the composition and process conditions of the formulations investigated. ....	69
Table 4.2:	Overview of SANS peak positions for mAb and Fab formulations. The characteristic distance is estimated from the $q$ -value using Bragg's law (Equation 2.4). ....	81
Table 5.1:	Mathematical model parameters and initial fitting values for the microsphere data set. Parameters in grey are held constant during fitting of the parallel tempering algorithm (PTA). ....	97
Table 5.2:	Optimal parameter values and corresponding objective functions for the mathematical model fit to the microsphere data set, as obtained from six different runs of the PTA. Red and green highlights indicate the range of the objective function values.....	103
Table 5.3:	P-values for the hypothesis that there is no correlation between the different pairs of model parameters for the microsphere data, based on six PTA runs (Table 5.1). For the bold values in red, the corresponding parameter correlation is considered significant. ....	104
Table 5.4:	P-values for the hypothesis that there is no correlation between the different model parameters for the solvent depot data, based on twelve PTA runs with five fitted parameters (Table D.2 in Appendix D). For the bold values in red, the corresponding parameter correlations are considered significant.....	108

Table 5.5:	Optimized parameter values as obtained by simultaneous fitting of the solvent depot data by the PTA. Parameter values in grey are held constant during fitting, bold parameter values in red are fitted independently, and italicized parameter values in green are fitted simultaneously across the different initial PLGA MWs. ....	111
Table 6.1:	Solvent depot formulation compositions, weight- and number-averaged molecular weights ( $MW_w$ and $MW_n$ ), polydispersity indices ( $MW_w/MW_n$ , PDI), and glass transition temperatures ( $T_g$ ). MW and PDI values were determined at Genentech using gel permeation chromatography. ....	118
Table 6.2:	PLGA rod design parameters for nine different formulations. Bold values in red indicate variations from the reference formulation A. ....	119
Table 6.3:	PLGA grades used for each of the nine different formulations. Grades in red italics indicate variations from the reference formulation A. ....	120
Table 6.4:	Model parameters to obtain linear release profiles in solvent depot systems. Bold values in green were fit with the parallel tempering algorithm, while italic values in blue were adjusted manually. ....	128
Table 6.5:	Initial model parameters to predict PLGA rod behavior for the nine formulations. Bold values in red indicate variations from the reference formulation A. ....	133
Table 6.6:	Modified model parameter values to capture first-phase release and differences in PLGA grade in the nine rod formulations. Bold values in red indicate variations from the initial values in Table 6.5. ....	149
Table A.1:	Fitting parameters of the generalized Guinier-Porod model and fitting values for neat and protein-laden S HyperCel. Lower and upper limits of the fitting range are also included. Values that were held fixed during fitting are indicated by an asterisk. ....	180
Table A.2:	Fitting parameters of the polydisperse cylinder model and fitting values for neat and protein-laden SP Sepharose FF. Lower and upper limits of the fitting range are also included. Values that were held fixed during fitting are indicated by an asterisk. ....	181
Table A.3:	Fitting parameters of the polydisperse cylinder model and fitting values for neat and protein-laden SP Sepharose XL. Lower and upper limits of the fitting range are also included. Values that were held fixed during fitting are indicated by an asterisk. ....	182

Table A.4:	Fitting parameters of the polydisperse cylinder model and fitting values for neat and protein-laden Capto S. Lower and upper limits of the fitting range are also included. Values that were held fixed during fitting are indicated by an asterisk.....	183
Table D.1:	Optimal parameter values and corresponding objective functions for the mathematical model fit to the solvent depot data set when seven parameters are fit, as obtained from twenty different runs of the PTA. Red and green highlights indicate the range of the objective function values.....	189
Table D.2:	Optimal parameter values and corresponding objective functions for the mathematical model fit to the solvent depot data set when five parameters are fit, as obtained from twelve different runs of the PTA. Red and green highlights indicate the range of the objective function values.....	190

## LIST OF FIGURES

- Figure 2.1: Adsorbed protein concentrations in the chromatographic media as a function of supernatant concentration. The labels indicate the approximate total ionic strength (TIS) of each sample. .... 17
- Figure 2.2: Scattering patterns of protein solutions at low concentrations (approximately 5 mg/mL), showing the characteristic scattering pattern of protein monomers, *i.e.*, the protein form factor. CRYSON scattering predictions from protein PDB files are shown by the dashed lines. Successive curves are offset by a factor of 4 for clarity. .... 24
- Figure 2.3: Scattering patterns of neat chromatographic media at 50 mM total ionic strength. Model fits are shown in the dashed lines. Successive curves are offset by a factor of 4 for clarity. .... 28
- Figure 2.4: Overview of the inferred sorption behavior as a function of resin architecture and protein size. In this work, lysozyme is considered a small protein and lactoferrin and mAbs are considered large proteins. .. 32
- Figure 2.5: Scattering patterns of protein-sorbed chromatographic media at an approximate total ionic strength of 50 mM. Error bars are generally smaller than the symbol size. Successive curves are offset by a factor of 4. Structural model fits are shown by the dashed lines, and were fit only to the background scattering and the low- $Q$  region, up to the  $Q$ -value where the presence of the protein caused an inflection in the scattering pattern, typically around  $0.03 \text{ \AA}^{-1}$ . Specific fitting ranges are included in Appendix A..... 33
- Figure 2.6: Cylinder radii of protein-laden agarose-based resins obtained by fitting SANS data to the polydisperse cylinder model. The labels indicate the approximate total ionic strength of each sample. The gray lines indicate the cylinder radii obtained for the neat media, while the colored dashed lines indicate the expected core radius if a uniform layer of protein adsorbs. .... 35

- Figure 2.7: Cylinder scattering length densities (SLDs) as obtained from fitting SANS data to the polydisperse cylinder model. The labels indicate the approximate total ionic strength of each sample. The gray lines indicate the SLD of pure D<sub>2</sub>O and the approximate SLD of protein and agarose in the sample solvent. Note that the core SLD for the neat media is the value for agarose, as indicated in the figures. .... 35
- Figure 2.8: Scattering patterns of protein-sorbed chromatographic media after subtraction of the low-*Q* model fit, at an approximate total ionic strength of 50 mM. The resulting scattering intensity is due to the presence of protein monomers. The predicted scattering intensity due purely to the protein form factor is shown by the dashed lines. The vertical lines show the position of peaks or shoulders in the scattering data, where the difference between the experimental data and the predicted form factor data is generally the highest. These lines are at the same *Q*-values in each panel. The black diamonds indicate the *Q*-value below which subtraction effects and artifacts become considerable. Error bars due to instrument error are generally smaller than the symbol size. Successive curves are offset by a factor of 4 for clarity. .... 37
- Figure 2.9: Illustration of the effect of protein sorption on the measured radius of an effective cylinder as a function of protein size, assuming that proteins distribute in a monolayer around the resin strands (Figure 2.4, center left). Protein structures were drawn merely for illustration using PyMOL [75] from the same PDB files used for the CRYSON form factor calculations. .... 42
- Figure 3.1: Typical scanning electron microscopy (SEM) images for spray-dried and lyophilized biotherapeutics. The top row shows SEM images of (a) a spray-dried powder and (b) a lyophilized powder as received, while the bottom row shows cross-sections of the same formulations after embedding in an acrylic resin. While formulations with Fab1 and a trehalose-to-protein ratio of 1 were used in all the images shown, mAb1 formulations showed similar morphologies. .... 55

Figure 3.2:	Confocal fluorescence microscopy (CFM) images of two spray-dried (top and middle) mAb1 formulations and a lyophilized (bottom) mAb1 formulation with trehalose-to-protein ratios (S/P) of 1 (top) and 10 (middle and bottom). The mAb1 protein in each formulation was conjugated to Alexa Fluor 488 dye with a labeling ration of 1%. The images on the left (a, e, and g) contain maximum-intensity projections of the full three-dimensional image stacks, while the images towards the right (b, c, d, f, and h) contain single cross-sections. The red dashed lines delineate the intensity profiles shown in the corresponding panels in Figure 3.3. ....	57
Figure 3.3:	CFM intensity line profiles for the cross-section of two spray-dried mAb-trehalose particles with varying S/P (top) and for a lyophilized, flake-like mAb-trehalose particle parallel and perpendicular to the flake (bottom). The profile lines are shown in Figure 3.2 as red dashed lines, which show the cross-sections of the particles at the approximate particle center (corresponding to a depth of 0 $\mu\text{m}$ ). All distances are reported as measured from the approximate particle center. For the spray-dried particles, the profile at different particle depths is shown, representing the three-dimensional particle structure. .	58
Figure 4.1:	Schematic of the neutron scattering length densities (SLDs) of a typical mAb, sucrose, fully deuterated sucrose, and water as a function of the amount of deuterium exchange of exchangeable hydrogens of each molecule. ....	70
Figure 4.2:	Schematic of the vapor cell set-up employed at the NCNR. ....	72
Figure 4.3:	Comparison of SANS patterns of a lyophilized mAb1 sample in regular (F1) and deuterated (F2) sugar (a) and overview of prominent scattering metrics reported in the time-resolved experiments (b). Open symbols show the scattering patterns before subtraction of the incoherent scattering background, while filled symbols show the patterns after subtraction. The dashed box indicates the area of the pattern highlighted in the time-resolved vapor cell experiments (Figure 4.4). ....	74
Figure 4.4:	Evolution of the SANS pattern of lyophilized mAb1 in deuterated sucrose (F2) as a function of time under cycles of alternating nitrogen and water vapor flows. The arrows on the scattering patterns indicate the general trend of the scattering pattern with time. A video of the evolution of the SANS pattern with time can be found online [100]. ....	78

Figure 4.5: Evolution of prominent scattering features of three formulations as a function of time under cycles of alternating nitrogen and water vapor flows. ....	79
Figure 4.6: Overview of observed peak positions of lyophilized mAb in deuterated sugar (F2) with schematics of the corresponding hypothesized microstructures. The green line indicates the original peak position, while the blue line indicates the original background value. ....	80
Figure 4.7: Comparison of peak height evolution during exposure to vapor cell D <sub>2</sub> O flow for a regular (F1) and a heat-stressed lyophilized mAb sample (F3). The open symbols show the height of the monomer peak ( $q = 0.16 \text{ \AA}^{-1}$ ), while the filled symbols show the height of the cluster peak ( $q = 0.10 \text{ \AA}^{-1}$ ). These peak positions are indicated in the inset, which shows the evolution of the SANS patterns of Formulation F1 with time (compare to Figure 4.4). ....	86
Figure 4.8: Comparison of aggregate content before and after exposure to vapor cell conditions for a regular (F1) and heat-stressed lyophilized mAb sample (F3), as measured by size-exclusion chromatography after reconstitution of the solid-state powders. ....	89
Figure 5.1: Model fitting of the drug release model to experimental, cumulative release data of lysozyme-loaded PLGA microspheres [124]. ....	102
Figure 5.2: Model fitting of the drug release model to experimental data of PLGA solvent depots with initial molecular weight (MW) of 41 kDa [91]: (a) cumulative drug release, (b) polymer degradation, and (c) water uptake. ....	106
Figure 5.3: Predictions (dashed blue) and simultaneous fits (solid red) of the drug release model to experimental data of PLGA solvent depots with initial MW of 10 kDa (panel a and c) and 56 kDa (panel b and d) [91]: (a-b) cumulative drug release and (c-d) polymer degradation. ....	109
Figure 6.1: Comparison between the desired release profile, which is linear (zeroth-order) over a period of 100 days (black symbols and dashed line), and the optimized release profile obtained from a fit of the model and parallel tempering algorithm (red solid line). The actual experimental design (blue dotted line) is based on the design principles of the optimal fit but is limited by the PLGA polymers available for this study. ....	126

Figure 6.2: Comparison between model predictions (dashed lines) and experimental data (closed symbols) for the mixed PLGA solvent depot system with varying mass fraction compositions of the pure PLGAs (pure PLGA release shown in open symbols). The lines connecting the symbols are a guide to the eye. Error bars indicate the standard deviation. ....	131
Figure 6.3: Initial model predictions for the cumulative drug release of the nine formulations.....	134
Figure 6.4: Experimental data for the PLGA rod system, including drug release, remaining rod mass, PLGA MW, PDI, and water uptake at two different scales. The lines connecting the symbols are a guide to the eye. Error bars indicate the standard deviation. ....	136
Figure 6.5: Comparison between model predictions (dashed blue lines) and experimental data (symbols) for the PLGA rods that exhibited apparent complete release. The experimental cumulative drug release was scaled to reach complete release (1.0) after 15 weeks. Model results with modified parameter values based on observed phenomena are shown by the red lines. ....	138
Figure 6.6: Comparison between model predictions (dashed blue lines) and experimental data (symbols) for the PLGA rods that exhibited incomplete release. Model results with modified parameter values based on observed phenomena are shown by the red lines. ....	140
Figure 6.7: Detail of a CFM cross-section of the reference formulation (A), showing the distribution of spray-dried FITC-dextran particles. The inset shows a binary transformation of the whole cross-section used to determine the particle fraction, where black represents the particles....	142
Figure 6.8: Comparison between FITC-dextran particle distributions in the nine rod formulations at Day 0. For formulation B, the lower section of the rod is out of focus. ....	143
Figure 6.9: Relation between the particle volume fraction, as measured from the cross-sectional images, and the amount of first-phase release for the nine rod formulations. Note that the volume fraction here does not take into account the fact that most particles are hollow. The formulations using the same PLGA grade as the reference formulation are shown by blue circles, while formulations using other PLGA grades are shown by red squares. ....	145

Figure 6.10: Comparison among particle distributions in the formulations with different amounts of drug loading. The blue dotted boxes indicate the presence of macroscopic pores in the rods, while the red dashed boxes show the positions of the images in Figure 6.11. ....	146
Figure 6.11: Comparison between the maximum-intensity projections of the particle distribution in the reference formulation (A) at Day 0 and Week 7. ....	147
Figure A.1: Scattering patterns of neat and protein-laden S HyperCel. Error bars are generally smaller than the symbol size. Successive curves are offset by a factor of 4. Structural model fits are shown by the dashed lines, and were fit only to the background scattering and the low- $Q$ region, up to the $Q$ -value where the presence of the protein caused an inflection in the scattering pattern. Specific fitting ranges are included in Table A.1. ....	176
Figure A.2: Scattering patterns of neat and protein-laden SP Sepharose FF. Error bars are generally smaller than the symbol size. Successive curves are offset by a factor of 4. Structural model fits are shown by the dashed lines, and were fit only to the background scattering and the low- $Q$ region, up to the $Q$ -value where the presence of the protein caused an inflection in the scattering pattern. Specific fitting ranges are included in Table A.2. ....	177
Figure A.3: Scattering patterns of neat and protein-laden SP Sepharose XL. Error bars are generally smaller than the symbol size. Successive curves are offset by a factor of 4. Structural model fits are shown by the dashed lines, and were fit only to the background scattering and the low- $Q$ region, up to the $Q$ -value where the presence of the protein caused an inflection in the scattering pattern. Specific fitting ranges are included in Table A.3. ....	178
Figure A.4: Scattering patterns of neat and protein-laden Capto S. Error bars are generally smaller than the symbol size. Successive curves are offset by a factor of 4. Structural model fits are shown by the dashed lines, and were fit only to the background scattering and the low- $Q$ region, up to the $Q$ -value where the presence of the protein caused an inflection in the scattering pattern. Specific fitting ranges are included in Table A.4. ....	179

Figure B.1: Maximum-intensity projections of the CFM image stacks for one Fab1 and five mAb1 formulations. Spray-dried formulations show protein-excipient microheterogeneity, while freeze-dried particles show homogeneous distribution. ....	185
Figure C.1: Full $q$ -range SANS patterns of a lyophilized mAb in deuterated sucrose (Formulation F2) as a function of time under cycles of alternating nitrogen and water vapor flows. ....	187
Figure C.2: Full $q$ -range SANS patterns of a spray-dried Fab in trehalose (Formulation F5) as a function of time under alternating nitrogen and water vapor flows. ....	188

## ABSTRACT

Dense protein systems are ubiquitous in biopharmaceutical processing but, while their microstructure plays a major role in the understanding of their structure-function relationships in biotherapeutic applications, microstructural characterization of these crowded, solid-like systems can be challenging. Here, we develop new methodologies and techniques to characterize the multiscale structure of dense protein systems, which are then used to understand fundamental problems in three general areas of the biopharmaceutical industry: separations, formulation, and drug delivery.

In separations, we characterize the effect of the architecture of cellulose-based and traditional and dextran-modified agarose-based ion-exchange resins on the nanoscale distribution of a relatively small protein (lysozyme) and two larger proteins (lactoferrin and a monoclonal antibody) at different protein loadings. We show that different resins lead to distinct protein distributions on protein-size length scales which are smaller than those previously observed *in situ*. Based on the data we propose that entropic partitioning effects such as depletion forces may drive the observed protein crowding. Our observations of the nano-scale structure are fundamental in understanding the mechanism of protein partitioning in different classes of chromatographic materials, providing necessary information for designing resins with improved performance.

In formulation, we demonstrate the use of confocal fluorescence microscopy with fluorescently-labeled monoclonal antibodies (mAbs) and antibody fragments (Fabs) to directly visualize three-dimensional particle morphologies and protein

distributions in dried biopharmaceutical formulations, without restrictions on processing conditions or the need for extensive data analysis. Moreover, small-angle neutron scattering with a humidity control environment was used to characterize protein-scale microstructural changes in such solid-state formulations as they were humidified and dried *in situ*. The findings indicate that irreversible protein aggregates of stressed formulations do not form within the solid-state, but do emerge upon reconstitution of the formulation. After plasticization of the solid-state matrix by exposure to humidity, the formation of reversibly self-associating aggregates can be detected *in situ*. The characterization of the protein-scale microstructure in these solid-state formulations facilitates further efforts to understand the underlying mechanisms that promote long-term protein stability.

In drug delivery, we developed a methodology to evaluate mathematical models for the prediction of sustained release from poly(lactic-co-glycolic acid)-based (PLGA) drug delivery systems. We show that a recently-developed, efficient stochastic optimization algorithm can be used not only to find global minima of such complex models robustly, but also to generate meta-data that allow quantitative evaluation of parameter sensitivity and correlation, which can be used for further model refinement and development. Furthermore, a predictive mathematical model was validated by (1) its use to design a desirable, zeroth-order release profile in injectable solvent depot release systems, and (2) the comparison between model predictions and experimental release data and microstructural observations for implantable solid rods. The novel observations for both experimental systems are essential for adequately describing the underlying drug-release mechanisms when designing predictive models such as the one evaluated here, and we directly illustrate

how such a predictive model facilitates the development of sustained drug-release systems.

In general, this dissertation highlights the broad range of phenomena that can influence dense protein systems, and emphasizes the value in bringing soft matter expertise to this field to better understand these systems. The tools and methods developed in this dissertation, including small-angle neutron scattering, confocal fluorescence microscopy, and mathematical modeling, will be invaluable in the study of the structure-function relationship of these and other dense protein systems throughout the biopharmaceutical field.

## Chapter 1

### BACKGROUND AND INTRODUCTION

*Here, in the humid momentary  
heat of summer's solstice  
I find my shadow self, and passion;  
throw off old cancer's green claim,  
dream, begin to be whole again.*

*Yes, night moves inside me,  
and I can set the stars in place.*

*In my tremor's pulse  
my hands know of themselves  
what they are doing.*

*Here, pink flowers speak to me  
by name. They open a valve  
in their soft-petalled mouths,  
whisper secrets of abandon,  
and singing, and*

*yes, even in my fingers and toes  
a new feeling is rising, an insistent urging  
sharply infused from below,  
a dark stem-colored flow.*

Charles Entrekin - *The Art of Healing* (2016)

#### 1.1 Rise of the Biopharmaceutical Industry

“Shalom,” read the sign on a delicatessen in Honolulu’s Waikiki Beach where, after a late-night walk in November 1972, medical professor Stanley Cohen and biochemist Herbert Boyer sketched out the experimental plan for an impromptu collaboration on some napkins from a dispenser [1,2]. A few months later, they

succeeded in inserting hybrid DNA fragments into a living organism, while retaining their biological functionality [3,4], and subsequently in producing eukaryotic DNA in bacteria [5], fundamental discoveries in genetic engineering. These achievements heralded the birth of modern biotechnology. In 1976, Herbert Boyer teamed up with venture-capitalist Robert Swanson to found a company focused on implementing recombinant DNA technology, Genentech Inc. (South San Francisco, CA), considered the first biopharmaceutical company in the traditional sense [2,6].

Soon, the production of hormones such as insulin and growth hormone launched biopharmaceuticals into the commercial market. Biopharmaceuticals have since grown into a major component of the pharmaceutical industry. In 2012, they represented 71% of the worldwide revenue generated by the ten top-selling pharmaceuticals, and total biopharmaceutical sales exceeded US\$ 125 billion worldwide [7,8]. By 2016 sales totaled US\$ 228 billion and by 2020 more than 50% of the 20 top-selling pharmaceuticals are expected to be biologics [9,10]. This growth has been fueled by the potential of these biotherapeutics to address previously unmet medical needs, resulting in the approval of several first-in-class, advance-in-class, and breakthrough designated therapeutics in the past few decades. Consequently, virtually all major pharmaceutical companies have picked up biotherapeutics as part of their product pipeline, with more than 200 approved biopharmaceuticals marketed in the United States (US) and/or European Union (EU) and more than 900 biopharmaceutical products currently in development [8,9]. These new products are expected to lead to a diversification of the biopharmaceutical marketplace, with a large number of product types on a reduced scale [11]. Rapid and adaptive change in several key areas of the biopharmaceutical industry will be necessary to accommodate this growth and

diversification, with accompanying challenges in expression, formulation, and delivery [6,11].

## **1.2 Monoclonal Antibody Products**

Initially, biotherapeutics were limited to products such as peptides and smaller recombinant therapeutic proteins. In 1986, the first therapeutic monoclonal antibody, Orthoclone OKT3, was approved for prevention of kidney transplant rejection [12]. Although sales growth was initially slow, development of monoclonal antibodies and their derivatives such as Fc-fusion proteins, antibody fragments, and antibody-drug conjugates continued and they subsequently became the fastest growing product class of biotherapeutics by the end of the 1990s [12,13]. Currently, antibody products dominate the biopharmaceutical industry, generating more than US\$ 90 billion in global sales from more than 80 approved products, with ten new antibody products approved in the US and EU in 2017 alone [12,14].

The prevalence of antibody products stems from their ability to target hard-to-treat conditions such as cancer, inflammatory disease, organ transplantation, cardiovascular disease, infection, respiratory disease, and ophthalmologic disease [15]. This efficacy of therapeutic antibodies is engineered during biopharmaceutical development based on the various natural functions of antibodies like neutralization, antibody-dependent cell-mediated cytotoxic (ADCC) activity, or complement-dependent cytotoxic (CDC) activity [15]. These natural functions are enabled by the macromolecular nature of antibodies, which gives them the structural complexity required to achieve high specificity and potency as compared to other proteins or small molecules.

However, this structural complexity also leads to several challenges in the development and production of antibody products and other biotherapeutics. In particular, monoclonal antibodies are prone to chemical and physical degradation, such as oxidation, deamidation, fragmentation, and aggregation, especially in response to environmental triggers such as moisture, temperature, or chemical composition [13]. This degradation can lead to loss of drug potency, formulation instability, and potential immunogenic side effects, which can threaten patient safety. Moreover, as antibodies must generally be administered in stoichiometric rather than catalytic quantities, large dosages of the drug are necessary [13]. The combination of high dosage and degradation mitigation makes the production, formulation, and delivery of biotherapeutics challenging [16].

The manufacturing process of monoclonal antibody products in the biopharmaceutical industry is generally divided in two main steps: upstream and downstream processing. Upstream processing refers to the step in which the biotherapeutics are produced in and harvested from bioreactors, after which they are transferred to downstream processing for recovery and purification. During downstream processing, the proteins are generally formulated in conditions suitable for storage and administration. However, to prevent degradation and reach sufficiently high dosages, formulations might have to be further modified after the purification process [17]. For example, monoclonal antibody products are sometimes dried to reach longer shelf-lives or incorporated in drug-delivery devices for sustained release.

### **1.3 Dense Protein Systems**

Throughout production, purification, formulation, and drug-delivery, antibody products can be present in highly concentrated, crowded morphologies that are

generally characterized as dense protein systems. Such systems include typical dense protein phases such as highly concentrated protein solutions, protein gels, and protein aggregates, but can also include more unconventional crowded protein morphologies such as frozen proteins, dried proteins, and protein-loaded particles. These dense systems typically arise from protein-protein interactions in solution, but can also be influenced by other factors such as physical processes (*e.g.*, drying and freezing) and protein-substrate interactions (*e.g.*, binding to a chromatographic column) [18,19]. Due to their inherently crowded nature, dense systems often exhibit solid or solid-like morphologies. Consequently, the microstructure of dense protein phases generally plays a major factor in their behavior in biopharmaceutical applications.

Depending on this behavior, dense systems can be either desirable or unwanted in biopharmaceutical processes. Examples of desirable dense protein systems include certain types of protein precipitates, which are used as an alternative to chromatography in mAb purification [20,21]; lyophilized mAbs, which can replace the typical liquid mAb formulations to extend shelf-life [22]; and mAb-loaded polymer particles, which can be used for sustained release for drug delivery [7]. However, relatively small changes in a dense system's structure or nature can make a large difference in its desirability. For example, during protein purification, crowded morphologies are beneficial to reach high loading volumes of proteins in chromatographic columns, but dense protein phases have also been implicated in reduced rates of elution from certain resins [23]. In other purification processes like crystallization and precipitation, it is important that the protein remains in its native state or that the process is reversible so that the biotherapeutic can be easily recovered [20,21]. In general, dense protein systems are problematic if they are induced by or

lead to the degradation of the biotherapeutic, such as in the formation of irreversible protein aggregates [16,24]. Because of the high concentrations and harsh environmental conditions, dense protein systems are often prone to such degradation events and, consequently, formulation and process conditions have to be tightly controlled, for example by adding certain excipients that stabilize the protein [16].

In all of these cases, microstructural characterization of these systems can help elucidate the mechanisms that lead to their properties and formation, ultimately allowing guided design of biopharmaceutical processes that lead to stable dense phases that are desirable while avoiding those that are unwanted. However, the characterization of dense, solid-like morphologies can be challenging. Many established techniques that are used to characterize typical biopharmaceutical formulations in solutions cannot be used on dense or solid systems. Moreover, dense phases can naturally arise within processing equipment or medical devices, where they are often in the presence of large amounts of other organic compounds, complicating *in situ* characterization. Consequently, a full, multiscale structural characterization of biopharmaceutical solid-state formulations, especially on molecular length scales, can help us understand fundamental mechanisms related to biopharmaceutical processes, but such a characterization is generally challenging to accomplish.

#### **1.4 Dissertation Objectives and Outline**

Three important, fundamental questions related to dense protein systems in the biopharmaceutical field have been identified:

1. how can the performance of chromatographic resins for protein separation be improved;
2. how can biopharmaceuticals be formulated to prevent drug degradation during handling, storage, and administration; and

3. how can biopharmaceuticals be delivered to the patient with optimal dosage while maintaining high patient compliance.

These questions span three key areas of the biopharmaceutical industry: separations, formulation, and drug delivery. The goal of this dissertation is to better understand the mechanisms that define the dense protein systems in each of these areas, through the development of new methodologies and techniques to characterize their multiscale structure. In general, the dense systems are recognized as complex materials and are investigated from a soft matter perspective with methodologies such as neutron scattering and modeling approaches that originate from soft matter applications. The techniques employed here, such as various forms of microscopy and small-angle neutron scattering, are particularly well-suited to study the structure-function relationship of these systems as they probe length scales that range from the size of the dense systems to the size of the protein molecules. Through the novel findings that arise from this work, we aim to promote the use of some of these soft matter approaches to the wider biopharmaceutical field.

Specific objectives can be found in each of the chapters of the dissertation, which are structured around the three investigated areas of biopharmaceutical processing. In general, with regard to separations, we aim to characterize the protein-scale structure of chromatographic resins used for the purification of biopharmaceutical proteins with small-angle neutron scattering (SANS) in Chapter 2. We aim to understand whether architectural differences on protein-size length scales in these resins can be probed by SANS *in situ*, as opposed to other structural characterization techniques such as electron microscopy that generally probe larger length scales and require additional sample preparation, and whether these

architectural differences affect the protein distribution and subsequent chromatographic performance.

With regard to formulation, Chapter 3 and Chapter 4 investigate the structure of solid-state protein formulations, which are often used to mitigate stability issues encountered by typical liquid formulations during storage and transport. However, underlying mechanisms and factors affecting the stability in these solid-state formulations are not yet fully understood [22]. We aim to understand how the stability is affected by the microstructure of the formulations. Specifically, in Chapter 3, we study the particle-scale structure of these formulations, particularly the relative distribution of protein and excipients, with a methodology developed around confocal fluorescence microscopy. The aim of this chapter is to determine if this particle-scale distribution is affected by the processing conditions of the drying method, and whether the distribution itself affects the long-term protein stability. Chapter 4, in contrast, documents a study of the protein-scale structure of these solid-state formulations using SANS, with the aim of understanding how proteins self-associate under changing environmental conditions in the solid state.

Lastly, with regard to drug delivery, a description of how the informed design of predictive models can aid in the development of sustained drug release systems is presented in Chapter 5 and Chapter 6. Such drug release systems are promising in controlling the bioavailability of biopharmaceuticals while simplifying the drug administration process from the patient's perspective, but are generally time- and resource-intensive to develop. We aim to ease the development of these systems by providing a methodology that can evaluate which predictive models are most suitable for specific applications. The methodology, which obtains quantitative information on

model performance based on a stochastic optimization algorithm, is described in Chapter 5, while a discussion of the results of this methodology when trying to predict the drug release from a couple of experimental model systems appears in Chapter 6.

## Chapter 2

### **EFFECTS OF RESIN ARCHITECTURE AND PROTEIN SIZE ON NANOSCALE PROTEIN DISTRIBUTION IN ION-EXCHANGE MEDIA**

After biopharmaceutical proteins are produced, they generally must be purified in an intensive downstream process in which they are separated from impurities such as debris from the cells in which they were produced, different proteins, and other side products. Protein chromatography remains the main separation technique in this process, with advances in the performance of chromatography often relying on improvements to the chromatographic resins used for protein capture and recovery. This chapter elucidates the architecture and points to the mechanism of protein partitioning in different classes of chromatographic materials, providing guidance for optimizing their performance. This chapter is adapted from a publication in *Langmuir* with permission (Appendix E) [25].

#### **2.1 Introduction**

The distribution of sorbed proteins within chromatographic resins is thought to affect separation performance by affecting uptake rate and capacity. Current design strategies to improve chromatographic resins include influencing the protein distribution through manipulation of the resin architecture, including the use of highly porous resin matrices and polymer modification [26–29]. As opposed to traditional resins, in which proteins adsorb as monolayers directly on the surface of the base matrix, polymer-modified materials contain functionalized polymers that allow volumetric protein partitioning into the polymer-occupied space [30,31]. Although

such advances have led to resins with improved performance, especially in terms of binding capacities, mechanistic understanding of the underlying structural interactions between proteins and the architecture of these resins is currently incomplete. For example, polymer extenders can decrease the effective mesh size and lead to size-exclusion effects that are not present in traditional materials. Consequently, detailed measurements of resin architecture and sorbed protein distribution can improve our understanding of resin performance and aid in the design of superior materials.

Nanoscale characterization of protein adsorption within the resin architecture is challenging with conventional techniques. While imaging techniques such as optical, fluorescence or electron microscopy can visualize the micro- and macrostructure of the resins, they lack the resolution required to study the structure on the length scale of the protein [32–36]. In addition, microscopy techniques often require drying, chemical fixation, or fluorescence labelling of the protein, which raises concerns about whether the observed structural information is an accurate representation of the structure under normal operating conditions [35–37]. Conversely, characterization techniques such as gas adsorption or inverse size-exclusion chromatography (ISEC) can measure general structural parameters such as the total surface area and pore size distribution of the resins, but they do not allow detailed visualization of the resin architecture and are challenging to use after protein sorption [31,35,38–41]. Hence, a true nanoscale characterization of protein distribution in chromatographic resins requires a technique with protein-scale resolution that allows *in situ* characterization without modification of the protein.

In prior research, we developed the method of small-angle neutron scattering (SANS) to characterize resin architecture and protein distribution within

chromatographic resins [42]. SANS is particularly well-suited to study these systems as it is capable of capturing structural features from the nanometer to the micrometer length scale, can probe relatively large sample volumes, can penetrate opaque materials to determine internal structure, and is minimally disruptive [43–47]. The adsorption of lysozyme on a cellulose-based chromatographic material, S HyperCel™, was studied to validate the method and create a framework to support further investigation of chromatographic materials [42,48]. Importantly, we demonstrated that SANS is capable of quantifying the nano- and microscale fractal architecture of S HyperCel™ and the nanoscale distribution of lysozyme in this material, which manifests as a densification of the sorbent’s fractal network. Furthermore, quantitative analysis of SANS measurements determined the amount of sorbed protein under relevant physicochemical conditions. These findings support the view that adsorption in this resin shows similarities to volumetric partitioning in polymer-modified resins because of the high crosslink density and consequent fractal nature of the cellulose base matrix, explaining the material’s high static and dynamic binding capacities for small proteins [35,36].

In this chapter we study the nano-to-mesoscale architectures of three fundamentally different resins: a traditional agarose-based resin (SP Sepharose Fast Flow™) and two dextran-modified agarose-based resins (SP Sepharose XL™ and Capto S™), in addition to the previously studied S HyperCel™. The four resins are referred to in this chapter simply as FF, XL, Capto, and HyperCel, respectively. These materials have been extensively studied before, in terms of both performance as well as structural characterization using conventional techniques such as ISEC and microscopy methods [31–36,38,49]. As a hypothesis, we propose that the size of

proteins will affect their sorbed distribution at the nanoscale in these different chromatographic media. To test this, we use SANS to quantify the nanostructural changes in these resins after adsorption of lysozyme, lactoferrin, and a monoclonal antibody (mAb) under varying loadings.

## **2.2 Experimental Section**

### **2.2.1 Materials**

#### **2.2.1.1 Buffers**

Monobasic sodium phosphate ( $\text{NaH}_2\text{PO}_4$ ) and sodium chloride ( $\text{NaCl}$ ) were purchased from Fisher Scientific (Waltham, MA), deuterium oxide ( $\text{D}_2\text{O}$ ) at 99.8 atom % D was purchased from Cambridge Isotope Laboratories, Inc. (Tewksbury, MA), and acetic acid was purchased from Sigma-Aldrich (St. Louis, MO). They were used to prepare 10 mM sodium phosphate buffer solutions at pH 7 and 10 mM acetic acid buffer solutions at pH 5 in both deionized (DI) water ( $\text{H}_2\text{O}$ ) and  $\text{D}_2\text{O}$ . The total ionic strength (TIS) in the solutions was adjusted using  $\text{NaCl}$  to 20 mM, 50 mM, 100 mM, and 200 mM TIS.

#### **2.2.1.2 Protein Solutions**

Hen egg white lysozyme (molecular weight [MW] 14.3 kDa) was purchased from Sigma-Aldrich, recombinant human lactoferrin (MW 78 kDa) was purchased from Lee BioSolutions (Maryland Heights, MO), and an IgG2 monoclonal antibody (mAb, MW 144 kDa, pI 7.9) was provided by Amgen, Inc. (Thousand Oaks, CA). The lysozyme and lactoferrin were prepared by dissolving the lyophilized proteins in each of the four TIS-controlled, sodium phosphate pH 7 buffers in  $\text{H}_2\text{O}$ , while the

mAb was provided in a concentrated solution and diluted with each of the four TIS-controlled, acetic acid pH 5 buffers in H<sub>2</sub>O before buffer exchange. Protein solutions were subsequently buffer-exchanged three times with the appropriate pH 7 (lysozyme and lactoferrin) or pH 5 (mAb) H<sub>2</sub>O-based buffer, using either 3 or 50 kDa Amicon Ultra-15 centrifugal filters from Millipore (Billerica, MA). Concentrated protein solutions were filtered at 0.22 μm and concentrations were determined using UV spectrophotometry (Thermo Scientific NanoDrop 2000, Waltham, MA).

### **2.2.1.3 Chromatographic Media**

S HyperCel™ (lot AU31072012-4) was provided by Pall Corporation (Northborough, MA). SP Sepharose Fast Flow™ (lot 10224983), SP Sepharose XL™ (lot 311563), and Capto S™ (lot 10061582) were obtained from GE Healthcare (Piscataway, NJ). All four resins are functionalized for cation exchange (CEX) with a sulfonate ligand; other key properties of these resins have been reported before [32–36]. FF and XL have the same agarose base matrix, but 40 kDa dextran is grafted onto XL, which can result in the attachment of each dextran molecule at more than one point. Both resins are functionalized with the same sulfonate group on a six-carbon spacer arm. Conversely, Capto uses the same 40 kDa dextran extenders as XL, but it has a more highly crosslinked agarose base matrix and is functionalized with a sulfonate group on a two-carbon spacer arm. HyperCel is synthesized from a highly crosslinked cellulosic base matrix and functionalized with a sulfonate ligand without a spacer arm. The relatively narrow pore structure of HyperCel has been compared to that of the dextran-modified resins [36]. Consequently, these resins are suitable for making direct structural comparisons. The average particle diameter is reported to be 90 μm for the agarose-based resins [32] and 75 – 80 μm for HyperCel [35].

The chromatographic particles were washed three times by suspending in DI H<sub>2</sub>O and then centrifuging and decanting. This was followed by solvent exchange with D<sub>2</sub>O by repeating this procedure twice by suspending in D<sub>2</sub>O and letting the solution equilibrate for a twelve-hour interval.

#### **2.2.1.4 Sample Preparation**

Each of the four resins was investigated ‘neat’ without adsorbed protein as well as after adsorption of each of the three proteins, leading to 16 resin-protein combinations. Each of these combinations was investigated at four TIS conditions – 20 mM, 50 mM, 100 mM, and 200 mM TIS – to influence the protein loading, leading to a total of 64 resin-protein samples, which include neat samples with no protein.

To measure the structure of the neat chromatographic media, the 16 samples were prepared by equilibrating 0.5 mL hydrated particle volume (h<sub>pv</sub>) of chromatographic particles with 9.5 mL of the appropriate TIS-controlled sodium phosphate buffer in D<sub>2</sub>O. After equilibration by gentle end-over-end rotation over a 48-hour period, the settled chromatographic particle slurry was separated from the supernatant to use in the neutron scattering experiment.

To measure protein uptake, each of the 48 protein-laden samples was prepared with (1) 0.5 mL hydrated particle volume (h<sub>pv</sub>) of chromatographic media equilibrated with pure D<sub>2</sub>O, (2) a certain volume of concentrated protein solution in the appropriate TIS-controlled H<sub>2</sub>O buffer, determined by the desired final protein concentration, and (3) the appropriate pH 5 or pH 7 TIS-controlled D<sub>2</sub>O buffer solution to bring the total sample volume to 10 mL. Samples were equilibrated by gentle rotation over a 48-hour period, after which protein concentrations in the

supernatant solutions were measured using UV spectrophotometry (Thermo Scientific NanoDrop 2000). The settled particle suspension, consisting of approximately 10 vol % protein, 20 vol % particles, and 70 vol % water, depending on the sample, was separated from the supernatant to use in the neutron scattering experiment.

### 2.2.1.5 Sample Compositions

For each resin-protein combination, the added amount of concentrated protein solution at each of the four TISs was specifically selected such that sorbed protein concentrations would vary within the resin-protein combination, while keeping the supernatant protein concentration after adsorption around 1 mg/mL. The added amounts of protein were based on previous adsorption isotherm data for these resin-protein combinations [32,36]. The supernatant protein concentration of 1 mg/mL was chosen such that the protein loading would lie well within the plateau region of the adsorption isotherms and the static binding capacity of the resins for the specific protein and TIS conditions was approached.

The adsorbed amount  $q$  (mg / mL hpv) was determined by mass balance

$$q = \frac{V}{V_m} (C_0 - C), \quad (2.1)$$

where  $V$  (mL) is the total solution volume,  $V_m$  (mL hpv) is the hydrated particle volume (hpv),  $C_0$  (mg/mL) is the initial protein concentration, and  $C$  (mg/mL) is the final protein concentration in the supernatant. Figure 2.1 shows the protein loadings obtained for each resin-protein combination. Each point in this figure is a single point

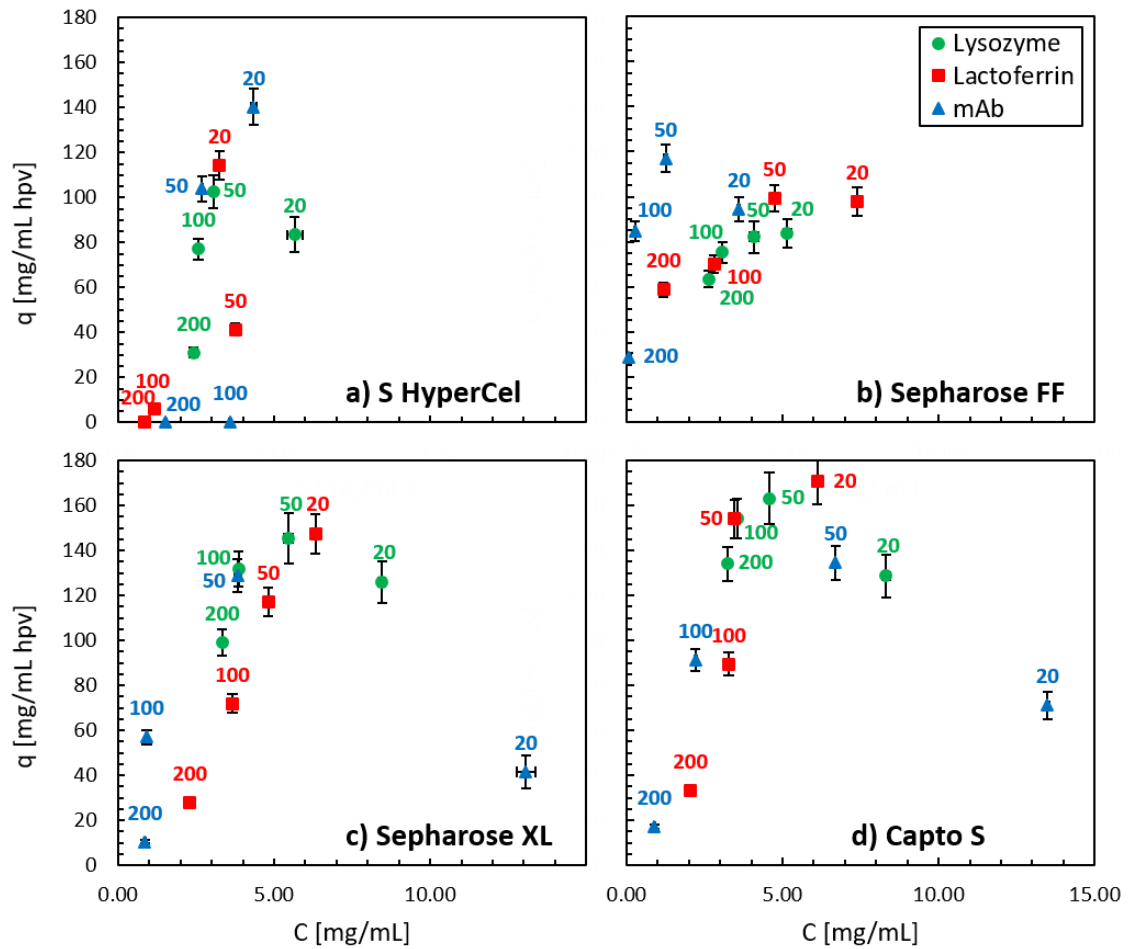


Figure 2.1: Adsorbed protein concentrations in the chromatographic media as a function of supernatant concentration. The labels indicate the approximate total ionic strength (TIS) of each sample.

of the protein adsorption isotherm, typically lying in the plateau region of the isotherm. The observed trends in protein loading generally correspond well to protein adsorption isotherm data measured previously, with decreased protein loading at higher TISs. However, for a few samples at 20 mM the protein loading is significantly lower than expected from previous isotherm data, *e.g.*, mAb in agarose-based resins.

Additionally, previous data show higher adsorbed amounts than measured here [32,36], which is also reflected in the fact that the supernatant protein concentrations are generally slightly higher than the intended 1 mg/mL. The lower adsorption might be due to several factors, including slow protein uptake at very low TIS [50] and D<sub>2</sub>O being a major component of the solvent instead of just H<sub>2</sub>O. However, these observations do not compromise further structural analysis from the SANS patterns.

Small amounts of H<sub>2</sub>O are introduced into the samples via the concentrated protein solutions, leading to varying D<sub>2</sub>O:H<sub>2</sub>O fractions in the solvent of the samples. As the amount of H<sub>2</sub>O in the sample has an important effect on the background scattering, scattering length density, and overall scattering intensity, these variations in D<sub>2</sub>O:H<sub>2</sub>O fraction were taken into consideration during analysis of the scattering patterns.

## **2.2.2 Methods**

### **2.2.2.1 Small-Angle Neutron Scattering**

An extensive overview of the theoretical background on small-angle neutron scattering (SANS), with particular regard to its use for solid-state protein systems, has been provided in prior work [42,51]. Concisely, SANS can probe structural heterogeneity within the sample by measuring the intensity  $I(Q)$  of deflected neutrons at a certain angle from the incident beam,  $\theta$ , which for simple systems can be described as [45–47]

$$I(Q) \propto (\Delta\rho)^2 \cdot P(Q) \cdot S(Q) + B, \quad (2.2)$$

in which

$$Q = \frac{4\pi}{\lambda} \sin \frac{\theta}{2}, \quad (2.3)$$

where  $Q$  is the magnitude of the momentum transfer vector,  $\lambda$  is the wavelength of the neutrons, and  $\rho$  is the scattering length density (SLD), which is material-dependent and determines the scattering contrast in the sample. As  $Q$  is related to the length scale being probed,  $d$ , by Bragg's law [45]

$$d = \frac{2\pi}{Q}, \quad (2.4)$$

features observed in SANS patterns contain structural information on the sample on these real-space length scales. This structural information is represented in Equation 2.2 by the form factor  $P(Q)$ , which represents the contribution of the shape of the particles or building blocks in the system to the scattering intensity, and the effective structure factor  $S(Q)$ , which represents the contribution of the interactions among these components. The background scattering  $B$  is typically observed in the high- $Q$  region of the pattern and depends on sample composition but provides no structural information. Note that the magnitude of the momentum transfer vector is denoted in this chapter by  $Q$ , as opposed to  $q$  in subsequent chapters, to distinguish it from the adsorbed amount of protein (Equation 2.1).

The experiments were carried out on the 30 m NG7 SANS instrument at the NIST Center for Neutron Research (NCNR), National Institute of Standards and

Technology (NIST), Gaithersburg, MD [52]. The instrument settings for the tests were:

- high  $Q$ : 1 m sample-to-detector distance (SDD) with 6 Å neutrons for a 360 s count time,
- intermediate  $Q$ : 4 m SDD with 6 Å neutrons for a 600 s count time, and
- low  $Q$ : 13 m SDD with lenses with 8 Å neutrons for a 900 s count time.

When spliced together, these regions result in a scattering range  $0.001 \text{ \AA}^{-1} < Q < 0.4 \text{ \AA}^{-1}$ , corresponding to length scales ranging from  $\sim 600 \text{ \AA}$  to  $\sim 5 \text{ \AA}$ . Demountable quartz window sample cells with a path length (thickness) of 1 mm were used for all samples and a wavelength spread of 0.15 was used for all experiments. Standard data reduction procedures were followed using the program IGOR Pro to obtain corrected and radially averaged SANS scattering patterns [53]. Instrument corrections were applied to the models for comparison with data and the effects of instrumental smearing on the parameter values were determined to be negligible during model fitting using IGOR Pro.

#### **2.2.2.2 Structural Models**

The SANS patterns were modeled by standard expressions to obtain quantitative structural information, namely (1) the generalized Guinier-Porod model [54] for the cellulose-based resin and (2) the polydisperse cylinder model [55] for the agarose-based resins. These models were used to fit the scattering patterns of the resins regardless of the presence of adsorbed protein as they accurately fit the scattering data both before and after protein adsorption.

The generalized Guinier-Porod model is an empirical model that successfully describes the nano-to-mesoscale structure of HyperCel [42,48]. The model describes a material with a fractal nature and is given by [54]

$$I(Q) = \frac{G}{Q^s} \exp\left[\frac{-Q^2 R_g^2}{3-s}\right] + B \quad \text{for } Q \leq Q_1 \quad \text{and} \quad (2.5)$$

$$I(Q) = \frac{D}{Q^m} + B \quad \text{for } Q > Q_1, \quad (2.6)$$

in which

$$Q_1 = \frac{1}{R_g} \sqrt{\frac{(m-s)(3-s)}{2}} \quad \text{and} \quad (2.7)$$

$$D = G \exp\left[\frac{-Q_1^2 R_g^2}{3-s}\right] Q_1^{m-s}, \quad (2.8)$$

based on continuity constraints. In these expressions,  $B$  is the background scattering,  $G$  is a scaling coefficient,  $R_g$  is the radius of gyration, and  $m$  and  $s$  are the Porod exponent and the dimension variable, which are related to the fractal dimensions of the microstructure on short and long real-space length scales, respectively. The radius of gyration can be obtained from the  $Q$ -value at the inflection point  $Q_1$  between the two fractal regions. Hence, this radius of gyration is a characteristic average length scale within the particle structure, with length scales below the  $R_g$  characterized by a fractal dimension related to the Porod exponent and length scales above the  $R_g$  characterized by a fractal dimension related to the dimension variable.

The SANS patterns from the agarose-based resins were fit using a polydisperse cylinder model, which represents a collection of non-interacting cylinders with a mean radius  $R$  and length  $L$ . Polydispersity of the cylinder radius is modelled using a normalized log-normal distribution  $n(r)$ . For this model, the scattering intensity as a function of  $Q$  is calculated as [55]

$$I(Q) = \frac{\phi}{V} (\rho_{cyl} - \rho_{solv})^2 \iint n(r) F^2(Q, r, \alpha) \sin \alpha \, d\alpha \, dr + B, \quad (2.9)$$

in which

$$V = \pi R^2 L, \quad (2.10)$$

$$n(r) = \frac{\exp\left[-\frac{1}{2}\left(\frac{\ln(r/R)}{\sigma}\right)^2\right]}{\sqrt{2\pi}\sigma R}, \text{ and} \quad (2.11)$$

$$F(Q, r, \alpha) = 2V j_0\left(\frac{QL \cos \alpha}{2}\right) \frac{J_1(Qr \sin \alpha)}{Qr \sin \alpha}. \quad (2.12)$$

The seven fitting parameters are (1) the volume fraction  $\phi$ , (2) the mean radius  $R$ , (3) the length  $L$ , (4) the radial polydispersity  $\sigma$ , which is equal to the standard deviation of the log-normal distribution, (5) the SLD of the cylinder  $\rho_{cyl}$ , (6) the SLD of the solvent  $\rho_{solv}$ , and (7) the background  $B$ . The polydisperse cylinder model is a two-phase model, one phase consisting of the cylinders and one phase consisting of the solvent. In such models, the SLD values of the two phases affect only the overall scaling of the scattering intensity, not the shape of the scattering pattern and consequently not the other structural parameters of the model except the volume fraction, which also scales directly with the scattering pattern.

### 2.2.2.3 Protein Form Factors

Equation 2.2 can be applied directly to protein systems within a framework in which the form factor  $P(Q)$  is the protein monomers' characteristic, rotationally averaged scattering pattern due to their shape, while the effective structure factor  $S(Q)$  is due to local interactions in solution, clustering, and aggregation. Both of these can have an effect on the total scattering pattern from protein solutions. However, in dilute protein solutions, the structure factor contribution becomes negligible and the protein form factor can be directly obtained from SANS measurements. The form factors of the three proteins were measured experimentally by SANS after dilution of the concentrated protein solutions to approximately 5 mg/mL in the pH 7 (lysozyme and lactoferrin) or pH 5 (mAb) buffer in D<sub>2</sub>O at 20 mM TIS, a concentration low enough to minimize contributions from the protein structure factor. The experimental form factors of the three proteins are shown in Figure 2.2.

The scattering pattern contribution from the form factor was calculated directly from the atomic structure of the protein using the program CRYSON [56] as applied to structural data from the RCSB Protein Data Bank (PDB) [57]. These calculations can take effects such as the solvation shell (not applied here) and the solvent composition (100 mole % D<sub>2</sub>O) into account. The CRYSON output is the form factor of a single protein monomer in units of barn ( $1 \text{ b} = 10^{-28} \text{ m}^2$ ). The scattering pattern scales linearly with the protein concentration, so the concentration of the protein can be taken into account by multiplication of the calculated scattering pattern by the protein concentration. Thus the protein monomer contribution can be predicted from the protein concentration in the system, or conversely, the protein concentration can be determined from its contribution to the scattering intensity.

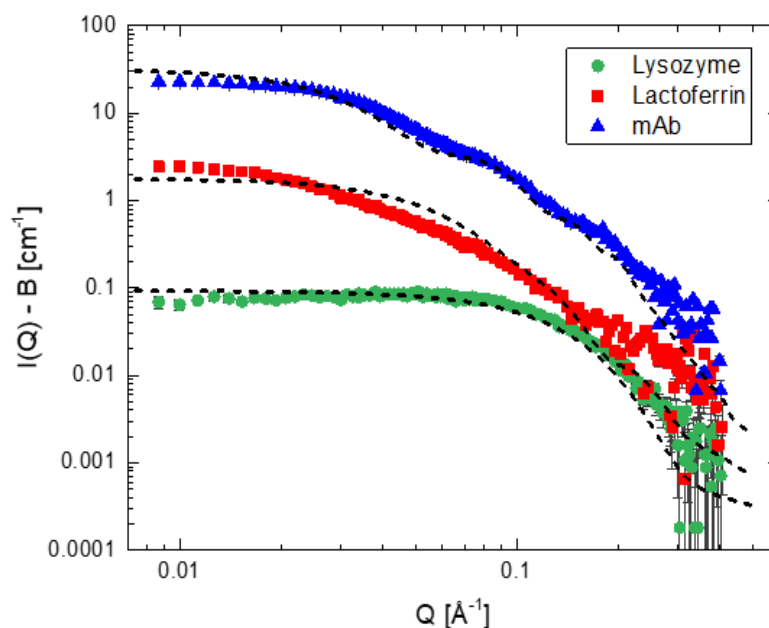


Figure 2.2: Scattering patterns of protein solutions at low concentrations (approximately 5 mg/mL), showing the characteristic scattering pattern of protein monomers, *i.e.*, the protein form factor. CRYSON scattering predictions from protein PDB files are shown by the dashed lines. Successive curves are offset by a factor of 4 for clarity.

CRYSON was used to compare the experimentally measured form factors to the values calculated from the protein atomic structures. The PDB files used to model lysozyme, lactoferrin, and the mAb have the PDB IDs 6LYS [58], 2BJJ [59], and 1IGT [60], respectively. The CRYSON predictions are shown by the dashed lines in Figure 2.2. They capture the experimentally determined form factors fairly well, although small deviations can be observed for each protein in specific regions. These deviations can be caused by the flexibility of the protein structure in solution, such as mAb hinge motions, as opposed to the crystalline protein structure obtained from the PDB files. Consequently, such small deviations can be expected and the CRYSON

predictions adequately confirm the experimentally determined form factors, which are used to characterize protein adsorption in the chromatographic resins.

#### **2.2.2.4 Model Fitting of Neat Resins**

For the neat resins with no adsorbed protein, structural models described the scattering patterns well over the whole  $Q$  range, and the models could consequently be directly fit to the experimental data using IGOR Pro's NCNR Analysis Macros [53]. For the generalized Guinier-Porod model for HyperCel, no parameters were held fixed during the fitting process, generally resulting in five fitting parameters. For the polydisperse cylinder model for agarose-based resins, the cylinder length and the SLD values were held fixed during fitting. The model described the experimental data well for cylinders that were effectively infinitely long. Hence, the cylinder length was fixed at 10000 Å to simplify the model and reduce the number of fitting parameters to four.

SLD values for the base matrix and the solvent were calculated using the NCNR SLD Calculator [61,62], for which the molecular densities were calculated from the displaced solvent volumes of the ensemble atomic groups [63]. The SLD of pure D<sub>2</sub>O and of the agarose base matrix in pure D<sub>2</sub>O were calculated to be  $6.33 \times 10^{-6} \text{ \AA}^{-2}$ , and  $2.22 \times 10^{-6} \text{ \AA}^{-2}$ , respectively. Note that the SLD of polymers such as agarose and proteins can change depending on the D<sub>2</sub>O content of the surrounding environment due to deuterium exchange. For these calculations, it was assumed that the fraction of exchanged hydrogens on the polymer was equal to the fraction of D<sub>2</sub>O in the solvent (100% for the neat resins). Contributions to the solvent SLD from buffer components and to the cylinder SLD from sulfonate ligands and dextran extenders were assumed to be negligible to simplify model calculations. Deviations

due to such contributions are effectively all included in the fitted volume fraction and polydispersity.

#### **2.2.2.5 Model Fitting of Protein-Laden Resins**

To first order, one might expect that the scattering patterns from protein-laden resins can be modeled by a summation of the scattering patterns from the neat resins and the protein monomer form factor. However, the sorption of the protein on the resin can introduce changes to both the apparent nanostructure of the resin as well as the proteins' contribution to the scattering. Indeed, as the resin and protein have similar scattering length densities, the protein distribution into the available space within the resins will be perceived by SANS as an apparent change of the resin nanostructure. Furthermore, resin-protein and protein-protein interactions can lead to changes in the protein scattering contribution. Regardless of these changes, the same structural models with different parameters can be used for the protein-laden resins as the neat resins, with the exception of the high- $Q$  region, where explicit protein contributions are evident. This region was instead fit directly to the expected form factor scattering from the protein monomers. More detailed information on the modeling of protein-laden resins, including specific fitting ranges and fixed fitting parameters, is included in Appendix A.

### **2.3 Results and Discussion**

SANS patterns were measured for four resins (HyperCel, FF, XL, and Capto) and three proteins (lysozyme, lactoferrin, and a mAb), in addition to the neat resin structures with no adsorbed protein, leading to 16 resin-protein configurations. Each configuration was studied at four different total ionic strengths (TISs), which affect the

total protein loading. This resulted in a total of 64 scattering patterns, of which only a select few are shown directly here for brevity. However, all scattering patterns and model parameters are included in Appendix A.

### 2.3.1 Scattering Patterns of Neat Resins

The reduced scattering patterns of the four resins at 50 mM TIS are shown in Figure 2.3; symbols represent the experimental data, while the dashed lines show the model fits. HyperCel is modeled by the generalized Guinier-Porod model, while the agarose-based resins are modeled by the polydisperse long-cylinder model. Fitting parameters are provided in Table 2.1 and Table 2.2. The HyperCel model parameters agree with those found previously [42]. The Porod exponent  $m$  is related to the fractal dimension within individual resin strands, while the dimension variable  $s$  is related to the fractal dimension of the larger resin strand network. The average radius of gyration in the model fits, which can be associated with the radius of gyration of the resin strands, is 34 Å.

For the agarose-based resins, in FF and XL the mean cylinder radii are 14 and 3 Å and the radial polydispersities  $\sigma$  are 0.9 and 1.3, respectively. In the more densely crosslinked Capto, the mean cylinder radius is 51 Å and the polydispersity is 0.6. The measured volume fractions of the cylinders range from 3 to 5%, which is consistent with the use of 4% agarose in Sepharose FF beads (Sepharose 4). For the neat resins, these parameters are not strongly affected by changing the TIS.

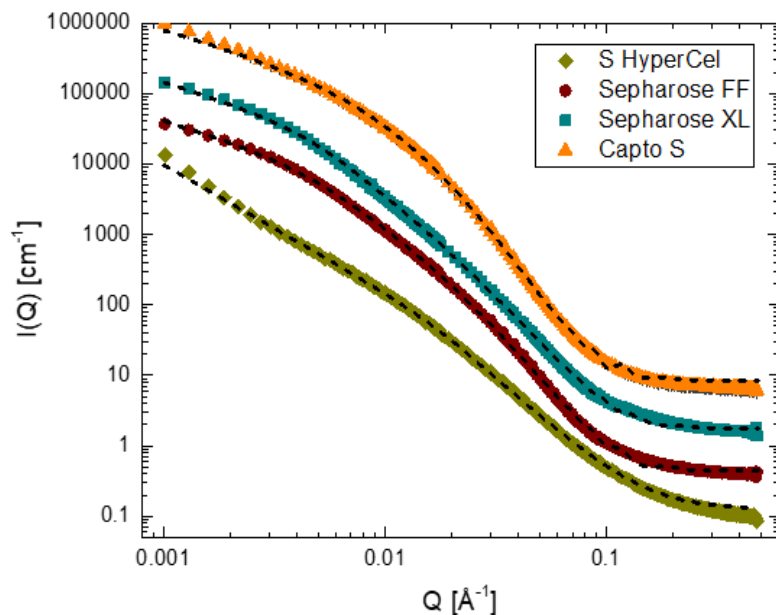


Figure 2.3: Scattering patterns of neat chromatographic media at 50 mM total ionic strength. Model fits are shown in the dashed lines. Successive curves are offset by a factor of 4 for clarity.

Table 2.1: Fitting parameters of the generalized Guinier-Porod model and fitting values for neat and protein-laden S HyperCel.

	Neat <sup>a</sup>	Lysozyme <sup>a</sup>	Lactoferrin <sup>a</sup>	MAB <sup>a</sup>
Scale $G$ [-]	0.040	0.005	0.019	0.012
Radius of gyration $R_g$ [Å]	33.5	35.9	33.4	31.2
Dimension variable $s$ [-]	1.79	2.17	1.80 <sup>b</sup>	1.80 <sup>b</sup>
Porod exponent $m$ [-]	2.72	2.65	2.70 <sup>b</sup>	2.70 <sup>b</sup>
background $B$ [cm <sup>-1</sup> ]	0.13	0.21	0.21	0.24

<sup>a</sup> Table values include only samples at 50 mM total ionic strength. Fitting values for all samples are included in Appendix A.

<sup>b</sup> Values were held fixed during fitting.

Table 2.2: Fitting parameters of the polydisperse cylinder model and fitting values for neat agarose-based resins.

	SP Sepharose FF <sup>a</sup>	SP Sepharose XL <sup>a</sup>	Capto S <sup>a</sup>
Volume fraction $\phi$ [-]	0.034	0.025	0.049
Mean cylinder radius $R$ [Å]	13.8	3.2	52.0
Radial polydispersity $\sigma$ [-]	0.92	1.26	0.57
Cylinder length $L$ <sup>b</sup> [Å]	10000	10000	10000
SLD cylinder $\rho_{cyl}$ <sup>b</sup> [ $10^{-6}$ Å <sup>-2</sup> ]	2.22	2.22	2.22
SLD solvent $\rho_{solv}$ <sup>b</sup> [ $10^{-6}$ Å <sup>-2</sup> ]	6.33	6.33	6.33
Background $B$ [cm <sup>-1</sup> ]	0.12	0.11	0.15

<sup>a</sup> Table values include only samples at 50 mM total ionic strength. Fitting values for all samples are included in Appendix A.

<sup>b</sup> Values were held fixed during fitting.

### 2.3.2 Nano-to-Mesoscale Architecture of Neat Resins

The cellulose-based HyperCel has an architecture that is fundamentally different from that of the agarose-based resins. HyperCel is well-described by the generalized Guinier-Porod model, which indicates fractal behavior on two distinct length scales: (1) a dense fractal network of cellulose within the resin fibrils, as indicated by the Porod exponent  $m$ , and (2) a more open fractal network of the resin fibrils themselves on longer length scales, as indicated by the dimension variable  $s$ . These observations correspond to previous SANS measurements on HyperCel and explain why this resin shows performance comparable to that of polymer-modified materials [42]. However, the generalized Guinier-Porod model is incapable of capturing the architecture of agarose-based resins, which indicates that these materials are inherently not fractal-like. Instead, these materials are better described by the polydisperse cylinder model, in which the cylinder length is very long compared to the

cylinder radius. Consequently, the resin strands of which these materials are composed are not intrinsically arranged in a fractal network.

These observations agree well with previously-known information on the molecular structure of these materials. While cellulose gels are generally composed of a random polymer network, X-ray diffraction experiments have shown that agarose appears as rigid single or double helices of about 15 Å in diameter in the gel state [64–67]. Comparison with electron microscopy imaging, which shows filaments on the order of 20 – 300 Å, has led to the hypothesis that these filaments are composed of up to hundreds of agarose helices in a side-by-side assembly [32,34,35,64,68].

SANS provides an independent measurement of the resin strand thickness on smaller length scales and averaged over a large sample volume. As other techniques that can access protein-scale structural information, such as ISEC, measure the pore size distribution, these two techniques can provide complementary information about the accessible space and the filled space in these resin materials. For HyperCel, the measured radius of gyration of the resin strands is about 34 Å, which corresponds well with mean pore radius measurements via ISEC of about 40 Å [35]. This makes physical sense, as in a random polymer network, one can expect that the pore sizes are of a similar length scale to the characteristic length scale of the polymer network [69].

For FF, the mean cylinder radius as measured by SANS is 14 Å. This corresponds fairly well to the diameter of the double helices that compose agarose gels. The fact that SANS can detect these thin strands implies that these helices are sufficiently far apart that they can be observed as distinct scattering objects. Consequently, the observation that these helices form a dense side-by-side assembly within the larger filaments in electron microscopy may be incorrect. Instead, the

scattering data suggest that within the filaments, the agarose helices are more loosely distributed. We suspect that these bundle features observed in electron microscopy images probably arise from polymer rearrangement due to resin drying during sample preparation and are not reflective of the media in its native state.

As FF and XL have the same agarose base matrix, the measured difference in cylinder radius between the two materials is due to the dextran modifications in XL. The decrease in the mean cylinder radius from 14 Å in FF to 3 Å in XL and the increase in the polydispersity are consistent with the idea of dextran extending into the pore space, assuming that SANS resolves the individual dextran strands.

In Capto, the significantly larger mean radius of the resin strands of 51 Å is probably caused by the more highly cross-linked base matrix, which makes it somewhat similar to HyperCel. Consequently, due to the higher degree of cross-linking, agarose helices in Capto may arrange in the dense side-by-side assembly to form thicker strands as hypothesized before [64,68]. The fact that the dextran extenders are not directly observed in Capto may be due to the fact that larger scattering objects, such as the thicker strands, cause a significantly increased scattering intensity, which can overwhelm the scattering from the much smaller dextran polymers.

Schematic representations of these interpretations, based on the structural models, are shown in the top panels of Figure 2.4. In this figure, the long strands in the agarose-based materials represent the helices. Random, single-strand connections between these helices are not explicitly shown, nor are the dextran extenders.

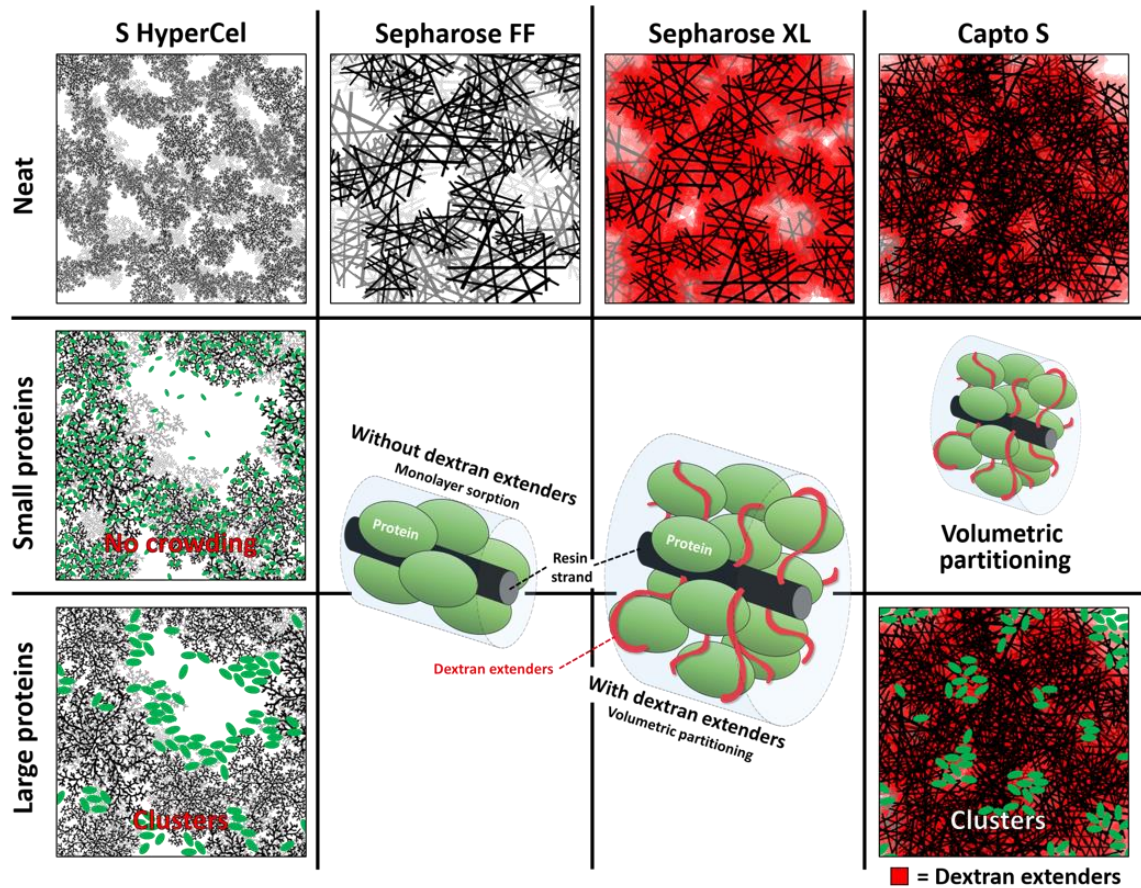


Figure 2.4: Overview of the inferred sorption behavior as a function of resin architecture and protein size. In this work, lysozyme is considered a small protein and lactoferrin and mAbs are considered large proteins.

### 2.3.3 Scattering Patterns of Protein-Laden Resins

Lysozyme, lactoferrin, and a mAb were sorbed into the chromatographic resins under different protein loadings by changing the TIS of the solvent among 20, 50, 100, and 200 mM. SANS patterns at 50 mM TIS, at which the protein loading is generally high (Figure 2.1), are shown in Figure 2.5. For each resin, the same models used to fit the neat resins were used to fit the protein-laden resins, and these are shown by the dashed lines in Figure 2.5. The high- $Q$  region was excluded from the model fits

because the contribution from protein monomers was accounted for instead by protein form and structure factors, as discussed in the Experimental Section (Section 2.2).

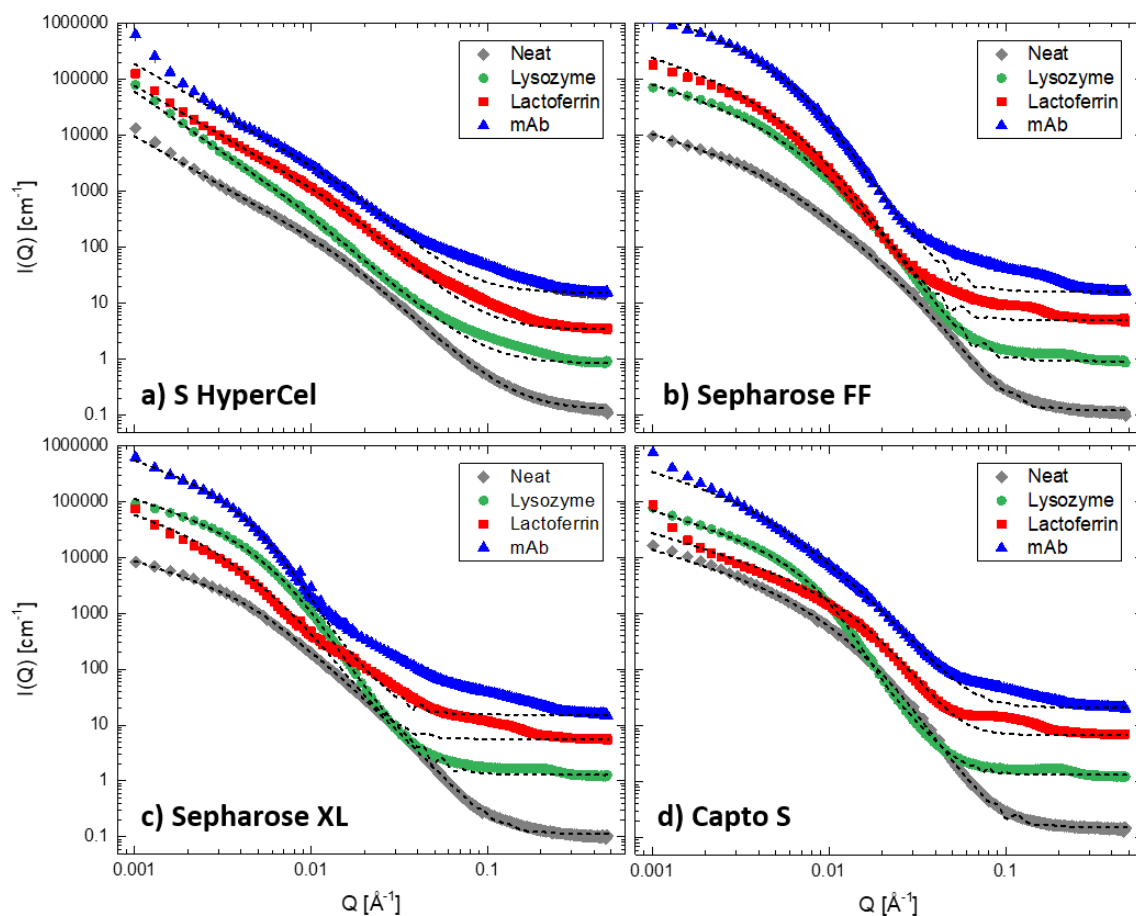


Figure 2.5: Scattering patterns of protein-sorbed chromatographic media at an approximate total ionic strength of 50 mM. Error bars are generally smaller than the symbol size. Successive curves are offset by a factor of 4. Structural model fits are shown by the dashed lines, and were fit only to the background scattering and the low- $Q$  region, up to the  $Q$ -value where the presence of the protein caused an inflection in the scattering pattern, typically around  $0.03 \text{ \AA}^{-1}$ . Specific fitting ranges are included in Appendix A.

The fitting parameters for the generalized Guinier-Porod model for protein-laden HyperCel at 50 mM are included in Table 2.1. After protein adsorption, the Porod exponent and radius of gyration, which correspond to the fractal dimension inside and the size of the cellulose strands, do not vary significantly from the values for the neat resin, 2.7 and 34 Å, respectively. For the HyperCel-lysozyme system, the dimension variable, which corresponds to the fractal dimension of the larger-scale resin strand network, increases as a function of the amount of adsorbed protein, going up to 2.4 for the 20 mM lysozyme sample as compared to the 1.8 of the neat resin. However, for the larger proteins the dimension variable does not change after protein adsorption at any TIS value; only the scaling coefficient changes due to variation in the SLDs. Consequently, the HyperCel architecture does not change at all with adsorption of larger proteins, which is illustrated by fixing the Porod exponent and dimension variable for these protein-resin combinations. The only change in the scattering pattern is the contribution of the protein monomers at high  $Q$  and an upturn at very low  $Q$ , which indicates the presence of larger objects outside the scattering limits.

The fitting parameters for the polydisperse cylinder model for the protein-laden agarose-based resins are the radial polydispersity, the mean cylinder radius and the SLD of the solid cylinder phase. The radial polydispersity is generally around 0.5 – 0.6 for the protein-laden resins. The mean cylinder radius for each sample and the SLDs of the cylinders as a function of the amount of adsorbed protein are shown in Figure 2.6 and Figure 2.7, respectively. The mean cylinder radius generally increases from the value for the neat resins (shown by the gray lines) as more protein is loaded on the resins (Figure 2.6). This increase in cylinder radius is accompanied by a shift of

the SLD from the value for agarose for neat resins to an SLD between the values for pure D<sub>2</sub>O and typical proteins (Figure 2.7).

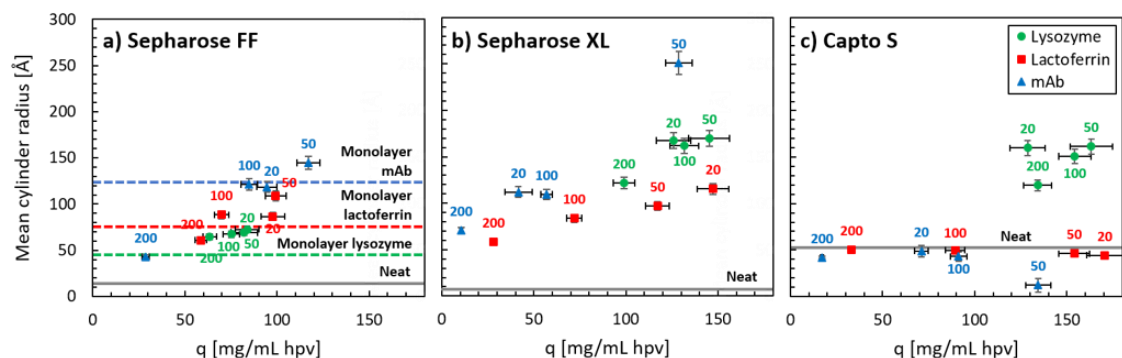


Figure 2.6: Cylinder radii of protein-laden agarose-based resins obtained by fitting SANS data to the polydisperse cylinder model. The labels indicate the approximate total ionic strength of each sample. The gray lines indicate the cylinder radii obtained for the neat media, while the colored dashed lines indicate the expected core radius if a uniform layer of protein adsorbs.

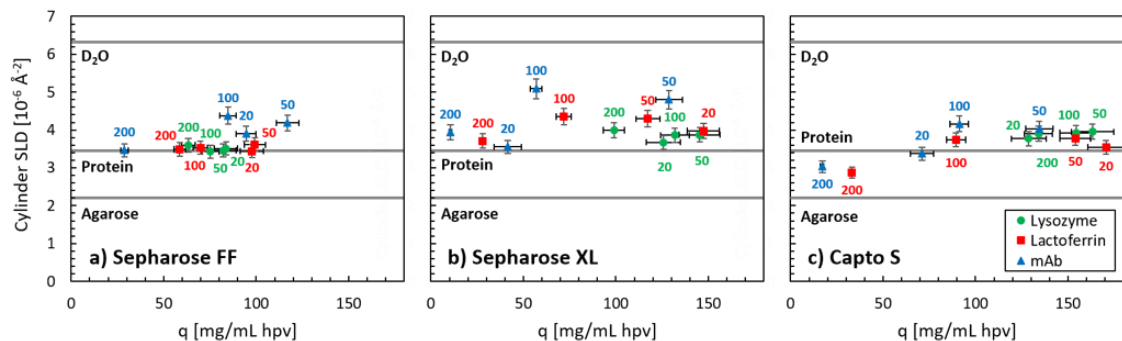


Figure 2.7: Cylinder scattering length densities (SLDs) as obtained from fitting SANS data to the polydisperse cylinder model. The labels indicate the approximate total ionic strength of each sample. The gray lines indicate the SLD of pure D<sub>2</sub>O and the approximate SLD of protein and agarose in the sample solvent. Note that the core SLD for the neat media is the value for agarose, as indicated in the figures.

The high- $Q$  scattering contributions due to protein monomers are compared directly to the expected protein form factors in Figure 2.8. The symbols in this figure show the experimental scattering patterns after subtraction of the structural model fit, which corresponds to the difference between the experimental data (symbols) and model fits (dashed lines) in Figure 2.5. Such subtraction is technically valid only if the two contributions, the structural model and the protein monomer contribution, are strictly uncorrelated, which is not the case here. However, this subtraction is performed here only to highlight the protein contributions in the high- $Q$  region, and deviations due to protein-resin interactions are implicitly included in the effective protein structure factor. In the low- $Q$  region, where the structural model fit describes the experimental scattering well, the subtraction involves two large, almost equal numbers, which typically results in large inherent errors in the data. Consequently, this region of the scattering pattern can be ignored for  $Q$  values below those indicated by the black diamonds in Figure 2.8.

The dashed lines in Figure 2.8 show the predicted contributions of the presence of proteins due solely to the protein form factors, based on the experimental form factors measured in dilute solution (Figure 2.2) but scaled to actual protein concentrations within the resins. Significant deviations between the experimental data and the dashed lines indicate the effect of a protein structure factor different from unity, indicating structuring in the distribution of sorbed protein. The dashed vertical lines in Figure 2.8 indicate the positions of peaks or shoulders in the experimental data and are positioned at the same  $Q$  values in each panel of the figure. These peak positions are summarized in Table 2.3.

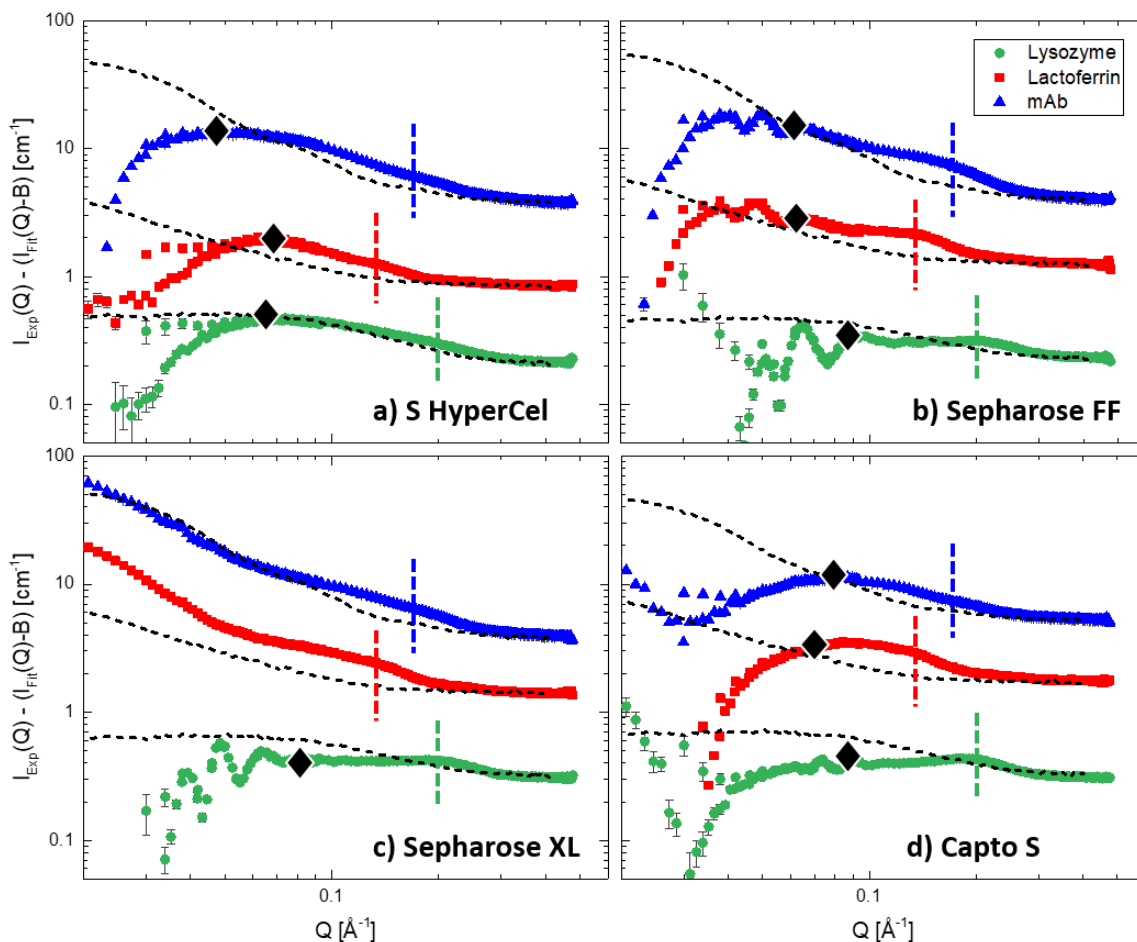


Figure 2.8: Scattering patterns of protein-sorbed chromatographic media after subtraction of the low- $Q$  model fit, at an approximate total ionic strength of 50 mM. The resulting scattering intensity is due to the presence of protein monomers. The predicted scattering intensity due purely to the protein form factor is shown by the dashed lines. The vertical lines show the position of peaks or shoulders in the scattering data, where the difference between the experimental data and the predicted form factor data is generally the highest. These lines are at the same  $Q$ -values in each panel. The black diamonds indicate the  $Q$ -value below which subtraction effects and artifacts become considerable. Error bars due to instrument error are generally smaller than the symbol size. Successive curves are offset by a factor of 4 for clarity.

Table 2.3: Peak positions in the scattering patterns of the protein monomer contributions.

	Lysozyme	Lactoferrin	MAB
Peak position <sup>a</sup> [ $\text{\AA}^{-1}$ ]	0.20	0.13	0.17
Nearest neighbor distance <sup>b</sup> [ $\text{\AA}$ ]	31.4	48.3	37.0
$R_g$ <sup>c</sup> [ $\text{\AA}$ ]	15	30	55

<sup>a</sup> Indicated by the vertical lines in Figure 2.8 for 50 mM total ionic strength. The same peak positions are observed at different ionic strengths (see Appendix A).

<sup>b</sup> Calculated from the peak position using Equation 2.4

<sup>c</sup> Calculated using CRYSON [56]

### 2.3.4 Protein Distribution in S HyperCel

The distribution of lysozyme in HyperCel is found to agree with that observed previously [42], namely that lysozyme adsorption increases the fractal dimension of the resin network (Table 2.1), which corresponds to a densification of this fractal network. This indicates that lysozyme is capable of infiltrating into and adsorbing in the smallest pore spaces within the resin. Moreover, the scattering from the lysozyme monomers at high  $Q$ -values corresponds very well to the predicted form factor scattering (Figure 2.8a). Consequently, contributions from the structure factor are negligible, which means that there are no significant structural protein-protein or protein-resin interactions. A schematic representation of the inferred distribution of lysozyme in HyperCel, where protein monomers lead to a densification of the fractal network, is shown in the first panel of the second row of Figure 2.4.

Larger proteins, such as lactoferrin and the mAb, show very different nanoscale distributions in HyperCel. The adsorption of these proteins has no significant effect on either the Porod exponent or the dimensional variable. Hence, larger proteins seem to be excluded from the smallest pore spaces in the fractal resin

matrix, but can presumably still attach to the resin at the surface of larger pores. This size-exclusion effect can potentially explain the significantly decreased binding capacity of HyperCel for larger proteins, especially at high TIS. Under these conditions, the cellulose strands that make up the smaller fractal regions within the resin matrix could condense, restricting the available interstitial space for large proteins even more [41].

Alternatively, our data suggest that large proteins may accumulate locally in specific regions of the pore space, where they partition from the neighboring resin network due to entropic partitioning. Such entropic effects have been demonstrated previously to lead to specific ordering of colloid-polymer systems, including protein systems [70–72]. However, they have not been associated with the partitioning of proteins in materials such as these chromatographic resins. We argue that instead of solely size-exclusion effects, protein crowding in chromatographic resins may be entropically favored due to depletion or excluded-volume forces.

For these larger proteins, the scattering from the protein monomers at high  $Q$ -values is no longer well-described by the form factor alone (Figure 2.8a). A significant structure factor is present, indicating the presence of protein-protein or protein-resin interactions indicative of local crowding. Such structuring is observed for all other resin-protein combinations investigated in this chapter (Figure 2.8). Indeed, all high- $Q$  scattering patterns have a significant deviation from the predicted form factor scattering. In particular, all scattering patterns show a scattering peak or shoulder in the same position for a specific protein. The approximate positions are indicated by the vertical lines in Figure 2.8 and are summarized in Table 2.3. Note that the vertical line for a given protein is at the same  $Q$  value in each panel of Figure 2.8.

Interestingly, these peaks and their positions are similar to those observed in SANS patterns of frozen protein solutions [73,74] and dried protein phases as discussed in Chapter 4. In frozen solutions, proteins are concentrated in dense phases due to the formation of ice crystals. Consequently, the scattering patterns show a protein-protein interaction peak, also termed the nearest-neighbor peak, as the position of the peak is related to the average distance between neighboring protein molecules in the dense phase through Equation 2.4. The average protein-protein distance as obtained from the approximate peak positions in this work are included in Table 2.3, where they are compared to the radii of gyration of the proteins as obtained from CRYSON [56]. For lysozyme, the inter-protein distance corresponds to twice the protein radius, indicating that the protein molecules are in close contact. For lactoferrin, the inter-protein distance is slightly smaller than twice the radius of gyration. This is possible as lactoferrin has a two-lobed, dumbbell-like shape (Figure 2.9) and the protein molecules can stack side by side. This side-by-side configuration is expected to be facilitated by the highly-charged patch on one of lactoferrin's lobes, which can allow it to adsorb end-on on the functionalized resin. For mAbs, the inter-protein distance is significantly smaller than twice the radius of gyration. Again, this is expected as mAbs are known to interdigitate due to their Y-like shape and flexibility, and the inter-protein distance is governed by the size of the Fab domains [74].

These observations support the idea that in HyperCel, lysozyme can infiltrate the fractal resin network, densifying the network but minimizing protein-protein contact. However, larger proteins are excluded from the network and instead form dense phases on the surfaces of the larger pores in the material due to size-exclusion or entropic effects.

### 2.3.5 Protein Distribution in Sepharose FF and XL

Protein adsorption in FF and XL leads to an increase in the cylinder radius obtained from the polydisperse cylinder model. Generally, the cylinder radius increases with increased amounts of adsorbed protein (Figure 2.6). This increase in the radius is presumably caused by adsorption of the protein on the resin strands. Indeed, the increases in fitted cylinder radii in FF correspond well to the expected values for a monolayer of protein positioned around the strands, as shown by the dashed lines in Figure 2.6a. These values were estimated from the neat resin thickness and the radii of gyration of the proteins as obtained from CRYSON [56], as shown in Figure 2.9. In addition, the SLD of the cylinders shifts from the value for agarose for the neat resins to the value for proteins after protein adsorption (Figure 2.7). The SLD values for the FF-mAb samples are slightly higher, but this is to be expected as the Y-like shape of the mAbs will lead to significant presence of D<sub>2</sub>O in the cylinder volume.

In comparison, the cylinder radii measured for XL are significantly larger than those for FF (Figure 2.6b). This indicates that proteins partition in XL throughout the dextran extenders around the base resin strands. The highest values of the observed cylinder radii in XL are about 170 Å for lysozyme and 250 Å for the mAb, which translates to a thickness of the polymer-filled dextran layer of about 160 – 240 Å, assuming that the base matrix resin strands are equally thick to those in FF. These values correspond fairly well to the thickness of the neat dextran layer as measured by ISEC, which is about 120 – 190 Å [32,76]. The cylinder SLD values for protein-laden XL are also generally higher than in FF, which is expected as the volumetric partitioning of proteins will lead to increased presence of D<sub>2</sub>O in the cylinder volume. Consequently, proteins form relatively dense phases around the resin strands – as

monolayers in the case of FF and by volumetric partitioning in the case of XL, with the dextran included, as is illustrated in the central panels of Figure 2.4.

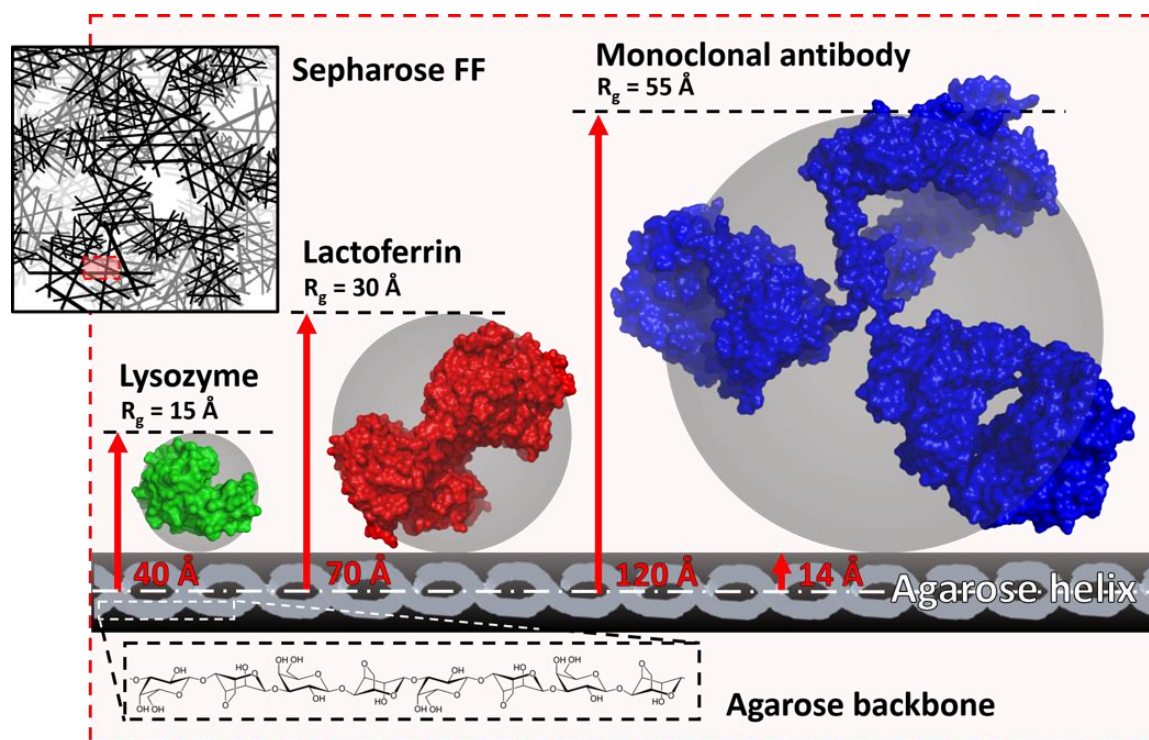


Figure 2.9: Illustration of the effect of protein sorption on the measured radius of an effective cylinder as a function of protein size, assuming that proteins distribute in a monolayer around the resin strands (Figure 2.4, center left). Protein structures were drawn merely for illustration using PyMOL [75] from the same PDB files used for the CRYSON form factor calculations.

This interpretation of the data is further supported by the presence of scattering peaks at high  $Q$  from the sorbed proteins, which are indicative of protein packing. For FF in particular, the peaks are fairly well-defined, indicating that the range of inter-protein distances is fairly narrow. For XL, the peaks are slightly broader, indicating

that the proteins are more heterogeneously distributed. Such behavior is expected as inter-protein distances will be more strictly defined in monolayer adsorption as compared to volumetric partitioning, not least because of the presence of the dextran.

Electron microscopy typically shows clusters or lumps of protein on larger length scales than observed here [34,36]. Again, this may be due to insufficient resolution of the technique and/or to significant structural changes of the resin during sample processing. SANS measurements show that protein molecules distribute within the resins on characteristic length scales on the order of nanometers, which is smaller than what has been observed in electron microscopy.

### **2.3.6 Protein Distribution in Capto S**

Protein adsorption in Capto shows similarities to that in both XL and HyperCel. Lysozyme adsorption in Capto S shows the same behavior as that in XL, with similar cylinder radii, SLDs, and interaction peaks. Consequently, the interpretation is the same as for that resin. However, lactoferrin and mAb adsorption in Capto is characterized by almost no change in the measured cylinder radius (Figure 2.6c). Similarly to the case for HyperCel, these larger proteins seem to be excluded from at least the smallest pores in the resin matrix or within the dextran layer, making them unable to bind close to the base resin strands. However, they can presumably still attach to dextran extenders at the surface of larger pores, as is shown in the bottom right panel of Figure 2.4. Alternatively, similar to the behavior in HyperCel, these larger proteins in Capto may crowd due to entropic partitioning. Such partitioning would help to explain the differences in protein transport observed between traditional and dextran-modified resins. For dextran-modified resins, it has been proposed that protein uptake occurs with a sharp uptake front with incomplete saturation [33]. The

reason for the incomplete saturation was hypothesized to be the inefficient packing of the protein, which can rearrange over time to accommodate more protein. Entropic partitioning is a possible mechanistic explanation for this protein rearrangement.

## **2.4 Conclusions**

Small-angle neutron scattering allows *in situ* characterization of resin architectures and the protein distributions within, with protein-scale resolution. The results obtained here show that protein molecules arrange in chromatographic resins on nanometer length scales, smaller than what has previously been observed with conventional characterization techniques, and the results reflect the variability of these arrangements that would be expected as a function of resin architecture and protein size. Dextran-modification or the fractal architectures of cellulose-based materials can increase protein loading due to the possibility of volumetric partitioning. However, highly cross-linked chromatographic materials can exhibit crowding behavior of larger proteins such as lactoferrin and mAbs due to size-exclusion or entropic partitioning effects. While these observations confirm the structural origins of the increased binding capacities in the resins investigated, they could also explain the higher salt sensitivity of larger proteins in these materials and their distinct transport behavior. Consequently, these observations can be used to guide design of chromatographic resins. Moreover, the techniques presented here allow characterization of novel and future resin materials, and the mechanisms inferred to contribute to the observed behavior can certainly be applicable in other systems.

## Chapter 3

### CHARACTERIZATION OF PROTEIN-EXCIPIENT MICROHETEROGENEITY IN BIOPHARMACEUTICAL SOLID-STATE FORMULATIONS BY CONFOCAL FLUORESCENCE MICROSCOPY

*We shall not cease from exploration  
And the end of all our exploring  
Will be to arrive where we started  
And know the place for the first time.*

T. S. Eliot – excerpt from Little Gidding (1942)

Once biopharmaceuticals are purified, they are formulated in buffer and excipients under conditions that facilitate storage and administration to the patient. The next two chapters explore novel experimental techniques to characterize the structure of solid-state biopharmaceutical formulations. This chapter documents the use of confocal fluorescence microscopy to study structural features on particle-size length scales, and is adapted from a publication in *Molecular Pharmaceutics* with permission (Appendix E) [77]. The next chapter studies protein-size structural features using small-angle neutron scattering.

#### **3.1 Introduction**

Although most macromolecular biotherapeutics are administered as aqueous solutions by subcutaneous injection or intravenous infusion, sometimes there is a need to develop a solid-state formulation. Solid-state formulations help mitigate major

protein stability challenges, including chemical and physical degradation mechanisms, and enable long-term stability during storage and transport. Current research focuses on optimizing the drying processes and conditions and the resulting long-term stability of the biopharmaceuticals [22,78–80]. Even though dried formulations are typically reconstituted before administration, their physical characteristics, such as the solid-state particle morphology and particularly the protein distribution within, contain important information that could potentially impact long-term stability [22]. Although characterization of these physical properties is an active area of research, the technical issues can often be challenging due to the large range of length scales involved and the sensitivity of the formulations to external stimuli such as humidity and temperature.

Typical drying methods are lyophilization or freeze-drying and spray-drying, while less common alternatives include foam-drying, spray-freeze-drying, and spray-coating [78,81]. Irrespective of the drying method, a stabilizer such as a sugar is usually added, resulting in an amorphous dry formulation composed predominantly of the protein and the sugar. The microscopic morphology of solid-state formulations is known to depend strongly on the drying method. For example, lyophilization produces a macroscopic cake that can be readily broken down to thin flakes that are up to several hundred micrometers long, while spray-drying directly produces relatively smaller and more homogeneous spherical particulates that are a few micrometers in diameter [78]. Depending on the formulation components and process conditions, the spray-dried particles can be hollow, as opposed to dense spheres, due to fast drying kinetics and resulting shell formation of the solid components.

Although the ultrastructure of the dried powders is well-known and easily investigated through techniques such as scanning electron microscopy (SEM), the

internal protein distribution is less well-understood. However, understanding of the protein distribution throughout the solid phase and of effects such as protein-excipient segregation as a function of processing conditions is of particular interest to solid-state stability research. Protein-excipient segregation does not necessarily imply phase separation between the protein and the stabilizer, but rather indicates the presence of compositional heterogeneity throughout the dried particle volume, with certain regions enriched in protein while others are enriched in stabilizer.

Long-term stability of proteins depends on the local stabilizer-to-protein ratio and, consequently, variations due to compositional microheterogeneity may lead to inferior protein stability relative to that expected from the overall protein-to-stabilizer ratio. For example, several reports have shown a relationship between overall protein instability and protein surface accumulation in dried formulations [22,78,82,83]. Protein degradation rates are generally higher at interfaces [84], and both lyophilized and spray-dried particles have been shown to exhibit protein accumulation at the surface. In a lyophilized formulation, protein may adsorb to the interface between the ice crystals and the freeze-concentrated liquid during the freezing step and stay trapped there during the sublimation step. In a spray-dried formulation, the microheterogeneity can be much higher due to the fast nature of the drying kinetics, which can preferentially entrap the protein in certain regions of the final particle morphology due to diffusion limitations [85,86]. In both cases, the addition of surfactants has been shown to reduce the interfacial protein accumulation, but it is not known how surfactant addition affects the protein distribution in the particle interior [78,87,88]. Moreover, interest has grown in the use of alternative delivery routes that directly use solid-state biopharmaceutical powders, such as in oral and pulmonary

delivery and incorporation of the protein powders in controlled drug-release systems such as polymer implants and injectable microcapsules [89–91]. In these instances, the distribution of active ingredient throughout the solid phase is fundamental to the understanding and design of optimal drug-release characteristics.

Despite the importance of the protein distribution in solid-state formulations, it has not been investigated extensively, mainly because of the lack of an experimental technique that allows its direct measurement. Electron spectroscopy for chemical analysis (ESCA) is capable of measuring protein concentration by probing the elemental composition, but it has an analysis depth of only about 50 Å, which is insufficient to penetrate into the particle interior [78,83,87,88]. Conversely, confocal Raman microscopy (CRM) has been used to obtain three-dimensional chemical maps with high spatial resolution of frozen protein formulations, but is more challenging to use for dry formulations as samples suffer local heating due to laser power and longer acquisition times [92,93]. Differential scanning calorimetry (DSC) and solid-state nuclear magnetic resonance (ssNMR) can accurately detect protein-excipient phase separation, but cannot resolve the protein distribution throughout the sample volume [94]. Consequently, there is a need for a robust, accurate, and cost-effective method for mapping protein distribution within solid-state formulations with sufficient resolution to detect phase separation and microheterogeneity.

Here we have developed a straightforward and simple technique to visualize protein distribution in solid-state formulations by fluorescent labeling of the protein and the use of confocal fluorescence microscopy (CFM) after regular drying procedures. The use of CFM allows direct, three-dimensional imaging of dried biopharmaceutical formulations without additional sample preparation (beyond

standard fluorescent labeling) or extensive data analysis. This chapter describes the investigation of microheterogeneity in monoclonal antibody (mAb) and antibody fragment (Fab) formulations, all containing polysorbate 20 (PS20) as a surfactant. The effects of drying method, sugar type, and sugar content on the microheterogeneity were investigated: (1) lyophilization vs. spray-drying, (2) trehalose vs. sucrose as the sugar stabilizer, and (3) different sugar-to-protein ratios (S/P). This chapter shows that while the presence of surfactant limits protein accumulation at the solid-air interface, significant protein-sugar segregation is present in spray-dried samples, especially those with a low S/P. In contrast, lyophilized samples show uniform protein distribution throughout the bulk of the dried solid under all process conditions investigated.

## **3.2 Materials and Methods**

Sample preparation and initial characterization were done at Genentech Inc. (South San Francisco, CA), while we completed electron and confocal fluorescence microscopy studies at the University of Delaware.

### **3.2.1 Materials**

A recombinant humanized mAb of the IgG1 sub-class (mAb1) and a model antibody fragment (Fab1) [91] were manufactured by Genentech. Alexa Fluor 488 was purchased from Thermo Fisher (Eugene, OR), polysorbate 20 from Pattern Chemical Mfg. Corp. (Gardena, CA), trehalose dehydrate from Ferro Pfanstiehl Laboratories (Cleveland, OH), and sucrose from Sigma (St. Louis, MO).

All formulations contained 10 mg/mL protein prior to drying and 0.01% (w/w) PS20, and either trehalose or sucrose in different sugar-to-protein ratios (S/P),

ranging from 0 (0 mg/mL sugar) to 10 (100 mg/mL sugar). MAb1 formulations were prepared in 4 mM histidine-HCl buffer, pH 6, while Fab1 formulations were prepared in 10 mM histidine-HCl buffer, pH 5.5. An overview of the composition and process conditions of each sample is provided in Table 3.1.

Table 3.1: Overview of the composition and process conditions of the samples investigated.

Sample number	Protein	Drying Process	Sugar	S/P Ratio (mass)	Moisture Content (%)
1	mAb	Spray-dried	Trehalose	1	0.59
2	mAb	Lyophilized	Sucrose	10	/
3	mAb	Spray-dried	Trehalose	10	0.56
4	mAb	Lyophilized	No Sugar	0	0.91
5	Fab	Lyophilized	Sucrose	1	0.42
6	mAb	Lyophilized	Trehalose	1	0.84
7	mAb	Lyophilized	Trehalose	10	0.52

### 3.2.2 Conjugation with Fluorescent Dye

N-hydroxysuccinimide (NHS ester) activated Alexa Fluor 488 [95] (6 mg) was dissolved in 0.6 mL dimethylsulfoxide (DMSO) and slowly added to 8 mL of mAb or Fab (103 mg/mL) in 100 mM sodium bicarbonate solution at pH 8.3 for the conjugation reaction to take place. The contents were mixed at room temperature under dark for 60 min and loaded onto PD-10 desalting columns to reduce the free dye in the mixture. The eluate from the PD-10 column was transferred to a dialysis cassette (MWCO 10 kDa) and dialyzed extensively against pH 6.0 buffer containing 4 mM histidine-HCl. Alexa Fluor conjugated mAb or Fab was recovered from the cassette and further passed through a HiPrep 26/10 desalting column (Amersham

Biosciences, Little Chalfont, United Kingdom) using an ÄKTA Avant (GE Healthcare Life Sciences, Pittsburgh, PA) purification system to remove the excess unconjugated free dye in the sample. The mole ratio of conjugated dye to protein was 0.706. The purified sample from the ÄKTA run was mixed with unlabeled protein in a 1/100 ratio to reduce the fraction of labeled protein in the samples to less than 1% before spray-drying or lyophilization.

### **3.2.3 Spray-Drying**

mAb1 was formulated at 10 mg/mL in pH 6.0 buffer containing 4 mM histidine-hydrochloride (histidine-HCl) with 0.01% (w/w) PS20, and a calculated amount of trehalose dihydrate or sucrose was added to achieve the desired sugar-to-protein ratio on a weight basis. The aqueous protein formulation was spray-dried using a B-191 Mini Spray Dryer (Buchi, New Castle, DE) equipped with a 1 L cyclone particle separator to prepare micron-sized particles. The inlet temperature was set at  $89 \pm 2$  °C, with 100% aspirator capacity at 9.11 L/s gas flow rate. The atomizing air flow rate was set at 19.66 L/min and liquid feed rate at 3.4 mL/min. This resulted in an outlet temperature of  $59 \pm 2$  °C. The spray-dried powder was collected in a clean dry glass vial and stored under vacuum till further use.

### **3.2.4 Lyophilization**

The samples were taken in 2 mL glass vials and lyophilized in a SP Scientific Advantage Pro lyophilizer (Gardiner, NY). The volume of solution in each vial was 0.5 mL. The lyophilization cycle was run with conservative drying settings known from experience to produce acceptable lyophilized material. The freezing shelf temperature and freezing rate were set at  $-35$  °C and 0.3 °C/min respectively. The

primary drying temperature and chamber pressure were  $-20\text{ }^{\circ}\text{C}$  and  $100\text{ }\mu\text{m Hg}$  respectively. The primary drying time was determined from the differential pirani/capacitance measurement. The secondary drying temperature, chamber pressure and drying time were  $25\text{ }^{\circ}\text{C}$ ,  $100\text{ }\mu\text{m Hg}$  and 10 h respectively. The ramp rates between drying steps were  $0.2\text{ }^{\circ}\text{C}/\text{min}$  and the headspace pressure was  $760\text{ mm Hg}$ . This lyophilization process typically produces solid cakes with moisture content of less than 1%.

### **3.2.5 Moisture Content Determination**

The moisture content of the spray-dried and lyophilized formulations was determined by a Coulometric Karl Fischer (KF) titration (Mettler-Toledo C30, Columbus, OH) equipped with a diaphragm-less electrode and solvent manager. Approximately 30 mg of spray-dried/lyophilized sample was weighed into vials to which 0.5 – 1 mL methanol was added in order to extract the moisture from the samples. The samples were kept for 10 min before starting the potentiometric titration. To start the analysis the samples were injected into the titration cell with Hydranal Coulomat<sup>®</sup> Water Standard (Sigma-Aldrich, St. Louis, MO). The sample injection was done manually using a Hamilton Syringe (Sigma-Aldrich) with a 20 G needle. The analysis was done using Mettler-Toledo-Software LabX 2014. The results of this analysis are included in Table 3.1.

### **3.2.6 Size-Exclusion Chromatography**

Size-exclusion chromatography (SEC) was performed on a TOSOH TSK-Gel Super SW3000 ( $7.8\text{ mm} \times 300\text{ mm}$ ) column using an Agilent 1200 series HPLC system equipped with a diode array detector (DAD). Samples were eluted at  $30\text{ }^{\circ}\text{C}$  in

isocratic mode with 0.20 M  $K_3PO_4$ , 0.25 M KCl, pH 6.2 as the mobile phase at a flow rate of 0.5 mL/min. Prior to analysis, samples were diluted to approximately 1.0 mg/mL in water and 100  $\mu$ L sample was injected. The total run time was 30 min and absorbance at 280 nm and 495 nm was used for detection of the dye-conjugated mAb1 as well as confirmation of removal of all free dye. The SEC peaks were divided into monomer, high molecular weight species (HMWS), and fragments. The percent peak area at 280 nm was calculated by dividing the peak area of each group at each time point by the total peak area.

### **3.2.7 Scanning Electron Microscopy**

Scanning electron microscopy (SEM) was used to characterize the morphology of the dried powders resulting from different process conditions. The powder morphologies were studied for samples as received and through particle cross-sections. For the former, the powder was mounted on double-sided carbon tape on an aluminum SEM stub and sputter-coated with Au-Pd in a Denton Bench Top Turbo III (Denton Vacuum, Moorestown, NJ) for 180 s at 25 mA. For the latter, the powders were embedded in LR White acrylic resin and UV-polymerized, then cut with a glass knife to expose cross-sections of the particles. The cut surface of the block was exposed to osmium tetroxide crystals for 6 h to induce contrast between the particles and the resin. All samples were imaged on a Hitachi S4700 field-emission scanning electron microscope (Tokyo, Japan).

### **3.2.8 Confocal Fluorescence Microscopy**

Dried powders containing labeled proteins, prepared as described above, were imaged both as received and after suspension in immersion oil (Zeiss Immersol 518F,

refractive index 1.52) on a Zeiss LSM 710 laser scanning confocal microscope (Jena, Germany). The use of immersion oil allowed higher resolution and transparency of the confocal image without influencing the powder morphology within the time span of the experiment. The optical resolution of the instrument was approximately 0.15  $\mu\text{m}$ , while the pixel size was below 0.14  $\mu\text{m}$  in the focal plane (x/y-direction) and below 0.4  $\mu\text{m}$  out of the focal plane (z-direction) for all images.

### 3.3 Results

The solid-state formulation particle morphologies for both the spray-dried and lyophilized samples were imaged using SEM (Figure 3.1). While spray-drying directly yields micron-sized particles that are nearly spherical in shape, lyophilization and subsequent mechanical breakdown of the cake yields thin flakes that can be several hundred micrometers long.

Although the three-dimensional images obtained by CFM are not shown here (available online as Supplemental Information [77]), the same morphologies as observed in SEM are apparent in the maximum-intensity projections of the CFM image stacks, which are basically top-down views of the three-dimensional images. Figures 3.2a, e, and g show the maximum-intensity projections for mAb1 in a trehalose formulation that was spray-dried with  $S/P = 1$ , spray-dried with  $S/P = 10$ , and lyophilized with  $S/P = 10$ , respectively. The maximum-intensity projections illustrate how CFM can make particles virtually transparent and highlight the protein distribution through the fluorescence signal. Spray-dried particles with low  $S/P$  form hollow and often collapsed particles that resemble deflated balls or

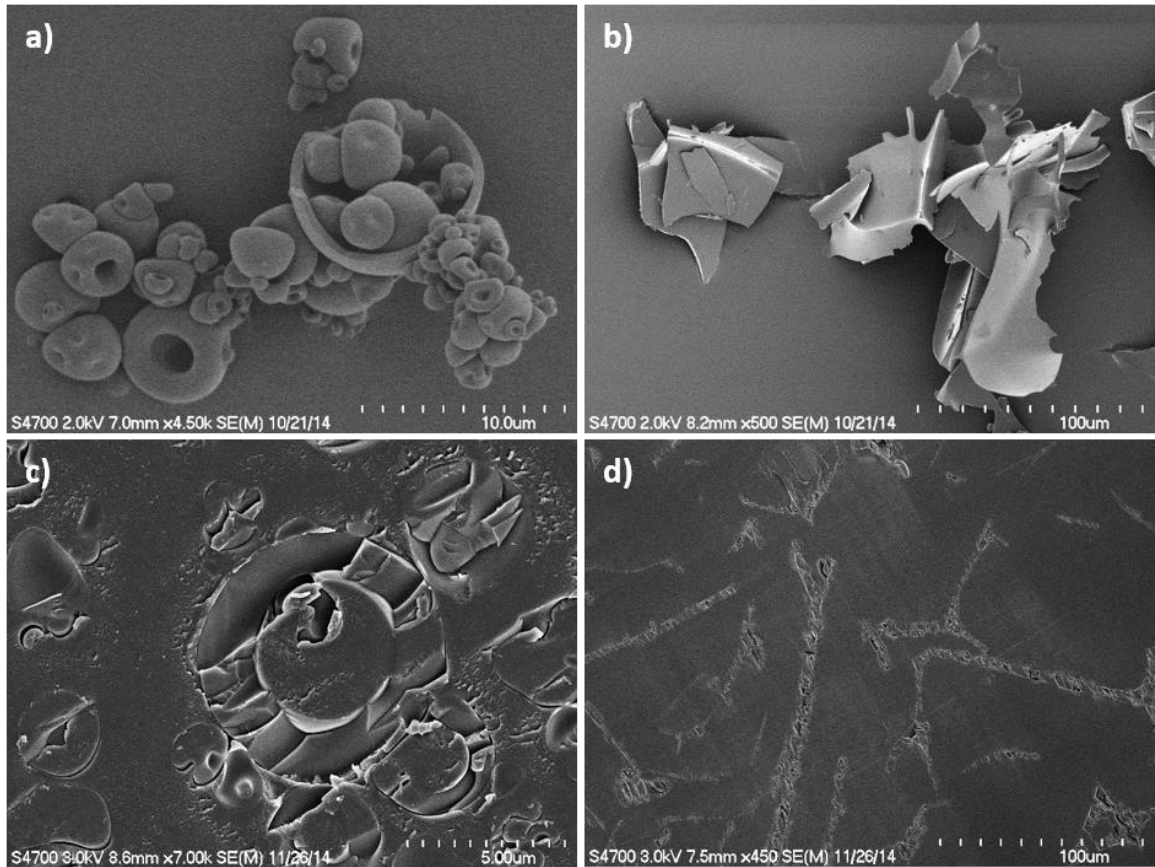


Figure 3.1: Typical scanning electron microscopy (SEM) images for spray-dried and lyophilized biotherapeutics. The top row shows SEM images of (a) a spray-dried powder and (b) a lyophilized powder as received, while the bottom row shows cross-sections of the same formulations after embedding in an acrylic resin. While formulations with Fab1 and a trehalose-to-protein ratio of 1 were used in all the images shown, mAb1 formulations showed similar morphologies.

doughnut-like particles (Figure 3.2a), but at higher S/P the particles are dense and more spherical (Figure 3.2e). In both cases, the protein distribution is heterogeneous to some degree, such that protein-sugar heterogeneity is clearly observable via the relative fluorescence intensities. A decrease in protein concentration does not necessarily imply a change in local protein-sugar ratio. Instead, it is conceivable that

the protein-sugar ratio remains the same but that the overall mass density of the solids changes throughout the particle microstructure. However, if this is the case, a change of internal particle morphology and, specifically, an increase in porosity would be expected where the mass density is lower. SEM imaging does not reveal any significant morphological changes throughout the particles in any of the samples investigated (Figure 3.1). This indicates that overall mass density fluctuations of the solids, although potentially present to a lesser degree, are not a significant cause of the observed heterogeneity in protein distribution. Hence, even though this method does not directly detect the distribution of the sugar, the assumption of constant mass density leads to the conclusion that the outside of the particles is generally enriched in protein and, consequently, the interior is richer in sugar, creating a radial gradient through the particle wall. Conversely, the flake-like lyophilized particles appear homogeneous in the maximum-intensity projection (Figure 3.2g).

The microheterogeneity, or lack thereof, is more clearly observable by investigating cross-sections of individual particles, as illustrated in Figure 3.2b, which shows a cluster of spray-dried particles at low S/P, and Figures 3.2c, d, f, and h, which show magnified regions of individual spray-dried and lyophilized particles. Intensity line profiles across the particles are indicated in red dashed lines in Figure 3.2 and are plotted in Figure 3.3. Note that these cross-sections are obtained as a 'layer' centered on the focal plane of the focused CFM that is approximately 0.4  $\mu\text{m}$  in depth. The figure compares the intensity profiles for a spray-dried particle at low S/P and at high S/P (Figure 3.3a and b), as well as the intensity profiles for a lyophilized particle perpendicular (through the flake) and parallel (along the flake) to the plane of the flake (Figure 3.3c).

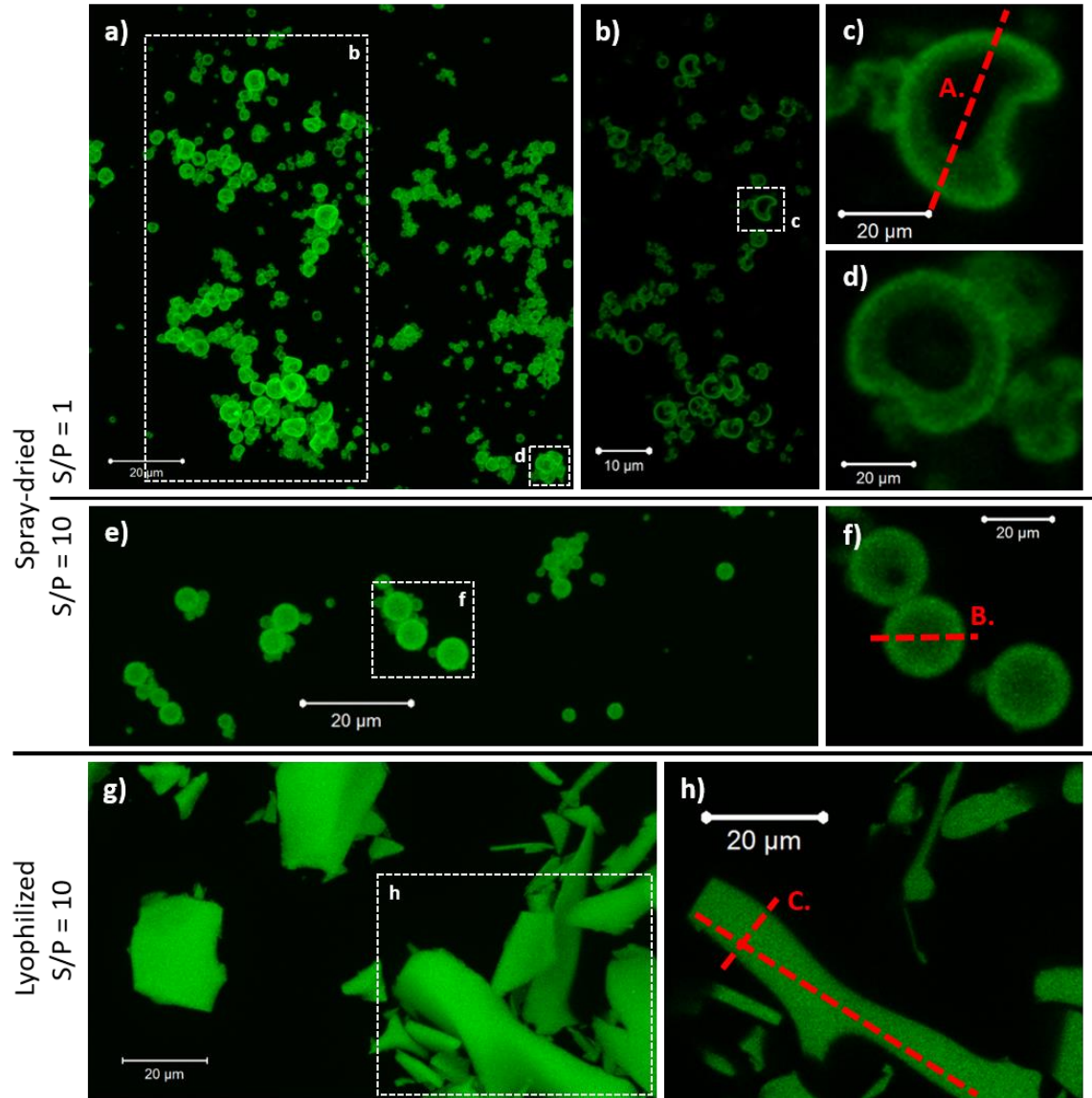


Figure 3.2: Confocal fluorescence microscopy (CFM) images of two spray-dried (top and middle) mAb1 formulations and a lyophilized (bottom) mAb1 formulation with trehalose-to-protein ratios (S/P) of 1 (top) and 10 (middle and bottom). The mAb1 protein in each formulation was conjugated to Alexa Fluor 488 dye with a labeling ration of 1%. The images on the left (a, e, and g) contain maximum-intensity projections of the full three-dimensional image stacks, while the images towards the right (b, c, d, f, and h) contain single cross-sections. The red dashed lines delineate the intensity profiles shown in the corresponding panels in Figure 3.3.

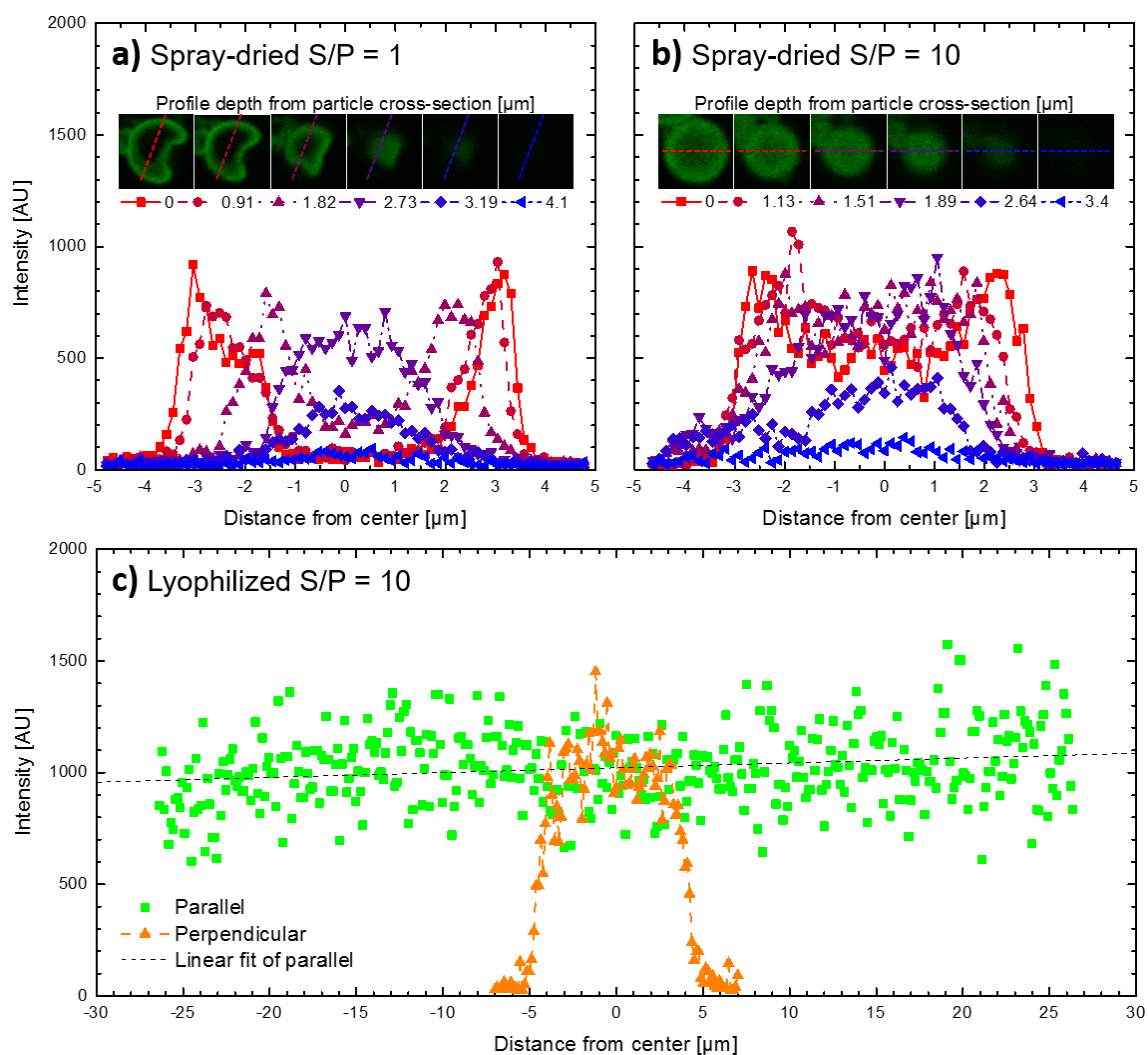


Figure 3.3: CFM intensity line profiles for the cross-section of two spray-dried mAb-trehalose particles with varying S/P (top) and for a lyophilized, flake-like mAb-trehalose particle parallel and perpendicular to the flake (bottom). The profile lines are shown in Figure 3.2 as red dashed lines, which show the cross-sections of the particles at the approximate particle center (corresponding to a depth of 0  $\mu\text{m}$ ). All distances are reported as measured from the approximate particle center. For the spray-dried particles, the profile at different particle depths is shown, representing the three-dimensional particle structure.

For the spray-dried particles, profiles are shown along the same scan line but at different depths within the particles, thus providing a direct view of the three-dimensional distribution of protein within the particles. Note that the intensities shown here are not absolute. The strongest heterogeneity is observed in the spray-dried particle at low S/P, which has a hollow core and a distinct gradient throughout the shell. At higher S/P, the spray-dried particles still display heterogeneity in the radial direction but to a lesser degree. Lyophilized particles indeed show homogeneous intensity profiles, as indicated by the intensity profile along the length of the flake-like particle. When viewed through the thickness of the particle, the intensity inside the particle is also homogeneous. Note that the intensity profile through the thickness of the flake includes the particle edge, while the profile along the length of the profile does not contain the particle edge (Figure 3.2h). These profiles for lyophilized formulations were observed for mAb1 and Fab1 formulations regardless of sugar type (sucrose or trehalose) or S/P (0, 1, and 10) (additional images included in Appendix B).

### **3.4 Discussion**

The spray-dried and lyophilized particle morphologies, as depicted in the SEM and CFM images, agree well with those reported in the literature (Figure 3.1 and 3.2) [78,89]. The formation of hollow particles during spray-drying is an effect of kinetic limitations during the very fast drying and subsequent protein crowding near the rapidly shrinking liquid-air interface, a well-known phenomenon in the drying of colloidal solutions [96–98]. When the local protein concentration increases to high values at the droplet periphery, the viscosity also increases sharply and a rigid shell is formed at the air-water interface. While water continues to evaporate from the particle

interior, a hollow particle is formed that may collapse upon further drying [98]. When the sugar-to-protein ratio increases, the total solids concentration in the solution increases and the effective protein concentration in the dried solid decreases, such that shell formation occurs at greater shell thicknesses, which reduces the chance of collapse. Intuitively, the same mechanism is potentially responsible for the protein-sugar heterogeneity observed in the spray-dried formulations (Figure 3.3a and b).

For spray-dried formulations, protein crowding at the interface can be caused by two non-exclusive effects: (1) protein adsorption at the liquid-air interface, and (2) protein crowding at the particle periphery due to the receding interface and peripheral water flow from the center of the particle outward, as described above. Both of these effects are enhanced by the high molecular weight and hence low mobility of mAbs. For example, a study of desiccated sessile droplets of a lysozyme and trehalose formulation showed clear accumulation of both trehalose and lysozyme at the particle periphery, with the lysozyme-to-trehalose ratio increasing sharply at the particle interface [85]. Proteins are known to have a high affinity for adsorption at interfaces, which will lead to a high protein concentration near the particle surface when the droplet diameter decreases quickly during drying [86,99]. Such protein accumulation at the surface can negatively affect long-term stability due to low local protein-to-stabilizer ratios [22,78,82,83]. However, addition of surfactants significantly reduces protein adsorption at the interface, as has been shown by electron spectroscopy for chemical analysis (ESCA) measurements [78,87,88]. Hence, in this work, in which PS20 was included as a surfactant in all formulations, protein-sugar heterogeneity was presumably caused mainly by the second mechanism.

For lyophilized formulations, where the second mechanism is not present, all formulations investigated showed homogeneous protein distributions. Although proteins tend to accumulate at the ice crystal and freeze-concentrated liquid interface during the freezing step [86], here, too, the addition of surfactant has been shown to reduce protein accumulation at the surface. This seems to be confirmed in the perpendicular profiles through the lyophilized flakes in Figure 3.3c, which do not show an increase in protein concentration at the particle interface. However, small increases in protein concentration at the particle surface might not be detected by CFM due to resolution limits. CFM has an optical resolution of approximately 0.15  $\mu\text{m}$ . For comparison, ESCA can determine the protein concentration at the surface up to a depth of approximately 50  $\text{\AA}$ , which is well below the resolution of CFM. Hence, while CFM can obtain the bulk protein distribution, ESCA can give complementary information about the protein concentration at the surface. Interestingly, frozen protein solutions have also been shown to have a homogeneous distribution in the freeze-concentrated phase of lysozyme and trehalose formulations, using confocal Raman microscopy (CRM) [92]. This indicates that during the sublimation step of lyophilization the protein distribution in the freeze-concentrated liquid does not change significantly.

In general, confocal fluorescence microscopy is a straightforward and reliable technique for imaging protein distribution in solid-state formulations. It allows sufficient transparency to create full three-dimensional images of particles in these size ranges and has the resolution required to observe microheterogeneity of protein and stabilizer. One of the greatest advantages of CFM is that once a small amount of protein is labeled, all drying processes can be executed without changes in regular

protocols and samples can be viewed directly without further sample preparation. As such, it is suited for the further investigation of protein-stabilizer heterogeneity, both for understanding its effects on long-term stability as well as in the design of the controlled drug-release profiles. The possibility of acquiring intensity profiles throughout the particle, as illustrated in Figure 3.3a and b, allows for future characterization and modeling of the drying processes.

Two potential concerns regarding the use of CFM are (1) that protein-sugar phase separation, with domains consisting entirely of sugar, are not detected and (2) that the 1% labeled protein interacts differently in solution or with the sugar as compared to the unlabeled protein, misrepresenting the actual unlabeled protein distribution. The first issue is easily solved by taking simultaneous confocal and regular optical microscopy images. In this work, no formulations showed regions by optical microscopy that did not overlap with the fluorescence signal, indicating there was no protein-sugar phase separation at these length scales. Regarding the second issue, labeling a monoclonal antibody with a fluorescent tag increases the molecular weight by less than 1%. Hence, the mobility of the molecules is not significantly altered. In addition, the Alexa Fluor fluorescent labels are, by design, net negatively charged to increase hydrophilicity and generally reduce self-association [95]. In a few cases, however, this net negative charge has been shown to lead to electrostatic interactions with positively charged interfaces or structures. For this work, a comparison of SEC data of formulations with and without labeled protein showed no significant change in the presence of protein aggregates, indicating that protein-protein interactions are not significantly altered by the presence of the label.

### **3.5 Conclusions**

Confocal fluorescence microscopy is capable of detecting microscale segregation of monoclonal antibodies (mAbs) and excipients in solid-state biopharmaceutical formulations. While lyophilization procedures for a model IgG1 mAb generally lead to a uniform protein-excipient distribution, specific spray-drying conditions can lead to distinct protein-excipient microheterogeneity. Microheterogeneity is observed in spray-dried particles as a radial increase in protein concentration towards the periphery, and is hypothesized to be caused by proteins being kinetically trapped at the quickly receding water-air interface, a well-known phenomenon in the drying of colloidal solutions. Due to addition of polysorbate 20, protein surface adsorption was limited and not a direct cause of protein heterogeneity in this study.

## Chapter 4

### ***IN SITU* CHARACTERIZATION OF THE MICROSTRUCTURAL EVOLUTION OF BIOPHARMACEUTICAL SOLID-STATE FORMULATIONS WITH IMPLICATIONS FOR PROTEIN STABILITY**

The results presented in the previous chapter showed that while microheterogeneity on a particle scale can be detected in certain spray-dried formulations, it does not lead to an observable increase in irreversible aggregation in these formulations. Instead, we would expect that the structure on the molecular scale is the more critical factor in determining formulation stability. Consequently, the characterization of the protein-scale microstructure of solid-state formulations, particularly under the effect of changing environmental conditions, is the focus of this chapter, which is adapted from a submission to *Molecular Pharmaceutics* [100].

#### **4.1 Introduction**

Solid-state formulations of biopharmaceuticals, such as lyophilized or spray-dried proteins, are developed to provide protein stability during transport and long-term storage as discussed in the previous chapter. Solid-state formulations are also used in drug-delivery systems as alternatives to the usual intravenous infusion or subcutaneous injection, like pulmonary delivery of powders or sustained drug-release devices such as polymer implants, microspheres, or solvent-depots [78,81,89–91]. However, the formation of protein clusters as irreversible aggregates is a prevalent form of instability in biopharmaceutical formulations, and the presence of such

aggregates can have a negative impact on the drug's efficacy as well as lead to undesired immunogenicity or toxicity of the drug [22].

To delay or prevent aggregation in the solid state, lyophilization and spray-drying are performed with stabilizers (such as sugars) and other additives (such as surfactants). While it is generally accepted that these stabilizers protect the protein from degradation in the solid state, the precise mechanism of stabilization is still an active topic of current research [22,78–80,101,102]. Though there has been significant work on the role of stabilizing sugars as a replacement for water molecules and on the molecular physics of the sugar, water, and amino acid interactions [22,101], less is known about the protein-scale microstructure in these solid-state formations. This is especially relevant given that the protein molecules are in a highly crowded local environment due to the high protein concentration in the solid state, which can easily reach 50 – 80% by mass in typical formulations. In the previous chapter, we elucidated the micron-scale protein heterogeneity of these formulations using confocal fluorescence microscopy (CFM) [77], where differences in protein heterogeneity suggested that a protein-scale microstructural investigation is warranted. To address these challenges, we demonstrate how protein-scale structure can be resolved in these formulations *in situ* by small-angle neutron scattering, where contrast between protein and excipients can be achieved by deuteration.

Protein stability can be informed by the multiscale structural characterization of solid-state formulations, which encompasses knowledge of (1) the morphology and size of the solid-state particles, (2) the protein-stabilizer microheterogeneity, and (3) the presence of protein clusters or aggregates. Protein degradation has been shown to be more likely at the particle surface, and is determined by the particle morphology,

size, and protein distribution within the solid-state particles [22,78,82–84]. These factors also influence the reconstitution efficiency and the release rate during sustained drug-release applications [81,91]. Chapter 3 demonstrated that, while particle-scale microheterogeneity is significant in spray-dried formulations, it is generally not observed in lyophilized formulations. Importantly, the observed microheterogeneity itself did not lead to an increase in irreversible aggregation in the formulations investigated, indicating that particle-scale microheterogeneity is not a sufficient condition for formulation instability. This is consistent with the expectation that the microheterogeneity on protein (nanometer) length scales, and not on particle length scales, is the most critical structural issue affecting protein stability. However, measuring molecular structural features on molecular length scales *in situ* in these solid-state formulations is extremely challenging. There is insufficient contrast between the protein and excipients for direct electron microscopy or X-ray scattering methods. However, the ability to selectively deuterate the sugars, or as is shown here, to introduce a controlled amount of deuterated water, provides a method to determine the average local protein environment via neutron scattering methods.

Just as in the case of determining the protein distribution in chromatographic resins in Chapter 2, small-angle neutron scattering (SANS) is well-suited to capture protein-scale structural information from these solid-state formulations as it (1) can probe features on nano- to micrometer length scales, (2) is minimally disruptive (as opposed to X-rays), (3) can penetrate opaque materials to determine internal structure, and (4) can sample relatively large volumes [44–47,51]. Recently, SANS has been used to characterize the protein microstructure in solid-state formulations, mainly in the frozen state but also in lyophilized formulations of model proteins [51,73,74].

Scattering patterns show a single protein-protein interaction peak, which indicates a crowded amorphous morphology with average separation distances on the order of the protein molecular dimensions. Consequently, SANS has the potential to probe the protein aggregation and protein-excipient distribution in these systems. A distinct advantage of SANS over other methods is the ability to create scattering contrast between the proteins and excipients by isotopic labeling, uniquely enabling SANS to measure excipient and protein molecular distributions [51].

Related but distinctly different techniques have recently been suggested as methods to predict the long-term stability of proteins in the solid-state, such as solid-state hydrogen-deuterium exchange with mass spectrometry (ssHDX-MS) and neutron backscattering (NB) [22,102–106]. Similar to SANS, ssHDX-MS uses isotopic labeling to determine the amino acids that more readily exchange hydrogens upon exposure of the solid-state formulation to deuterated water vapor. These measurements have been shown to correlate with long-term stability, providing a potential route to predict formulation stability [102–104]. Similarly, NB probes molecular dynamics of hydrogens in the formulation on fast time scales, and consistent with the prevailing thinking, faster molecular dynamics are implicated in limiting protein stability in the solid state [22]. While both of these methods show promise in predicting long-term stability by informing about the molecular-scale dynamics, important questions remain about the protein-scale microenvironment in these solid-state formulations as well as about whether any small aggregates may be present in such formulations in the solid state.

Here we report a new method that exploits contrast variation and SANS to measure the protein-scale microstructure of several biotherapeutic monoclonal

antibody (mAb) and antibody fragment (Fab) formulations *in situ* in the lyophilized or spray-dried state. In addition to identifying differences in structure of initially stable formulations, we have also investigated the effects of exposure to humidity and elevated temperature. An enhanced vapor cell SANS sample environment (VC-SANS) [107] was constructed that enables the measurement of the effects of cycling humidity on the protein-scale structure *in situ*. The resulting findings contribute to our fundamental understanding of protein behavior in solid-state formulations and highlight the potential of (vapor cell) SANS to further explore this behavior for different formulations and conditions.

## 4.2 Experimental Section

### 4.2.1 Materials and Sample Preparation

A recombinant humanized mAb of the IgG1 sub-class (mAb1) and a model antibody fragment (Fab1) were manufactured by Genentech Inc. (South San Francisco, CA). Polysorbate 20 (PS20) was purchased from Pattern Chemical Mfg. Corp. (Gardena, CA), trehalose dehydrate from Ferro Pfanstiehl Laboratories (Cleveland, OH), and fully deuterated sucrose ( $C_{12}^2H_{14}H_8O_{11}$ ) from Omicron Biochemicals Inc. (South Bend, IN).

All formulations contained 10 mg/mL protein prior to drying, 0.01% (w/w) PS20, and 10 mg/mL of either trehalose or sucrose, which corresponds to a sugar-to-protein ratio (S/P) of 1. MAb1 formulations were prepared in 4 mM histidine-HCl buffer, pH 6, while Fab1 formulations were prepared in 10 mM histidine-HCl buffer, pH 5.5. An overview of the composition and process conditions of each sample is provided in Table 4.1. A heat-stressed formulation (F3) was obtained by maintaining a

regular lyophilized mAb1 formulation (F1) at 110 °C for 5 hours. The spray-drying, lyophilization, moisture content determination, and size-exclusion chromatography (SEC) was completed at Genentech and followed the procedures outlined in Chapter 3. The results of the moisture content determination and SEC analysis are included in Table 4.1. The lyophilized, solid cakes were manually broken up to allow loading in the SANS sample cell, so that the particle-scale morphologies and protein distributions in the loaded lyophilized and spray-dried formulations correspond to those described in Chapter 3 (Figure 3.2) [77].

Table 4.1: Overview of the composition and process conditions of the formulations investigated.

Formulation	Basic composition	Sugar	S/P ratio	Moisture content [%]	Drying process	Aggregate content [%]
F1	10 mg/mL mAb1; 4 mM L-His/HisHCl pH 6.0; 0.01% (w/v) polysorbate 20	Trehalose	1	<2	Lyophilized	3.7-6.5
F2		Deuterated sucrose	1	<2	Lyophilized	/
F3		Trehalose	1	<2	Lyophilized	15.3 (heat-stressed)
F4	10 mg/mL Fab1; 10 mM L-His/HisHCl pH 5.5; 0.01% (w/v) polysorbate 20	Trehalose	1	3	Lyophilized	1
F5		Trehalose	1	7	Spray-dried	1

#### 4.2.2 Small-Angle Neutron Scattering

The basic background of small-angle neutron scattering (SANS) is discussed in Section 2.2.2.1. Note that the magnitude of the momentum transfer vector is denoted in this chapter by  $q$ , as opposed to  $Q$  in Chapter 2. Because the SLD of a typical protein and sugar are similar, structural features of proteins within a sugar matrix are

generally not observed by SANS (Figure 4.1). However, as proteins and sugars contain exchangeable hydrogens, the SLD is a function of the extent of deuterium exchange. Figure 4.1 illustrates that there are two straightforward methods to increase the contrast for a specific formulation: (1) use deuterated sugars (or proteins) and (2) introduce deuterium oxide ( $D_2O$ ) into the system. Both methods are used in this chapter and provide complementary information.

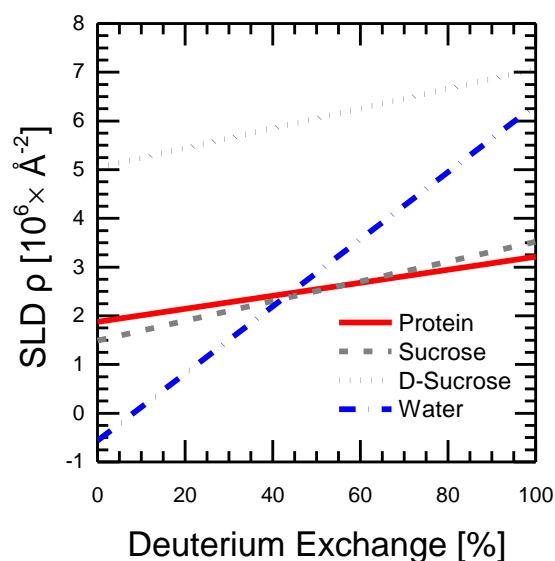


Figure 4.1: Schematic of the neutron scattering length densities (SLDs) of a typical mAb, sucrose, fully deuterated sucrose, and water as a function of the amount of deuterium exchange of exchangeable hydrogens of each molecule.

The experiments were carried out on the 10 m NGB (nSoft) SANS instrument at the NIST Center for Neutron Research (NCNR), National Institute of Standards and Technology (NIST), Gaithersburg, MD. The instrument settings for the tests were:

- high  $q$ : 1.2 m sample-to-detector distance (SDD) with 5 Å neutrons for a 600 s count time,
- intermediate  $q$ : 4.5 m SDD with 5 Å neutrons for a 1200 s count time, and
- low  $q$ : 4.5 m SDD with lenses with 10 Å neutrons for a 1500 s count time.

When spliced together, these regions result in a scattering range  $0.004 \text{ \AA}^{-1} < q < 0.6 \text{ \AA}^{-1}$ , corresponding to length scales ranging from approximately 1600 Å to 10 Å. The wavelength spread was 0.15 for all samples.

For time-resolved vapor cell studies, data were collected in time bins of 360 s at the high- $q$  instrument setting, with intermittent full-range scans approximately every 4.5 h to probe the structural integrity of the samples. Sample cells with demountable quartz windows and a path length (thickness) of 1 mm were used for static experiments, while the NIST vapor cell described below was used for all time-resolved experiments. Standard data reduction procedures were followed to reduce the data to radially-averaged patterns [53].

### 4.2.3 Vapor Cell

The vapor cell used at NIST consists of a titanium cell with quartz windows, as shown schematically by Shelton *et al.* [107]. The setup of the vapor cell SANS experiment is depicted in Figure 4.2. The cell has a vapor inlet at the top and a vapor outlet at the bottom, allowing vertical vapor flow throughout the sample chamber, and it can be temperature-controlled from approximately 5 to 90 °C. The cell is connected to a nitrogen source via a flow path that can be toggled to allow flow through or to bypass a bubbler filled with water. The bubbler was held at 20 °C while the vapor cell was at 25 °C to prevent vapor condensation in the connecting lines and vapor cell. The

sample powders were mounted into the sample chamber within an aluminum foil pocket, which was open at the top to allow vapor exchange with the sample chamber. Samples were exposed to either a continuous pure nitrogen ( $N_2$ ) gas flow or a mixed  $D_2O$ - $N_2$  or  $H_2O$ - $N_2$  vapor flow for periods of several hours, while the SANS patterns were collected in time bins of several minutes.

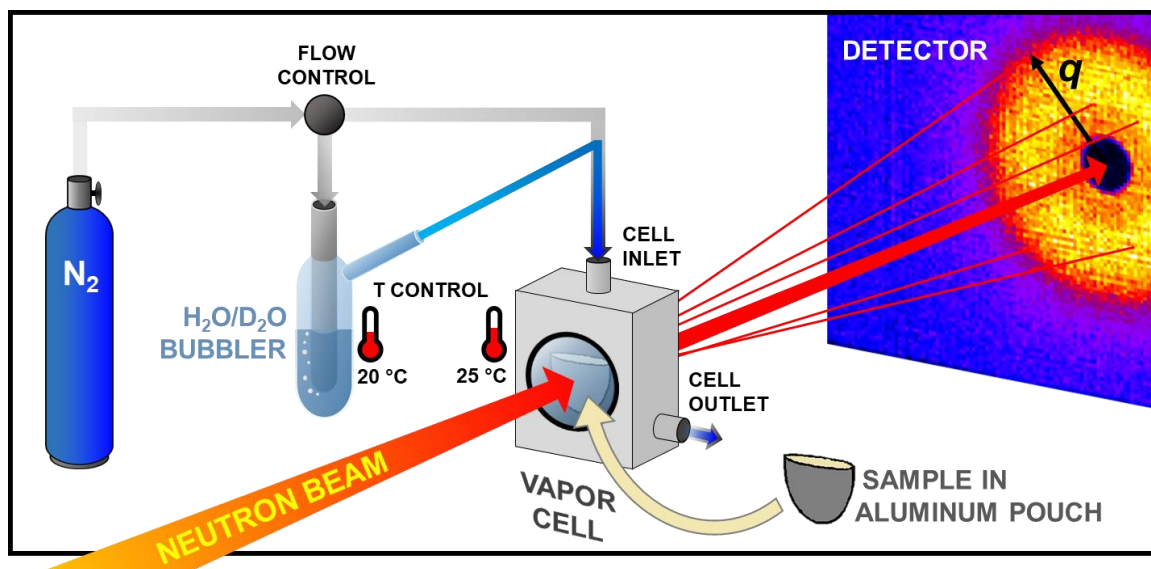


Figure 4.2: Schematic of the vapor cell set-up employed at the NCNR.

### 4.3 Results and Discussion

The nano-scale microstructure of five different solid-state monoclonal antibody (mAb) and antibody fragment (Fab) formulations, listed in Table 4.1 was investigated using small-angle neutron scattering (SANS). The static microstructure of the formulation was first probed using regular SANS, then microstructural changes under the influence of water uptake were investigated using SANS in a vapor cell

environment (VC-SANS). Quantitative agreement was observed between the initial structures measured in the standard demountable cells and the VC-SANS cell.

### 4.3.1 Static Microstructure

A typical SANS pattern of a solid-state biopharmaceutical formulation, represented by Formulation F1, is shown in Figure 4.3 (blue). The pattern shows flat background scattering at high  $q$ -values (small length scales), and power-law behavior, with a slope of  $-4$ , at small  $q$  values. This Porod slope indicates scattering from the sharp surface of the micron-sized particles that comprise the solid formulation. In the case of a lyophilized formulation, these are the thin platelet-like particles resulting from the crushing of the lyophilized cake, while for a spray-dried formulation these are the hollow spherical particles as observed by confocal fluorescence microscopy (Figure 3.2) [77]. The background evident at high  $q$  is due to incoherent scattering that arises mainly from hydrogen atoms.

The scattering pattern of the typical formulation without deuteration lacks any features that correspond to the internal structure of the dried powders – the structure of protein molecules distributed in the excipient – because of the lack of contrast between the excipient and the protein (Figure 4.1). Figure 4.3 shows that using fully deuterated sucrose as an excipient in Formulation F2 enhances the contrast between the protein and the sugar phase sufficiently to obtain protein-scale structural information from SANS. Here this structural information appears in the form of a single broad peak at intermediate  $q$  values.

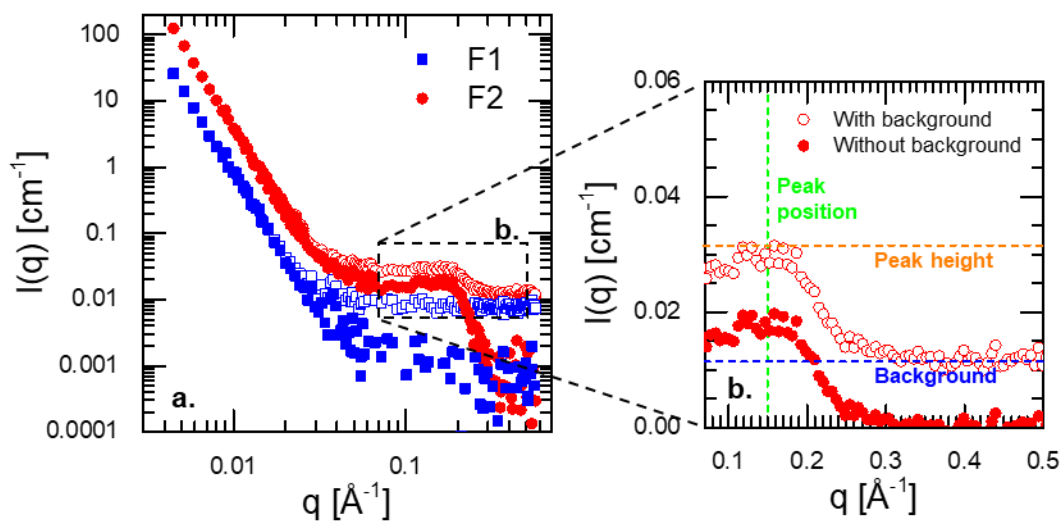


Figure 4.3: Comparison of SANS patterns of a lyophilized mAb1 sample in regular (F1) and deuterated (F2) sugar (a) and overview of prominent scattering metrics reported in the time-resolved experiments (b). Open symbols show the scattering patterns before subtraction of the incoherent scattering background, while filled symbols show the patterns after subtraction. The dashed box indicates the area of the pattern highlighted in the time-resolved vapor cell experiments (Figure 4.4).

Such a peak has been observed before in lyophilized formulations of model proteins such as lysozyme as well as in frozen mAb formulations, and is characterized as a nearest-neighbor peak or a protein-protein interaction peak because the peak position corresponds to the average protein-protein distance in the amorphous formulation [51,73,74]. In Figure 4.3 the observed peak position of  $0.15 \text{\AA}^{-1}$  corresponds to an average protein-protein center-to-center separation distance of  $d = 42 \text{\AA}$  (Equation 2). As the radius of gyration ( $R_g$ ) of a mAb is approximately  $50 \text{\AA}$  and mAbs are highly anisotropic, mAbs must orient favorably and interdigitate to pack with the observed separation distance in these solid formulations [74,108]. However,

comparison to SANS measurements of frozen mAb formulations without sugars [51], where  $d = 31 \text{ \AA}$ , indicates that the mAbs are separated by the stabilizers. These measurements show that the presence of sugar in this formulation leads to an increase in the average protein-protein surface separation distance of  $\sim 11 \text{ \AA}$ , which is comparable to the molecular size of trehalose  $\sim 9 \text{ \AA}$  [109]. Thus, our measurement confirms the assumption of the sugar forming a protective adsorbed layer surrounding the protein in these solid formulations.

Although the use of deuterated sucrose in the formulation clearly increases contrast sufficiently to show structural features of the protein in the sugar matrix, it does not alter the power-law scattering in the low- $q$  regime. Consequently, there are no significant microstructural features in the corresponding range of 300 to 1600  $\text{\AA}$ , such as distinct protein-rich clusters or other microheterogeneities. The longest length scales probed by SANS are comparable to the limit of resolution of the confocal fluorescence microscopy imaging performed previously for similar formulations (Chapter 3) [77], which is approximately 1500  $\text{\AA}$  or 0.15  $\mu\text{m}$ . Hence, we conclude that mAbs in these lyophilized formulations are distributed uniformly on length scales from that of the protein to that of the particle, and that there are no microheterogeneities or evidence of any significant population of aggregated protein. Still, it is possible that there are larger areas of protein-rich or protein-free domains within the solid formulations, as long as they are randomly distributed, for example in a fractal manner.

### **4.3.2 Microstructural Changes under Cyclic Humidification**

These results show that SANS is a promising method to study the microstructure of therapeutic proteins in a variety of formulations with different

process conditions, compositions, and protein stability. However, the use of deuterated excipients requires modifications to the standard formulations, and may lead to changes in protein-excipient interactions. Another way to introduce contrast in solid-state formulations is by introducing D<sub>2</sub>O into the formulation through uptake from the vapor phase. The D<sub>2</sub>O will diffuse through the hygroscopic powder, mainly in the sugar phase, and increase the SLD contrast. In addition, it will lead to deuterium exchange with exchangeable hydrogens on both the protein and sugar, which will occur as a function of time and exposure. For example, hydrogens in the core of the protein will not exchange as rapidly as those readily accessible on the sugar molecules, an effect that has recently been exploited to study protein formulation stability [102–104,110]. In the following, we exploit this method to further study the protein-excipient distribution in these solid-state formulations.

The advantage of using the vapor cell in this manner is twofold. First, the uptake of D<sub>2</sub>O within the sample greatly enhances the contrast, allowing the observation of the microstructure, *i.e.*, the protein-protein interaction peak, in typical solid-state samples without the use of deuterated sugar. Second, the vapor cell allows *in situ* characterization of microstructural changes under stressed environmental conditions such as heat or water uptake. Formulations in the vapor cell were initially exposed to pure nitrogen flow for a period of about one hour to assure the removal of excess water. Subsequently, formulations were exposed to cycles of alternating nitrogen and water vapor flow, while their microstructural changes were monitored using SANS.

The evolution of the SANS patterns with time for the deuterated sucrose formulation (F2) for three successive water vapor – nitrogen cycles is shown in Figure

4.4. As the use of deuterated sugar provides sufficient contrast to distinguish the nearest-neighbor peak, the effects of moisture uptake and contrast changes due to the introduction of deuterium can be decoupled. Specifically, H<sub>2</sub>O vapor can be used to investigate the effect of humidity and moisture uptake on the formulation, while D<sub>2</sub>O vapor can be used to investigate the changes in contrast. In general, exposure to water leads to distinct changes in the scattering patterns over time that can be characterized by three main metrics: the peak height, the peak position, and the background scattering (Figure 4.3b). Changes in peak height can be attributed to the number of available scattering objects (protein molecules) and the contrast between the protein and excipient components. Changes in peak position can be attributed to changes in the inter-protein distance or protein distribution. Lastly, changes in background scattering can be attributed to the amount of hydrogen present in the formulation, and hence the uptake of hydrogenated water.

The evolution of these three structural metrics throughout the progress of the vapor cell experiment is shown in Figure 4.5a-c. The exposure to H<sub>2</sub>O is expected to lead to an increase in the background scattering as additional water is taken up by the hygroscopic powder. In addition, uptake of H<sub>2</sub>O is expected to decrease the contrast in the sample if H<sub>2</sub>O distributes throughout the sugar phase. This can be understood from Figure 4.1, where, in the case of 0% deuterium exchange, mixing of water (SLD below that of the protein) with the deuterated sugar (SLD above that of the protein) will effectively reduce the SLD of the sugar component and decrease the SLD difference between the sugar and protein. Indeed, Figure 4.4a and Figure 4.5a and c show that the peak height decreases and the background increases with H<sub>2</sub>O uptake over a period of 10 h. Subsequent drying of the samples with N<sub>2</sub> reverses this effect.

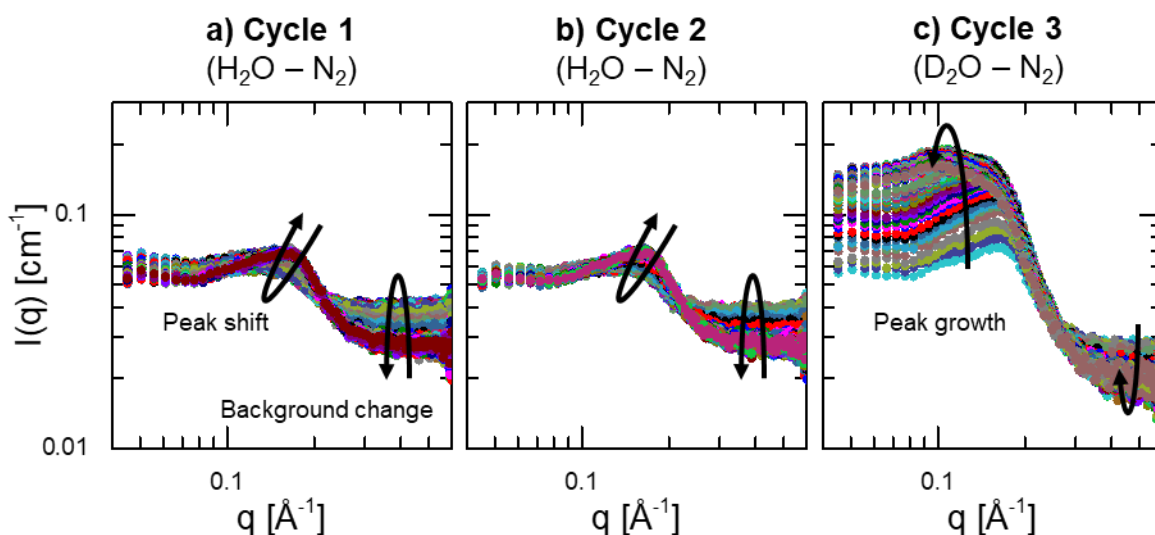


Figure 4.4: Evolution of the SANS pattern of lyophilized mAb1 in deuterated sucrose (F2) as a function of time under cycles of alternating nitrogen and water vapor flows. The arrows on the scattering patterns indicate the general trend of the scattering pattern with time. A video of the evolution of the SANS pattern with time can be found online [100].

The uptake of H<sub>2</sub>O also has a significant effect on the peak position, and hence on the average protein-protein distance within the formulation. Upon the introduction of water, the nearest-neighbor peak gradually moves to smaller  $q$ -values, corresponding to an increase in the average inter-protein distance (Figure 4.4a). Thus, the sample swells upon humidification at the level of interprotein separation. Upon subsequent drying with nitrogen, this distance is observed to recover, but it recovers to an average separation distance slightly smaller than in the original formulation. The corresponding scattering patterns at the two distinct peak positions are shown in Figure 4.6a-b, with approximate peak positions and average protein-protein distances listed in Table 4.2. This shows that the drying rate and conditions, *i.e.* processing, influence the formulation at the nanometer scale.

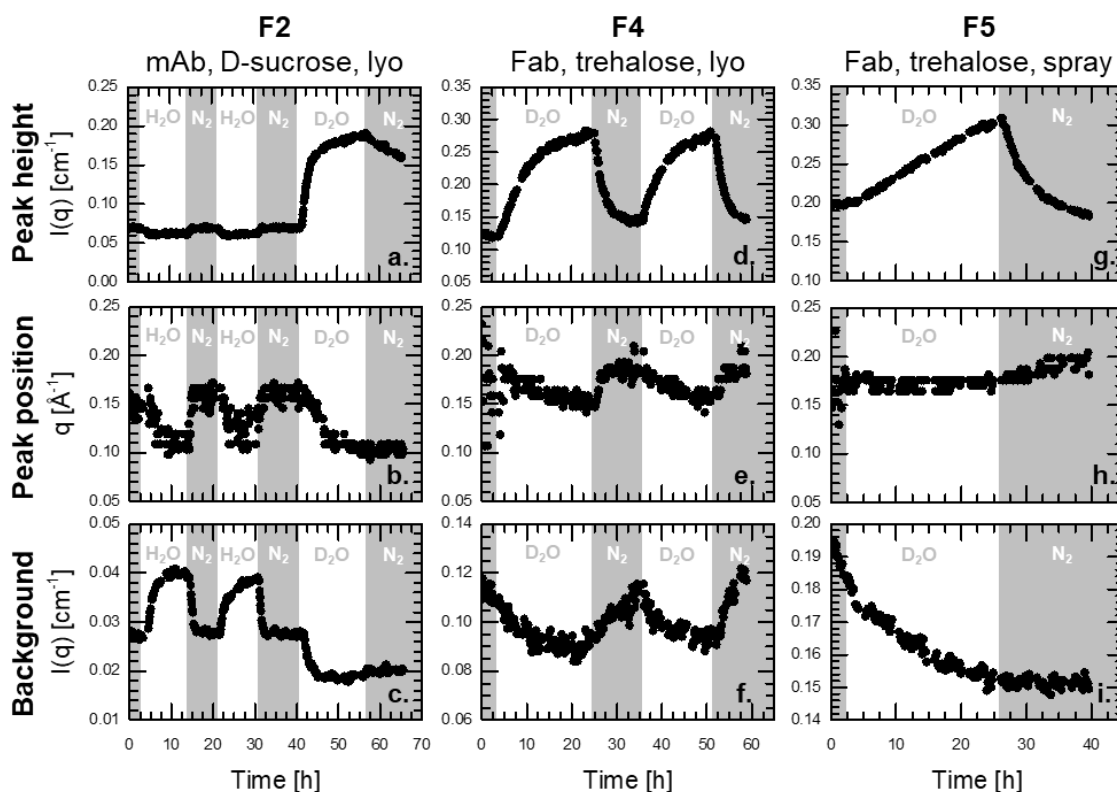


Figure 4.5: Evolution of prominent scattering features of three formulations as a function of time under cycles of alternating nitrogen and water vapor flows.

The uptake of water in solid-state formulations is known to decrease the glass transition temperature ( $T_g$ ) [101]. Here, the formulations were subjected to very high humidity levels, which plasticized the sugar-protein matrix. Indeed, the formulation powders were visibly collapsed after the vapor cell experiment, leading to densification of the powder. Regardless, regular full scans of the scattering patterns throughout the course of the vapor cell experiment show the same scattering from larger particles at low  $q$  values, indicating that the powders retained their solid morphology (data included in Appendix C). However, as shown, water uptake led to

sufficient plasticization to ‘swell’ the matrix between protein molecules, while drying led to an average separation distance that is slightly smaller than in the original formulation (bottom panels of Figure 4.6a and b). The fact that the peak shifted gradually over several hours suggests that these microstructural changes occurred throughout the whole sample volume to approximately the same degree. Importantly, repeating this H<sub>2</sub>O-N<sub>2</sub> cycle led to identical changes in the scattering patterns, indicating that the process is reversible (Figure 4.4b and Figure 4.5a-c).

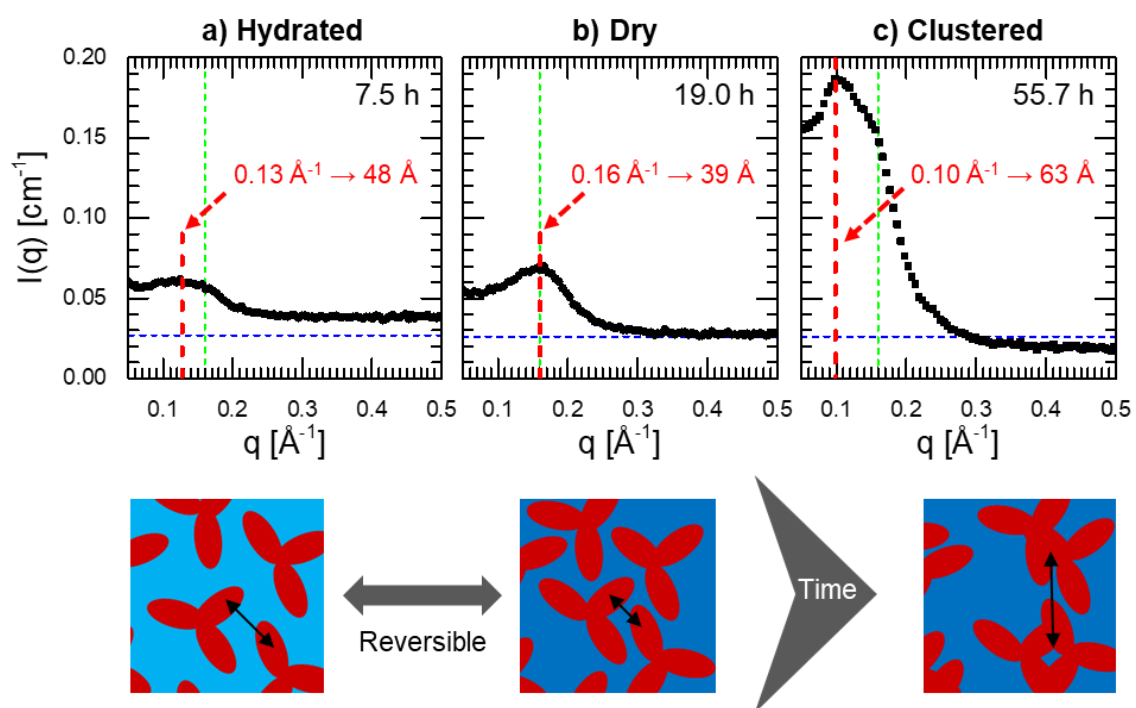


Figure 4.6: Overview of observed peak positions of lyophilized mAb in deuterated sugar (F2) with schematics of the corresponding hypothesized microstructures. The green line indicates the original peak position, while the blue line indicates the original background value.

Table 4.2: Overview of SANS peak positions for mAb and Fab formulations. The characteristic distance is estimated from the  $q$ -value using Bragg's law (Equation 2.4).

	F2: Lyophilized mAb1	F4: Lyophilized Fab1	F5: Spray-dried Fab1
Initial peak	0.15 Å <sup>-1</sup> 42 Å	0.17 Å <sup>-1</sup> 37 Å	0.17 Å <sup>-1</sup> 37 Å
Hydrated peak	0.13 Å <sup>-1</sup> 48 Å	0.16 Å <sup>-1</sup> 39 Å	0.17 Å <sup>-1</sup> 37 Å
Dry peak	0.16 Å <sup>-1</sup> 39 Å	0.18 Å <sup>-1</sup> 35 Å	0.19 Å <sup>-1</sup> 33 Å
Cluster peak	0.10 Å <sup>-1</sup> 63 Å	/	/

Using D<sub>2</sub>O instead of H<sub>2</sub>O vapor is expected to lead to similar morphological changes, but with a significant change in the scattering intensity due to the increase in contrast. Moreover, the background scattering is expected to decrease as hydrogen is removed from the system due to deuterium exchange. This is indeed observed, where upon D<sub>2</sub>O uptake the peak height increased substantially while the background scattering decreased (4.4c). Initially, the peak position moved to smaller  $q$  values just as during H<sub>2</sub>O uptake. However, after a few hours of exposure, a separate, second peak emerged at even smaller  $q$  values (4.5a-c).

This second peak is hypothesized to be the result of scattering from protein clusters or (reversible) aggregates in the formulation. Hence the position of this cluster peak represents the average distance between protein clusters or a protein cluster and a monomer, and not individual molecules (Figure 4.6c, bottom). There are several factors that support this hypothesis. First, the fact that the second peak emerges independently of the first peak, and does not involve a shift of the first peak, indicates that the peak is caused by a distinct fraction of protein molecules in the formulation,

which grows over time, and not a general change in the protein microstructure as seen during water uptake and release. Second, the rapid growth of the second peak, without a similar decrease in the first peak, supports the viewpoint that the protein indeed forms correlated clusters. This idea is based on neutron scattering theory, which shows that, neglecting changes to particle structure and interactions, the total scattering intensity increases twofold if two smaller particles merge [46]. Third, the position of the peak, which at  $0.10 \text{ \AA}^{-1}$  corresponds to an average separation distance of  $63 \text{ \AA}$ , is consistent with the radius of gyration of a mAb dimer, assuming that the dimers interdigitate similarly to the mAb monomers. The radius of gyration of mAb dimers in concentrated solutions has been measured by SANS as  $69 \text{ \AA}$  [108].

Interestingly, some mAbs have been shown to form reversible dimers in solution that coexist with the dispersed monomers, even at relatively low concentrations [108]. In the solid state, the formation of such dimers could occur as a function of time in the plasticized state, or could be triggered specifically due to the presence of  $D_2O$ , which can alter interactions among protein, water, and excipients. In either case, these findings show that such dimers form even in the solid state when sufficient mobility of the mAb is possible due to plasticization of the matrix.

### **4.3.3 Comparison between mAbs and Fabs**

The VC-SANS patterns of a lyophilized formulation containing a Fab and regular, non-deuterated sugar (Formulation F4) were used to assess whether the increase in scattering contrast due to  $D_2O$  exposure is sufficient to reveal the protein microstructure in such non-deuterated formulations, as well as to characterize potential differences between the microstructures of mAbs and Fabs. The evolution of key metrics of the SANS patterns of Formulation F4 is shown in Figure 4.5d-f, and a video

of the evolution of the patterns with time can be found online [100]. Initially, the patterns of this non-deuterated formulation are similar to that of Formulation 1 in Figure 4.3, with no indication of the nearest-neighbor peak. However, exposure to D<sub>2</sub>O vapor increases the contrast sufficiently to reveal a single scattering peak. Consequently, VC-SANS is a promising technique to investigate the protein-scale microstructure of pristine biopharmaceutical formulations.

The exposure to water vapor can modify the microstructure, as evidenced by the changes in peak position and visible densification of the powder, which can compromise the ability of VC-SANS to reveal the true, native particle microstructure. However, the plasticization of the matrix is primarily the result of the high relative humidity in the vapor cell. Previous work on hydrogen-deuterium exchange in solid-state biopharmaceutical formulations (ssHDX) has shown that a lower relative humidity, below approximately 11%, can lead to deuterium exchange while keeping the powder density intact [102]. While we did not pursue such low levels of humidification here, continued studies along the lines of those presented here but at low relative humidity could aid in investigating the native microstructure of non-deuterated biopharmaceutical formulations.

While the nearest-neighbor peak of the lyophilized Fab formulation follows similar trends to those of the mAb formulation during water uptake and release, the peak positions naturally correspond to smaller protein-protein distances (Table 4.2), consistent with the smaller size of Fabs ( $R_g$  of 28 Å). Moreover, unlike the packing in the highly anisotropic mAbs, the globular Fabs do not interdigitate and the Fab  $R_g$  is smaller than the average protein-protein distance in all cases, which corresponds to the behavior of globular proteins more generally [74]. Although this Fab1 has a similar

microstructure to the Fab of mAb1, a second peak does not appear in the scattering patterns and so we can conclude that they do not form dimers or other aggregates within the time scale of the experiment.

#### **4.3.4 Comparison between Lyophilization and Spray-Drying**

Lyophilization and spray-drying are vastly different drying processes, which lead to very different particle morphologies as well as differences in protein-excipient microheterogeneity on the particle scale (Chapter 3) [77]. For example, certain spray-dried formulations show an increase in protein concentration towards the exterior of the particles, while proteins in lyophilized formulations are generally homogeneously distributed on the particle scale (Figure 3.2). To investigate the effects of the drying method on the protein-scale microstructure, the VC-SANS patterns of a lyophilized (Formulation F4) and a spray-dried (Formulation F5) Fab formulation in a non-deuterated sugar are compared, where both have the same nominal sugar-to-protein ratio of 1.

Despite the different drying mechanisms, the protein-scale microstructure of lyophilized and spray-dried formulations is similar, as shown by the evolution of key metrics of the SANS patterns of Formulation F4 and F5 in Figure 4.5d-i. While the average protein-protein distance is slightly smaller in the spray-dried formulation (Table 4.2), overall trends in the scattering patterns are maintained. In a solid-state formulation containing microheterogeneity, with certain areas enriched in protein and others depleted, it is expected that the local, average protein-protein distance will be smaller than for the situation where the same amount of protein is homogeneously distributed. Hence, the smaller average protein-protein distance in the spray-dried formulation is consistent with the particle-scale microheterogeneity observed in CFM

(Figure 3.2). Moreover, the full  $q$ -range SANS patterns (included in Appendix C) show that this microheterogeneity in the spray-dried formulation does not originate from major changes in protein-scale microstructure, but rather can occur by a redistribution of the excipient and the protein molecules.

This observation raises a question about how the microstructure is affected when insufficient sugar is present to stabilize the protein, either throughout the whole formulation or locally due to microheterogeneity. Below a certain sugar-to-protein ratio, which depends on the specific sugar, protein, and overall formulation conditions, formulations can exhibit a loss of protein stability [101]. As all of the formulations in this study were initially stable, with sugar-to-protein ratios of 1, it is expected that adequate sugar was present and that the effects of low sugar-to-protein ratios were not probed with these formulations. However, the methodology developed here can be applied to study such formulations with low sugar-to-protein ratios, as well as other solid-state formulations.

#### **4.3.5 Relation between Microstructural Changes and Aggregation**

The VC-SANS results can be used to assess the effects of the protein-scale microstructural changes in the solid-state formulations on the aggregation behavior and stability of the protein. As SANS probes the ensemble microstructure over the whole sample volume, it is better suited to studying the mechanisms and structure of bulk aggregation events than to detecting small degrees of protein aggregation. While this study focuses on initially stable formulations, where aggregate formation over the lifetime of the formulation is expected to be limited, interesting aspects of the aggregation mechanisms are revealed by observation of the microstructural changes in stressed conditions, such as through exposure to humidity and high temperature.

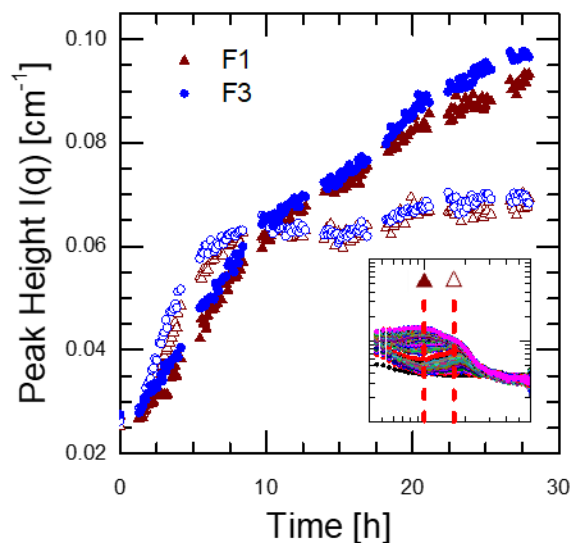


Figure 4.7: Comparison of peak height evolution during exposure to vapor cell  $D_2O$  flow for a regular (F1) and a heat-stressed lyophilized mAb sample (F3). The open symbols show the height of the monomer peak ( $q = 0.16 \text{ \AA}^{-1}$ ), while the filled symbols show the height of the cluster peak ( $q = 0.10 \text{ \AA}^{-1}$ ). These peak positions are indicated in the inset, which shows the evolution of the SANS patterns of Formulation F1 with time (compare to Figure 4.4).

The evolution of the nearest-neighbor peak height in the VC-SANS patterns of both an unstressed (F1) and a heat-stressed (F3) formulation under  $D_2O$  flow is included in Figure 4.7. To obtain the heat-stressed sample (F3), the regular lyophilized mAb formulation (F1) was held at  $110 \text{ }^\circ\text{C}$  for 5 hours to generate about 15% aggregates after reconstitution, compared to about 6% aggregates in the regular formulation (Table 4.1), as detected by size-exclusion chromatography (SEC). Figure 4.7 is similar to that for the mAb in the deuterated sugar (F2, Figure 4.5a), but records the peak heights of the monomer (open symbols, at  $q = 0.16 \text{ \AA}^{-1}$ ) and cluster (filled symbols, at  $q = 0.10 \text{ \AA}^{-1}$ ) peaks separately. Peak heights are scaled by the heights of

the monomer peaks of the two formulations to account for small differences in sample mass. Note that the peak positions correspond to those observed for F2 (Table 4.2) and that the cluster peak overtakes the monomer peak about 10 hours after the start of the D<sub>2</sub>O-rich vapor flow, indicating the presence of aggregates in both formulations after exposure to humidity.

If the aggregates detected by SEC were already present in the solid-state formulation before reconstitution, the cluster peak would be present in the VC-SANS patterns from the onset of the experiment or at least at short time scales. However, the fact that the cluster peak does not appear at the onset, especially for the heat-stressed formulation, and the fact that the peak heights align at early times for both formulations, shows that the irreversible aggregates detected by SEC are not present initially in the solid-state formulation. Specifically, the fact that the two formulations have the same peak heights even though they have significantly different aggregate content after reconstitution indicates that the formation of these reversible aggregates in the solid state is not directly related to the formulation's tendency to form aggregates in solution. However, the small increase in peak height of the stressed formulation as compared to the unstressed formulation towards the end of D<sub>2</sub>O exposure could reflect its higher tendency to aggregate. These observations suggest that while modifications to the protein that make it prone to aggregation, such as partial unfolding or chemical modification, occur in the solid state, the proteins in stressed formulations are not aggregated in the solid state, where diffusion is quenched, but rather aggregate only after reconstitution.

If the formation of the clusters observed by VC-SANS is not directly linked to the aggregates detected by SEC, what is the nature of these clusters in the solid state?

If the aggregates detected by VC-SANS are irreversible, which would indicate a permanent loss of stability, they are expected to persist through reconstitution and also be detected by SEC. However, if SEC does not detect the aggregates formed during VC-SANS, they are reversible and presumably disassociate during the reconstitution process. Since the aggregate content of the reconstituted formulations before and after VC-SANS is the same (Figure 4.8), most clusters detected by VC-SANS appear to be reversibly self-associating aggregates (reversible clusters). The fact that both formulations have the same peak height indicates that such aggregates are reversible. Although these aggregates disassociate upon reconstitution within a period of days after the VC-SANS experiment, their behavior when kept in the solid state over a longer span of time is an interesting topic for future study. For example, one could hypothesize that these reversible aggregates are precursors for irreversible aggregation during long-term storage, and that formulations that exhibit such reversible aggregates after drying, *e.g.*, due to low excipient concentrations, are more prone to long-term stability issues.

While these results demonstrate that VC-SANS is a useful tool for understanding protein-scale microstructural changes in solid-state formulations, it remains challenging to determine a formulation's long-term stability. However, recent reports have shown that measurements of molecular dynamics in these formulations are capable of predicting stability. For example, both solid-state hydrogen-deuterium exchange with mass spectrometry (ssHDX-MS) and neutron backscattering (NB), techniques that probe different but potentially related fast protein dynamics, have been shown to reveal characteristics that correlate with long-term stability measurements [22,102–106]. However, the fundamental mechanisms of why these characteristics are

good predictors are not yet fully understood. As VC-SANS combines aspects of both ssHDX-MS and NB by combining hydrogen-deuterium exchange with protein-scale characterization, it is a promising technique to help elucidate the basis for the correlations between long-term formulation stability and molecular dynamics.

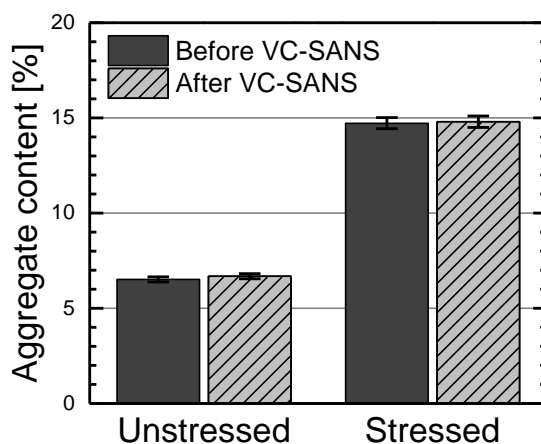


Figure 4.8: Comparison of aggregate content before and after exposure to vapor cell conditions for a regular (F1) and heat-stressed lyophilized mAb sample (F3), as measured by size-exclusion chromatography after reconstitution of the solid-state powders.

#### 4.4 Conclusions

VC-SANS with contrast variation is shown as a new method for characterizing changes to the molecular arrangement *in situ* on protein length scales in solid-state biopharmaceutical formulations. Investigation of lyophilized and spray-dried formulations shows crowded morphologies similar to those in frozen protein solutions, in which protein molecules are separated sufficiently to be stabilized by a protective sugar layer, independent of the drying method. Plasticization of the solid matrix

through exposure to humidity leads to the formation of reversibly self-associated aggregates, possibly in the form of protein dimers, which dissociate after reconstitution. In addition, heat-stressed formulations do not show an increase in protein clustering in the solid state as compared to unstressed formulations, although the aggregate content of heat-stressed formulations after reconstitution is significantly higher. These results suggest that irreversible protein aggregation occurs upon reconstitution of the solid-state formulations, but that the formation of these aggregates is not directly caused by the presence of reversible aggregates in the solid state.

## Chapter 5

### DATA-DRIVEN DEVELOPMENT OF PREDICTIVE MODELS FOR SUSTAINED DRUG RELEASE

“Alle Dinge sind Gift, und nichts ist ohne Gift, allein die Dosis macht  
dass ein Ding kein Gift ist.”

Paracelsus – *Septem Defensiones* (1538)

Solid-state biopharmaceutical formulations are often used in alternative drug delivery pathways such as pulmonary delivery or sustained drug delivery devices, which can increase the efficacy of the drug and patient compliance. This chapter describes a new methodology for parameter estimation of predictive mathematical models for such sustained drug delivery systems. The next chapter will use this methodology to make model predictions for a couple of experimental model systems.

#### 5.1 Introduction

The potential of sustained drug-delivery systems to enhance the long-term bioavailability of pharmaceuticals has motivated their application for biopharmaceutical formulations, where they can improve efficacy and reduce tissue damage due to frequent subcutaneous injections or intravenous infusions, ultimately improving patient compliance [7,111,112]. However, their inherent extended release times complicate their design and can delay and increase the cost of development, due to the need for multiple long-term experimental studies. The use of mathematical

models to simulate these drug-delivery systems and predict the expected behavior *in vitro* or *in vivo* for a wide range of system parameters can guide design and significantly reduce the required number of experimental trials. While the main advantage of these predictive models lies in their capability to make predictions outside of the known, experimentally-verified system behavior, making such predictions is intrinsically challenging and requires that the model can perform accurately when the parameter space is extended.

Accurate model predictions can be guaranteed if the model correctly describes the fundamental mechanisms behind the physical processes involved. However, because of the complexity of drug-delivery systems, the relevant underlying mechanisms are not always fully understood, especially for *in vivo* release. For example, drug release from poly(lactic-co-glycolic acid)-based (PLGA) drug delivery systems involves more than a dozen physico-chemical processes with more than 40 interactions among these processes, all affecting drug release [113]. Consequently, mechanistic models that faithfully capture the drug-delivery processes will necessarily be complicated and contain a large parameter set that is subject to overfitting of available data. Alternatively, models can be simplified by abstracting certain processes or by using empirical correlations to capture experimental data. Such empirical models are computationally more tractable and have a limited set of parameters that are often specifically chosen because they can be determined from experimental data, but the performance of these models outside of the conventional parameter space is suspect at best. To balance these issues, predictive models typically contain simplified mechanistic representations or combine both empirical and mechanistic components. Thus, the challenge in developing predictive models lies in balancing empiricism for

simplicity with rigorous, but more complex representation of fundamental processes, which again is subject to overfitting of available data.

A model's performance is often based purely on its capacity to predict specific test data sets from parameter values estimated from a training data set [114–117]. However, it is important to understand which parameters in a given model are critical, as well as how many parameters can be estimated unambiguously from the available experimental data or, conversely, how many and which experimental data are necessary to support model training. Consequently, model selection, confidence, and design can be greatly improved by quantitative measures of the quality of parameter estimation.

Here we provide a practical approach to obtain quantitative information on model and parameter quality and performance, with the goal of stimulating rational decision-making in the design and implementation of predictive models. We demonstrate the methodology through a model for sustained drug release from PLGA, one of the most commonly used biodegradable polymers for sustained drug release [111]. A wide variety of different PLGA-based drug delivery systems have been developed, including microspheres, gels, rods, and solvent depots. The complexity of the interconnected PLGA degradation, erosion, and drug release in these systems has made predictions of drug release challenging [113,118,119]. Consequently, a broad spectrum of models are available in the literature with varying levels of complexity and empiricism [117]. Our goal here is not to develop a new model but rather to illustrate a new methodology that can help select the best model for a specific application, as well as aid in the development of new models, by using published models and experimental data.

The methodology is based on the results of a recently-developed optimization algorithm [120] that, due to its stochastic nature, generates meta-data concerning the optimal fit parameters and their error estimates. These meta-data are further analyzed using statistical methods to determine factors related to model confidence and parameter sensitivity, accuracy, and correlation. While we focus on the predictive modeling of sustained drug release from PLGA systems, the approach is readily applied to a broad range of drug delivery modeling.

## **5.2 Methodology**

### **5.2.1 Mathematical Model**

A model of controlled release was adapted from Little *et al.* for which the rationale and details regarding the model design as well as comparisons between model predictions and experimental data have been presented [121–123]. This model was specifically chosen because it was developed for predicting drug release from biodegradable polymer systems, particularly PLGA. To achieve this, the model combines both empirical and mechanistic elements to capture the release processes sufficiently accurately while limiting the number of model parameters. Several model extensions have been proposed that can include additional processes such as dissolution effects and those relevant for *in vivo* release [122,123]. Here we have adopted a relatively simple version of the model to use as an illustrative case study. This version, described briefly below, can capture zeroth- and first-order release profiles, as well as the characteristic tri-phasic, sigmoidal release profile consisting of first-phase “burst” release, a lag phase, and second-phase release.

The model incorporates three fundamental mechanisms implicated in drug release from biodegradable polymers in the form of partial differential equations (PDEs): drug diffusion, characterized by the diffusivity  $D_D$ , water uptake, characterized by the local water concentration  $C_{H_2O}$ , and polymer degradation, characterized by the average molecular weight  $MW$ :

$$\frac{\partial C_D}{\partial t} = \frac{1}{r^m} \frac{\partial}{\partial r} \left( r^m \frac{\partial}{\partial r} D_D C_D \right), \quad (5.1)$$

$$\frac{\partial C_{H_2O}}{\partial t} = \frac{1}{r^m} \frac{\partial}{\partial r} \left( r^m \frac{\partial}{\partial r} D_{H_2O} C_{H_2O} \right) - k_{deg} MW C_{H_2O}, \text{ and} \quad (5.2)$$

$$\frac{\partial MW}{\partial t} = -k_{deg} MW C_{H_2O}. \quad (5.3)$$

In these equations,  $m$  is a parameter that defines the geometry of the system (0 for a slab, 1 for a cylinder, and 2 for a sphere),  $t$  is the time, and  $r$  is the spatial coordinate in the simplified one-dimensional geometry, which follows from the assumption of symmetry. Other parameters are listed in Table 5.1. Drug diffusion out of the system and water uptake are described by Fick's second law. As water diffuses into the system, it reacts in a second-order hydrolysis reaction with the biodegradable polymer, which decreases the polymer's average molecular weight (MW). Note that the MW in the model can be either the weight-averaged or number-averaged MW.

Diffusion and erosion of the low-MW polymer degradation products are not explicitly described. Instead, the porosity ( $\epsilon$ ) of the system depends on the MW of the polymer through an empirical, sigmoidal relationship in which porosity rapidly increases when the average polymer MW has decreased sufficiently to reach a specific MW at which release occurs ( $MW_r$ ):

$$\epsilon(MW(r, t)) = 1 - \frac{1}{2} \left[ 1 + \operatorname{erf} \left( \frac{MW(r, t) - MW_r}{\sqrt{2\sigma_r^2}} \right) \right]. \quad (5.4)$$

Here erf is the error function and  $\sigma$  represents the standard deviation (SD) of the polymer MW at the moment of release. As the polymer molecular weight decreases and the porosity increases, the effective diffusivity of the drug encapsulated within the matrix ( $D_D$ ) increases, asymptotically approaching the maximum diffusivity of the drug within the system ( $D_{D,0}$ ). However, drug within a certain occlusion radius ( $R_{occ}$ ) of the outer surface of the system is assumed to be directly accessible by infiltrating water and experiences unhindered diffusion at the maximum diffusivity, representing the first-phase burst release:

$$D_D(r, t) = \begin{cases} D_{D,0} & \text{if } r > (R - R_{occ}) \\ D_{D,0} \epsilon(MW(r, t)) & \text{if } r \leq (R - R_{occ}) \end{cases}. \quad (5.5)$$

The initial conditions specify the initial drug and water concentration and initial polymer MW ( $MW_0$ ) in the system:

$$C_D(r, 0) = C_{D,0}, \quad (5.6)$$

$$C_{H_2O}(r, 0) = 0, \text{ and} \quad (5.7)$$

$$MW(r, 0) = MW_0. \quad (5.8)$$

while the boundary conditions are defined based on symmetry conditions at the system center and perfect sink conditions at the surface:

$$\frac{\partial C_D}{\partial r}(0, t) = 0, \quad (5.9)$$

$$\frac{\partial C_{H_2O}}{\partial r}(0, t) = 0, \quad (5.10)$$

$$C_D(R, t) = 0, \text{ and} \quad (5.11)$$

$$C_{H_2O}(R, t) = C_{H_2O,0}. \quad (5.12)$$

Table 5.1: Mathematical model parameters and initial fitting values for the microsphere data set. Parameters in grey are held constant during fitting of the parallel tempering algorithm (PTA).

	Parameter	Symbol	Initial Value	Units
1.	Maximum drug diffusivity	$D_{D,0}$	$7.27 \times 10^{-17}$	$[\text{m}^2/\text{s}]$
2.	Initial drug concentration	$C_{D,0}$	117	$[\text{kg}/\text{m}^3]$
3.	Water diffusivity	$D_{H_2O}$	$10^{-12}$	$[\text{m}^2/\text{s}]$
4.	Maximum water concentration	$C_{H_2O,0}$	50	$[\text{mass}\%]$
5.	Drug occlusion size (radius)	$R_{occ}$	1	$[\mu\text{m}]$
6.	System size (radius)	$R$	13.15	$[\mu\text{m}]$
7.	Polymer initial molecular weight	$MW_0$	7831	[Da]
8.	Polymer molecular weight at drug release	$MW_r$	1000	[Da]
9.	Polymer molecular weight degradation rate constant	$k_{deg}$	$6.00 \times 10^{-10}$	$[\text{1}/\text{s}(\text{kg}/\text{m}^3)]$
10.	Polymer molecular weight standard deviation at release	$\sigma_r$	1000	[Da]

### **5.2.2 Experimental Data**

Two experimental data sets from the literature served as example problem sets. One data set, describing the release of lysozyme from PLGA microspheres in an acetate buffer [124], is limited in that it contains only drug release data. These data show a sigmoidal release profile accompanied by an initial burst release. Conversely, the second data set, involving the release of fragment antibodies (Fabs) from PLGA solvent depots, contains data on drug release, polymer degradation, polymer erosion, and water uptake [91]. Moreover, it contains data for three different initial polymer MWs (10, 41, and 56 kDa), enabling a more thorough exploration of model behavior.

### **5.2.3 Parallel Tempering Algorithm**

The adaptive parallel tempering algorithm (PTA) [120] was used to determine the optimal model parameters based on the available experimental data. The design and attributes of the algorithm, as well as its superior performance when evaluating several standard test problems, are discussed in the literature [120]. The PTA is particularly effective at robustly and efficiently finding estimates for global optima for complex problems, and the method generates meta-data that enable evaluation of the model.

Conceptually, the objective function that describes the goodness-of-fit between a model and experimental data can be imagined to constitute a landscape within parameter space, where minima in the landscape correspond to parameter solutions that describe the experimental data well. The PTA is a stochastic method that identifies parameter sets that minimize an objective function by directing a biased “random” walk through the allowed parameter space. This biased random walk is generated similarly to the more familiar Monte Carlo stochastic simulations in

statistical physics, where the objective function here plays the role of microstate energy and the parameter space that of the physical microstate space. Due to the stochastic nature of the PTA, multiple runs of the algorithm will lead to different optimal parameter solutions. Comparing solutions can identify if, for example, the solution landscape includes multiple basins of comparable fit quality, or the relative breadth of the solution basin. Consequently, the PTA can be used to explore the objective function landscape and understand parameter set uniqueness and uncertainty.

While assessment of the objective function landscape can be achieved by evaluating the objective function for each parameter combination, for complex problems this is often impractical due to the high computational requirements. Instead, the PTA focuses, due to its design, on the regions of parameter space where the effects of parameter sensitivity and correlation are most critical. Within one run, the PTA evaluates the objective function many times, generally guided towards the minima. Hence, even within one run, the PTA generates a large amount of meta-data that can be used to understand critical aspects of the objective function through statistical analysis, without having to evaluate it for the whole parameter space. When the PTA is run multiple times, additional meta-data on the objective function landscape around the *global* minimum can be obtained.

#### **5.2.4 Implementation**

The PTA and the mathematical model were coded in Matlab<sup>®</sup> (Mathworks, R2017b). The objective function used by the PTA to optimize the model parameters was based on a sum-squared error (SSE) between the model results and experimental data sets. In the case of multiple data sets, such as the solvent depot data, the SSE was weighted equally for each data set, though changing the weighting factors did not have

a significant effect on the optimization results. The set of model partial differential equations was solved using the finite-difference method through the *pdepe* function in Matlab<sup>®</sup>. Default values for the PTA-specific parameters were used [120].

Initial values of the model parameters, the starting point of the PTA, were based on literature values. Initial parameter values for the microsphere data fitting are included in Table 5.1. For the more comprehensive solvent depot data, the PTA solutions were shown to be fairly insensitive to the initial parameter values (data not included). The initial drug concentration, maximum water uptake, and microsphere radius were considered known and were held constant during model fitting, reducing the number of parameters that were initially fitted to seven. The initial drug concentration was estimated from common values in the literature. However, the initial drug concentration does not affect the shape of the cumulative drug release curve; it determines only the absolute amount of drug released per period of time. The maximum water uptake is also mostly a scaling factor, and was estimated to be roughly 50% by system mass, based on water uptake data in PLGA systems [91,125]. The mean system diameters and the PLGA initial MWs were reported by the authors [91,124]. The polymer MW variance at release was estimated based on the reported polymer polydispersity indices (PDIs) of approximately 2 [91,124]. The polymer degradation rate was estimated based on reported PLGA degradation half-lives of approximately 3 weeks for a 50:50 L/G ratio [126,127]. The occlusion radius was estimated based on the expected particle size of the encapsulated drug [91]. The initial values for the maximum drug diffusivity, water diffusivity, and polymer MW at release were based on empirical correlations [121,122].

Meta-data on the parameters were obtained by multiple runs using the same initial values and these sets of parameter solutions were used for statistical analysis, including parameter variation and Pearson correlation coefficients (*corrcoef* function in Matlab<sup>®</sup> [128]). The correlation coefficients yield probability values (p-values) for the hypothesis that there are no correlations among different parameters. A p-value smaller than 0.05 was considered a significant parameter correlation.

### 5.3 Results and Discussion

The combined mathematical model and PTA were first used to analyze the limited microsphere data set and then to analyze the more extensive solvent depot data set for the 41 kDa MW PLGA. These optimal model parameters were used to make predictions regarding the 10 and 56 kDa MW PLGA solvent depot data, which are compared against the experimental data.

#### 5.3.1 Detecting Overfitting

Drug release data of lysozyme-loaded PLGA microspheres are shown in Figure 5.1 [124]. The drug release model, adapted from Little *et al.* [121–123], was used in conjunction with the parallel tempering algorithm (PTA) [120] to find optimal parameter solutions. The initial estimates of the model parameters, based on literature values, are included in Table 5.1, with the model prediction for these values shown in Figure 5.1 (dashed line). Without any parameter fitting, the model already describes the experimental data fairly well, which is an asset that this systems-focused model was specifically designed for by its authors.

Results of the PTA fitting are shown in Figure 5.1 (solid line). The optimized parameter set fits the experimental data well and improves on the literature values.

However, fitting such limited data can be suspect as a highly-parametrized model often leads to overfitting of the available data. Meta-data on the fit parameters was obtained from six independent fitting runs from the same initial values. Seven parameters were fit while three were held constant (Table 5.1). The results (Table 5.2) include the optimal parameters for each of the independent runs, the corresponding objective value, and the average parameter values and coefficients of variation (CV) across the six runs. The fits overlap with the fitted curve shown in Figure 5.1 and yield comparable objective values. Although most solutions are located in the same general area of parameter space, there is significant variation in parameter values. In particular, the optimal parameters found in Run 4 are quite different from those identified in the other runs, indicating that the PTA located multiple minima in the objective function.

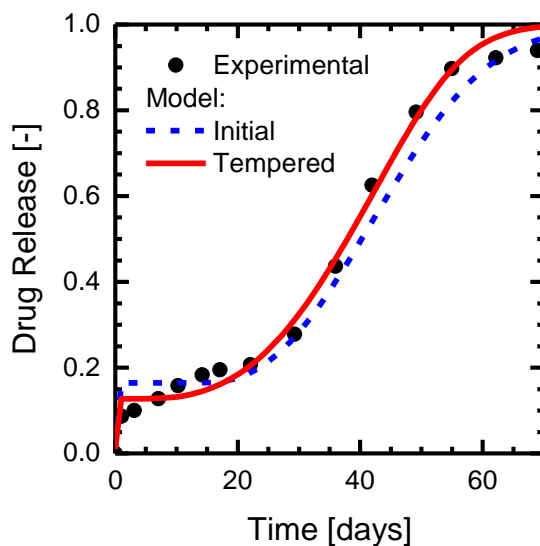


Figure 5.1: Model fitting of the drug release model to experimental, cumulative release data of lysozyme-loaded PLGA microspheres [124].

Table 5.2: Optimal parameter values and corresponding objective functions for the mathematical model fit to the microsphere data set, as obtained from six different runs of the PTA. Red and green highlights indicate the range of the objective function values.

	Drug diffusivity $\left[10^{-16} \frac{\text{m}^2}{\text{s}}\right]$	Water diffusivity $\left[10^{-12} \frac{\text{m}^2}{\text{s}}\right]$	Occlusion radius [ $10^{-6}$ m]	Initial polymer MW [Da]	Polymer MW at release [Da]	Polymer degradation rate constant $\left[\frac{10^{-10}}{\text{s}(\text{kg}/\text{m}^3)}\right]$	Polymer MW SD at release [Da]	Objective Value [-]
Initial	0.73	1.00	1.00	7831	1000	6.00	1000	0.526
Run 1	1.02	0.99	0.96	9784	1101	6.01	1403	0.237
Run 2	0.89	1.21	0.95	8050	1024	6.25	1052	0.240
Run 3	1.19	0.84	0.87	4902	636	5.43	719	0.233
Run 4	2.35	0.09	0.81	6902	1182	3.69	1200	0.223
Run 5	1.26	1.22	0.87	6849	923	5.24	1021	0.232
Run 6	1.53	0.92	0.88	6389	852	4.86	1004	0.231
Average	1.37	0.88	0.89	7146	953	5.25	1067	
CV ( $\sigma/\mu$ )	38%	47%	6%	23%	21%	17%	21%	

Strong parameter correlations are evident in the statistical analysis of these meta-data. Probability values (p-values, Table 5.3) below 0.05 are considered significant (bold values in red in Table 5.3). Many parameter correlations exist in this model fit; this is expected, as the model is highly-parametrized relative to the amount of experimental data. For example, the polymer degradation rate constant and the drug diffusivity parameterize two opposing effects that, when varied in a balanced manner, can lead to similar predictions of drug release behavior. Note that there are especially many correlations among parameters involving the polymer degradation process, which helps identify refinement of the experimental methods. Here, the fitting methodology clearly indicates that additional experimental data are required to

identify parameters uniquely, for example by obtaining additional information on the polymer degradation, such as polymer MW. This is illustrated in the next example.

Table 5.3: P-values for the hypothesis that there is no correlation between the different pairs of model parameters for the microsphere data, based on six PTA runs (Table 5.1). For the bold values in red, the corresponding parameter correlation is considered significant.

P-values (< 0.05)	Drug diffusivity	Water diffusivity	Occlusion radius	Initial polymer MW	Polymer MW at release	Polymer degradation rate constant	Polymer MW SD at release
Drug diffusivity	1.000	<b>0.012</b>	<b>0.029</b>	0.568	0.489	<b>0.000</b>	0.861
Water diffusivity	<b>0.012</b>	1.000	0.118	0.680	0.495	<b>0.032</b>	0.752
Occlusion radius	<b>0.029</b>	0.118	1.000	0.133	0.868	<b>0.008</b>	0.500
Initial polymer MW	0.568	0.680	0.133	1.000	0.090	0.402	<b>0.014</b>
Polymer MW at release	0.489	0.495	0.868	0.090	1.000	0.687	<b>0.033</b>
Polymer degradation rate constant	<b>0.000</b>	<b>0.032</b>	<b>0.008</b>	0.402	0.687	1.000	0.950
Polymer MW SD at release	0.861	0.752	0.500	<b>0.014</b>	<b>0.033</b>	0.950	1.000

### 5.3.2 Critical Parameters and Model Sensitivity

In addition to parameter correlations, estimation of unique parameter values can be compromised when the model results are relatively insensitive to changes in the values of certain parameters. As with correlations, model sensitivity can be inherent to the model itself, but is also influenced by the nature of the available experimental data. Understanding which parameters influence model results, as well as to which parameters the model is insensitive, is important when designing experiments, interpreting the statistical analysis or, at a higher level, developing suitable models. Moreover, keeping non-critical parameters constant through parameter estimation can greatly reduce model complexity and hence computational requirements. Model insensitivities will manifest in the objective function landscape as a shallow trough contained within the specific parameter dimension. Consequently, they can be explored with the PTA similarly to parameter correlations.

The solvent depot data contain information on the polymer MW degradation and water uptake, in addition to the cumulative drug release, for initial polymer MWs of 10, 41, and 56 kDa [91]. The experimental data for the 41 kDa initial polymer MW are shown in Figure 5.2, along with model fits by the PTA from initial values that were estimated from the literature. The model describes each of the data sets well. Moreover, the parameter values are much more uniquely defined, with coefficients of variation (CVs) for most parameters below 10%, as obtained from twenty independent optimization runs of the PTA (data included in Appendix D, Table D.1). However, the water diffusivity and occlusion radius have CVs of 217 and 51%, respectively, providing clear indications of model insensitivity to these parameters, as can be easily understood from Figure 5.2. Burst release is so low (Figure 5.2a) that the occlusion radius is negligibly small and can easily be reduced by an order of magnitude without

significantly affecting the model fit. Similarly, water uptake is very rapid (Figure 5.2c) in this system, such that the model results are not affected by changes to the water diffusivity. As the model is insensitive to these parameters, they can be considered constants and can be removed from the PTA optimization, redrawing the objective function and reducing computational time.

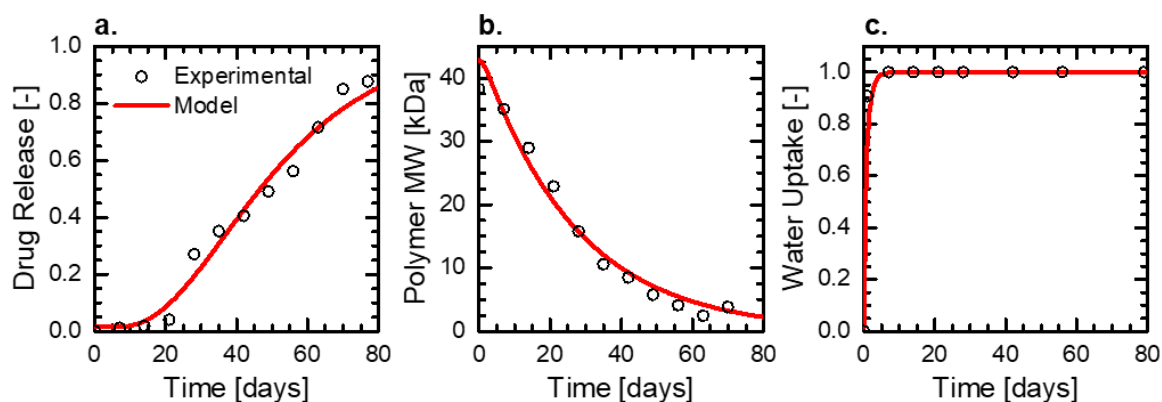


Figure 5.2: Model fitting of the drug release model to experimental data of PLGA solvent depots with initial molecular weight (MW) of 41 kDa [91]: (a) cumulative drug release, (b) polymer degradation, and (c) water uptake.

The PTA parameter estimation can consequently be rerun with the optimized set of parameters to probe the quality of parameter estimation. With the removal of two additional fitting parameters, five parameters are estimated by the PTA for the solvent depot data. The results of twelve PTA runs are included in Appendix D (Table D.2). The CVs of the five parameters in these runs are all below 10%, and the p-values to test for correlations between the parameters are shown in Table 5.4. It is clear that even though this experimental data set contains additional information, including on the polymer degradation process, significant parameter correlations

between the (1) polymer MW at release and drug diffusivity and (2) polymer degradation rate constant and initial polymer MW persist. For the former, neither of these parameters is clearly defined by the experimental data. Rather, both are estimated from the reported rate of drug release. Hence, to guarantee that the model parameters are uniquely defined, one of these parameters should be determined through additional data. For example, the authors of the model have done this through empirical correlations extracted from comprehensive data in the literature [121]. For the latter parameter pair, the correlation is caused mainly by the fact that the model's predicted polymer degradation profile does not agree perfectly with the experimental data, particularly in the early time points, where the model overpredicts the polymer degradation rate of the experimental system (Figure 5.2b). Observations like these indicate that further refinements of the model might be necessary.

### **5.3.3 Model Predictions**

The model predictive capability is assessed by comparing against additional data with variations in initial polymer MW. Using the optimal parameters from the 41 kDa dataset, predictions of the model are compared against the 10 kDa and 56 kDa initial polymer MW data sets, where the initial MW is the only parameter modified. The model predictions and experimental data are compared in Figure 5.3, which shows the excellent model predictions for the 56 kDa PLGA, providing confidence in model validity. However, while the model qualitatively captures the dramatic change in release pattern for the 10 kDa PLGA, it does not quantitatively predict the 10 kDa drug release and polymer degradation profiles.

Table 5.4: P-values for the hypothesis that there is no correlation between the different model parameters for the solvent depot data, based on twelve PTA runs with five fitted parameters (Table D.2 in Appendix D). For the bold values in red, the corresponding parameter correlations are considered significant.

P-values (< 0.05)	Drug diffusivity	Initial polymer MW	Polymer MW at release	Polymer degradation rate constant	Polymer MW SD at release
Drug diffusivity	1.000	0.808	<b>0.000</b>	0.460	0.349
Initial polymer MW	0.808	1.000	0.924	<b>0.042</b>	0.524
Polymer MW at release	<b>0.000</b>	0.924	1.000	0.222	0.820
Polymer degradation rate constant	0.460	<b>0.042</b>	0.222	1.000	0.771
Polymer MW SD at release	0.349	0.524	0.820	0.771	1.000

This discrepancy points to an underlying problem with applying the model to systems with fundamentally different physical states. The poor quantitative accuracy can be attributed to the very different physicochemical properties of the 10 kDa PLGA, which remains a viscous fluid when injected into the release medium, while the higher molecular weight formulations quickly form a solid depot [91]. Model parameters such as diffusivities and degradation rate constants can be expected to be different in a liquid versus a solid phase.

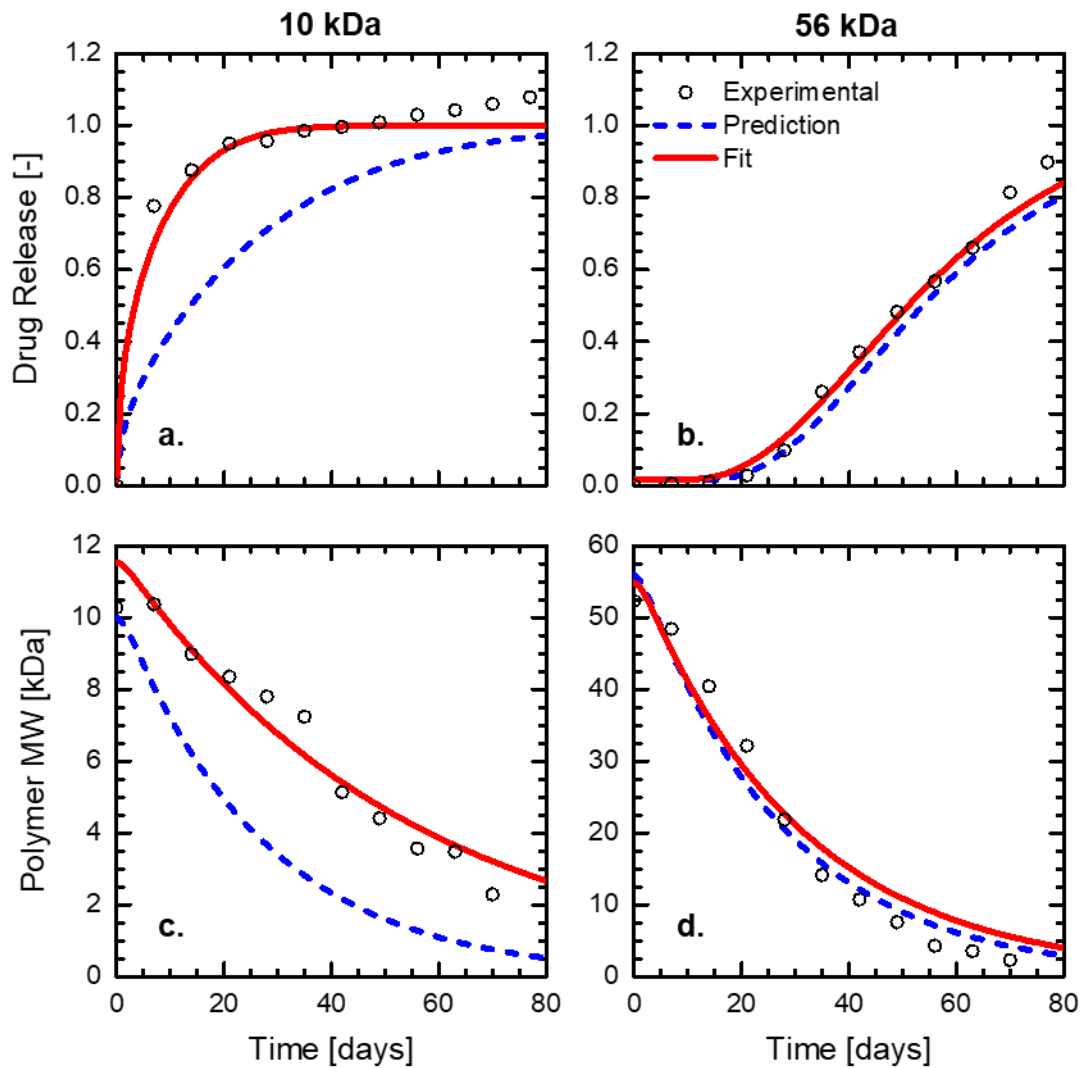


Figure 5.3: Predictions (dashed blue) and simultaneous fits (solid red) of the drug release model to experimental data of PLGA solvent depots with initial MW of 10 kDa (panel a and c) and 56 kDa (panel b and d) [91]: (a-b) cumulative drug release and (c-d) polymer degradation.

In an alternative application of the PTA, the data sets for all three initial polymer MWs can be used to train the model simultaneously. Table 5.5 shows the results of a simultaneous parameter fit where parameter values are required to be same

across the different data sets, with the exceptions of the initial polymer MWs and the drug diffusivity and polymer degradation rate constant for the 10 kDa PLGA. The optimized model results are included in Figure 5.3 (results for the 41 kDa PLGA are similar to those shown in Figure 5.2). Indeed, as anticipated by physical considerations, varying the drug diffusivity and polymer degradation rate enables accurately modeling the experimental results for the 10 kDa PLGA. Furthermore, the parameter changes make physical sense for when the depot is a viscous liquid instead of a solid. Naturally, when additional information is fed to the PTA, it can provide more useful insights, as shown here by the detection of significant deviations of expected parameter values for multiple data sets.

Although only the final optimized parameter values for each run are used here for ease of concept and display, the PTA generates thousands of objective function evaluations during each run. This meta-data can be used in combination with analytical tools to create a better understanding of the relevant parameter space in complex models and large experimental data sets. The advantages of the PTA lie in its ability to identify parameter correlations and model sensitivities, not just inherent to the mathematical model, but with practical relation to specific experimental training sets in those areas of parameter space that are most critical for parameter estimation.

Table 5.5: Optimized parameter values as obtained by simultaneous fitting of the solvent depot data by the PTA. Parameter values in grey are held constant during fitting, bold parameter values in red are fitted independently, and italicized parameter values in green are fitted simultaneously across the different initial PLGA MWs.

Parameter	Units	10 kDa	41 kDa	56 kDa
Drug diffusivity	$\left[10^{-13} \frac{\text{m}^2}{\text{s}}\right]$	<b>5.57</b>	<i>1.28</i>	<i>1.28</i>
Initial drug concentration	[kg/m <sup>3</sup> ]	195	195	195
Water diffusivity	$\left[10^{-12} \frac{\text{m}^2}{\text{s}}\right]$	1.00	1.00	1.00
Maximum water concentration	[kg/m <sup>3</sup> ]	988	988	988
Occlusion radius	[10 <sup>-8</sup> m]	1.00	1.00	1.00
System radius	[10 <sup>-3</sup> m]	1.00	1.00	1.00
Initial polymer MW	[Da]	<b>11540</b>	<b>46693</b>	<b>54866</b>
Polymer MW at release	[Da]	<i>1864</i>	<i>1864</i>	<i>1864</i>
Polymer degradation rate constant	$\left[\frac{10^{-10}}{\text{s}(\text{kg}/\text{m}^3)}\right]$	<b>2.18</b>	<i>3.89</i>	<i>3.89</i>
Polymer MW SD at release	[Da]	<i>10583</i>	<i>10583</i>	<i>10583</i>

#### 5.4 Conclusions

Rational decision-making on (1) the selection and development of predictive models and (2) experiment and formulation design for sustained drug release is enabled by meta-data obtained from a stochastic parallel tempering method (PTA) for parameter estimation. We describe a practical methodology to use the PTA to access and analyze these meta-data with the help of a mathematical model and experimental

data from the literature. In particular, the PTA method in combination with a simple model allows (1) robust generation of near-optimum model solutions while simultaneously fitting different experimental data sets, (2) determination of parameter correlations and model sensitivity based on available data, and (3) guidance in the experimental design of desired release profiles.

## Chapter 6

### DESIGN OF SUSTAINED RELEASE BIOPHARMACEUTICAL SYSTEMS THROUGH MODEL PREDICTIONS

While the previous chapter focused on the methodology of using the parallel tempering algorithm (PTA) to estimate model parameters, the discussion in this chapter is on the validation of the model and the application of this methodology to investigate long-term, sustained release from experimental biopharmaceutical systems.

#### 6.1 Introduction

The molecular size and complexity of biopharmaceuticals gives them the advantage of high potency and specificity, but makes them challenging to formulate – as discussed in previous chapters – as well as to deliver [7]. Their size leads to reduced permeation through biological barriers, while their complexity makes them prone to loss of activity due to environmental triggers. Long-term, sustained delivery systems are promising approaches to increase the bioavailability of biotherapeutics and reduce the need for frequent administration of the drug [111,112,129]. While such delivery systems have been relatively successful for small-molecule drugs, their design and application for large-molecule biopharmaceuticals is also challenged by the size and complexity of these drugs. Most patents, applications currently on the market, and experimental studies in the literature consequently relate to small-molecule drugs or small peptides [119,121,129–131]. Hence, further investigation of sustained delivery systems for large molecules is warranted to broaden their use in biotherapeutic applications, but detailed experimental studies on these systems can require excessive

amounts of time. The understanding and development of such systems can be accelerated with the aid of mathematical models, such as the one described in the previous chapter. Models that are sufficiently accurate can elucidate the important mechanisms and corresponding design parameters and predict the expected drug release profile *a priori*. However, guaranteeing the accuracy of these models is inherently difficult, and confidence in the predictive capabilities generally relies on some experimental validation of the model. A carefully selected experimental test system is consequently required to validate a model for future use in formulation development.

The design of specific drug release profiles is a particularly important example of how the development of biotherapeutic sustained-release formulations can be informed by model predictions. The tight control of the release profile *in vitro* or *in vivo* is a major challenge in the design of sustained-release formulations. A minimum amount of release per day is generally required to keep the bioavailability of the drug at a sufficient level to maintain the biotherapeutic effect, but excessive release can be toxic or decrease the overall lifetime of the sustained-release system. Indeed, a common problem is burst release, in which a significant amount of drug is delivered during the first phase of release [7,132]. Although any of a number of different release profiles can be preferred, depending on the requirements of a specific application, a logical, desirable release profile based on the previous restrictions is a linear (zeroth-order) one. Such a release profile is desired for biotherapeutic applications as it leads to a constant drug release per day over the lifetime of the system, but it is practically challenging to achieve. Poly(lactic-co-glycolic acid) (PLGA) is a common material used for sustained delivery systems as it is mechanically strong, hydrophobic, and

biocompatible [7,111,113,116,131,133]. Moreover, its speed of degradation can be manipulated by altering the polymer composition and its degradation products are toxicologically acceptable products that are naturally removed from the body. However, PLGA systems generally lead to either rapid first-phase release or exhibit a lag phase with tri-phasic release.

Here, the model and methodology described in the previous chapter are used to predict the drug release from two different experimental systems, with the intention to (1) test the broad applicability of the model, (2) investigate the capacity of the model to aid in the design of such experimental systems, and (3) gain key insight into these systems to inform future developments. While a wide variety of drug release models are available in the literature [114–119,134,135], the model introduced in the previous chapter was specifically chosen and adapted from Little *et al.* to provide predictive capabilities for typical sustained drug release systems [121–123]. The two experimental systems are (1) injectable solvent depots and (2) implantable solid rods, systems that have been reported on extensively in the literature but that are relatively unexplored for large-molecule drugs [91,129,136]. The main goal of the solvent depot system is to create an experimental PLGA formulation with a linear (zeroth-order) release profile. Here, we have used design principles obtained from mathematical model fits to an ideal release profile to inform the development of an experimental solvent depot system with such a release profile.

The main goal of studying the experimental rod system is to validate the mathematical model while obtaining fundamental understanding of important drug release mechanisms. Although many experimental systems for studying drug release kinetics have been described in the literature [119,121,129–131], they often focus on a

particular drug or application, and insufficient information is available to study the degradation and drug release processes and understand their effects on the model parameters. Here, we have created a model experimental system consisting of nine different PLGA-based formulations with varying properties that directly correspond to model parameters, allowing direct observation of the effects of changing model parameters on drug release *in vitro*. During the degradation and drug release of the rods, critical system characteristics incorporated in the model, such as polymer molecular weight, polymer polydispersity, rod erosion, drug release, and water uptake are monitored over a period of fifteen weeks to validate model mechanics. Moreover, a surrogate drug in the form of fluorescently labeled dextran is used to generalize the release of large-molecule drugs and to allow direct imaging of the microstructure and drug distribution within the rods.

## **6.2 Materials and Methods**

### **6.2.1 Materials**

Amber glass vials of volume 4 mL and tetrahydrofuran (THF) Optima™ were obtained from Fisher Scientific (Hampton, NH). Phosphate-buffered saline (PBS) packets and stock solution containing Tween 20 (polysorbate 20, PS20) and azide were purchased from Millipore-Sigma (Burlington, MA) and were used to prepare PBS with 0.01% PS20 and 0.02% azide (PBS TN). Fluorescein isothiocyanate (FITC), dextran (from *Leuconostoc spp.* with MW 6 and 40 kDa), and dibutyltin dilaurate were obtained from Sigma–Aldrich (St. Louis, Missouri). Poly(lactic-co-glycolic acid) (PLGA) polymers (RG 505S, RG 752H, RG 755S, RG 756S, 7525 DLG 4A, and 8515 DLG 5A) were obtained from Evonik Industries AG (Essen,

Germany). A fragment antibody (Fab1) was supplied by Genentech, Inc. (South San Francisco, CA).

### 6.2.2 Mixed Solvent Depot Preparation

Solvent depots were prepared in triplicate and subjected to *in vitro* release studies at Genentech as described previously [91], with spray-dried Fab1 particles obtained by the procedure in Section 3.2.3. In contrast with this prior work, which was the basis for the solvent depot studies in the previous chapter, three PLGA polymers, RG 752H, RG 755S, and RG 756S, labeled Polymer I (7 kDa), Polymer II (36 kDa), and Polymer III (55 kDa), respectively, were mixed here in three formulations to obtain polymer blends with varying polydispersity but with similar weight-averaged molecular weights ( $MW_w$ ), listed in Table 6.1. These polymers correspond to those used in the previous chapter, to guarantee transferability of the model parameters, except for the lowest MW polymer, which was not available for this study. However, the 7 kDa PLGA is expected to exhibit similar characteristics as the 10 kDa PLGA of Chapter 5. As a control, the pure PLGAs were also prepared in three additional formulations (Table 6.1). The number-averaged and weight-averaged MWs ( $MW_n$  and  $MW_w$ ) are related to the polydispersity index ( $PDI = MW_w/MW_n$ ) and the polymer number-averaged MW standard deviation ( $\sigma_n$ ) through [137]

$$\frac{\sigma_n^2}{M_n^2} = PDI - 1. \quad (6.1)$$

Table 6.1: Solvent depot formulation compositions, weight- and number-averaged molecular weights ( $MW_w$  and  $MW_n$ ), polydispersity indices ( $MW_w/MW_n$ , PDI), and glass transition temperatures ( $T_g$ ). MW and PDI values were determined at Genentech using gel permeation chromatography.

Formulation	Polymer Formulation [Mass Fraction]			$MW_w$ [kDa]	$MW_n$ [kDa]	PDI [-]	$T_g$ [°C]
	Polymer I (7 kDa)	Polymer II (36 kDa)	Polymer III (55 kDa)				
1	0.1	0.8	0.1	60.9	19.1	3.2	-
2	0.2	0.6	0.2	61.8	18.3	3.4	-
3	0.4	0.2	0.4	63.4	12.6	5.0	-
4	1	0	0	13.1	7.2	1.8	41
5	0	1	0	64.3	35.7	1.8	47
6	0	0	1	117.7	55.2	2.1	46

### 6.2.3 Rod Design

A set of nine PLGA rod formulations was designed with the aim of studying the effect of important rod properties that are directly related to parameters in the mathematical model (Table 6.2). The experiment was set up around one reference formulation (A), with other formulations varying a specific design parameter to either a lower (−) or higher (+) value. Five parameters were explored, and formulations are identified by the parameter varied and its value relative to that of the reference sample (Table 6.2). Due to lack of practical relevance and to material constraints, the lower rod radius and higher drug molecular weight were not considered. Instead of a biopharmaceutical drug, dextran labeled with fluorescein isothiocyanate (FITC-dextran) was used as a surrogate model drug, which allowed control of the MW, detection of the drug release through fluorescence intensity of the release buffer, and imaging of the drug particle distribution within the PLGA rods.

Specific PLGA grades used for each formulation are listed in Table 6.3, where the first four digits indicate the L/G ratio, the number after DLG corresponds to the ratio of the intrinsic viscosity to the molecular weight (IV/MW, higher value corresponds to larger MW), and the last letter stands for the end group (A for acid and S for ester). Polymers with higher L/G ratios will degrade more slowly. In addition, PLGAs with ester end groups will generally degrade more slowly than those with acid end groups. Although the same end group should have been used for direct, fair comparisons of the formulations, two PLGAs with acid end groups were used here due to the limited availability of the polymers.

Table 6.2: PLGA rod design parameters for nine different formulations. Bold values in red indicate variations from the reference formulation A.

Parameter	Symbol	Units	Formulation								
			A. Ref	B. R+	C. MW <sub>0-</sub>	D. MW <sub>0+</sub>	E. C <sub>D,0-</sub>	F. C <sub>D,0+</sub>	G. MW <sub>D-</sub>	H. L/G-	I. L/G+
Rod radius	$R$	[mm]	0.25	<b>0.5</b>	0.25	0.25	0.25	0.25	0.25	0.25	0.25
Polymer initial molecular weight	$MW_0$	[kDa]	60	60	<b>50</b>	<b>110</b>	60	60	60	60	60
Initial drug concentration	$C_{D,0}$	[w %]	15	15	15	15	<b>5</b>	<b>25</b>	15	15	15
Drug molecular weight	$MW_D$	[kDa]	40	40	40	40	40	40	<b>6</b>	40	40
L/G ratio	$L/G$	[%L: %G]	75:25	75:25	75:25	75:25	75:25	75:25	75:25	<b>50:50</b>	<b>85:15</b>

Table 6.3: PLGA grades used for each of the nine different formulations. Grades in red italics indicate variations from the reference formulation A.

<b>Formulation</b>	<b>PLGA grade</b>
A. Ref	7525 DLG 5S (RG 755S)
B. R+	7525 DLG 5S (RG 755S)
C. MW <sub>0-</sub>	<i>7525 DLG 4A</i>
D. MW <sub>0+</sub>	<i>7525 DLG 6S (RG 756S)</i>
E. C <sub>D,0-</sub>	7525 DLG 5S (RG 755S)
F. C <sub>D,0+</sub>	7525 DLG 5S (RG 755S)
G. MW <sub>D-</sub>	7525 DLG 5S (RG 755S)
H. L/G-	<i>5050 DLG 5S (RG 505S)</i>
I. L/G+	<i>8515 DLG 5A</i>

#### 6.2.4 Spray-Drying and Characterization of FITC-Dextran

Spray-dried FITC-dextran was prepared and characterized at Genentech. To prepare FITC-dextran, 1 g dextran was dissolved in 10 mL dimethyl sulfoxide (DMSO) containing a few drops of pyridine. Consecutively, 0.1 g fluorescein isothiocyanate and 20 mg dibutyltin dilaurate were added, and the mixture was heated for 2 h at 95 °C to perform conjugation. This procedure was scaled up linearly for larger batches. The FITC-dextran was lyophilized after several precipitations in ethanol to remove the free dye.

Lyophilized FITC-dextran was formulated at 20 mg/mL in 10 mM histidine-HCl buffer with 0.02% (w/v) polysorbate 20 at pH 5.5 for spray drying. The formulated FITC-dextran solution was spray-dried using a Buchi laboratory-scale spray-dryer model 191 (Buchi Labortechnik AG, Flawil, Switzerland) with inlet and outlet temperatures of 90 °C and 60 °C, respectively. The collected spray-dried powder was secondary-dried overnight and stored at 4 °C until further use.

The particle size distributions of spray-dried FITC-dextran formulations were measured using a Horiba Partica LA-950V2 laser diffraction particle size distribution analyzer (Horiba Ltd., Kyoto, Japan). Approximately 1 mg of spray-dried powder was dispersed in 1 mL of isopropanol and the dispersion was added drop-wise to 50 mL isopropanol until a target light obscuration level was achieved. The refractive index of isopropanol (1.3776) was used to calculate the size distribution using the particle-sizing program. The mean particle size for the 6 and 40 kDa FITC-dextran spray-dried particles was 6.6 and 5.9  $\mu\text{m}$ , respectively.

The glass transition temperature ( $T_g$ ) of the spray-dried FITC-dextran particles was measured by modulated differential scanning calorimetry (MDSC, TA Instruments Q2000, New Castle, DE). Approximately 1 – 3 mg of sample and an empty reference pan were sealed in a TA hermetical aluminum pan. The MDSC experiments were performed by equilibrating the samples and reference pan to 5  $^{\circ}\text{C}$  for 10 minutes, modulating  $\pm 1$   $^{\circ}\text{C}$  every 60 seconds, and then heating to 200  $^{\circ}\text{C}$  at a rate of 2  $^{\circ}\text{C}/\text{min}$ . The  $T_g$  was determined as the glass transition midpoint in the reversing signal and was found to be 92.6 and 104.7  $^{\circ}\text{C}$  for the 6 and 40 kDa dextran-FITC, respectively.

### **6.2.5 Extrusion of Rods**

Hot-melt extrusion was performed at Genentech using a Haake Minilab conical counter-rotating twin-screw extruder (Thermo Scientific, Karlsruhe, Germany). The extruder barrel was pre-heated to 90  $^{\circ}\text{C}$  and the screw speed was set to 30 rpm. The pre-weighted solid PLGA and spray-dried FITC-dextran were starve-fed slowly into the extruder and re-circulated back to the barrel for micro-compounding. The melt-phase blending was continued for 30 min after complete feeding and then extruded

through a 0.5 mm or 1.0 mm circular die. The extrudate was cooled to room temperature, cut to cylinders of desired length using a razor blade and stored in glass vials until further use.

#### **6.2.6 Experimental Setup of Rods**

All rod studies were performed in triplicate for each of the nine formulations. One sample set of 27 samples was prepared for drug release studies, while separate, sacrificial sample sets were prepared for water uptake, rod erosion, and polymer degradation studies, which required one sample set every two weeks. For each sample, the polymer rods were cut into five 1 mg segments and placed in a labeled 4 mL amber glass vial. The exact weight of the empty vials and rods was recorded so that the drug release, water uptake, and rod erosion could later be normalized to the exact rod mass. Before the vials were capped, 1 mL of the release buffer (PBS TN) was added. For the drug release studies, the capped vials were sealed with plastic film to minimize evaporation. Vials were then incubated at 37 °C. The release buffer was replenished on day 1 and then every 7 days. At each of these time points, the release buffer (PBS TN) was completely pipetted out, 1 mL of fresh PBS TN was pipetted into the vials containing rods, and the vials were returned to 37 °C.

#### **6.2.7 Measurement of Drug Release from Rods**

For the *in vitro* drug release studies, the release buffer was collected in 2 mL low-bind Eppendorf tubes each week for twelve weeks and at week 15. The drug concentration in the collected buffer was measured by fluorescence intensity with a Synergy™ 2 multi-mode microplate reader (BioTek, Winooski, VT). The fluorescence intensity was calibrated using standards created from the spray-dried FITC-dextran

with a range from 0.001 mg/mL to 1 mg/mL. Samples with a measured concentration above 0.06 mg/mL were diluted to avoid the non-linear regime, which occurred above this concentration due to the inner filter effect.

### 6.2.8 Water Uptake and Rod Erosion Measurements

Water uptake, rod erosion, and polymer degradation studies were performed in triplicate on sacrificial sample sets on day 1 and week 1 and then every 14 days for eleven weeks. At each of these time points, the release buffer (PBS TN) was completely pipetted out of a sacrificial sample set and the contents of the vials were rinsed with 1 mL of deionized water to remove any excess degradation products or excipients. To measure water uptake (WU) and rod erosion (RE), any remaining water on the vial and rod surface was removed by placing the vials in a vacuum desiccator for 30 minutes. Subsequently, the mass of the rods was recorded as wet mass ( $M_{r,w}$ ). The rods were then placed in a vacuum desiccator for two weeks. The rod mass was measured every other day and drying was continued until the rod mass remained constant for at least four consecutive days. This mass was recorded as dry mass ( $M_{r,d}$ ). Water uptake was defined as

$$WU = \frac{M_{r,w} - M_{r,d}}{M_{r,d}} \quad (6.2)$$

Rod erosion, characterized by the remaining rod mass ( $M_{r,r}$ ), was calculated from the initial mass of the rod before hydration for release ( $M_{r,i}$ ) and the dry mass of the rod at time  $t$  as

$$M_{r,r} [\%] = \frac{M_{r,d}}{M_{r,i}} \times 100. \quad (6.3)$$

### 6.2.9 Polymer Degradation by Gel Permeation Chromatography

After dry mass measurements, the sacrificial samples sets were dissolved in THF and filtered through a 0.22  $\mu\text{m}$  PVC syringe filter as preparation for molecular weight (MW) determination of the PLGA. Gel permeation chromatography (GPC) analysis was performed using a Waters Alliance 2695 HPLC system (Waters Corporation, Milford, MA) equipped with a Waters 2414 refractive index (RI) detector and Phenogel™ 5  $\mu\text{m}$  10E4A (300  $\times$  7.8 mm) and Phenogel™ 5  $\mu\text{m}$  100A (300  $\times$  7.8 mm) columns in series (Phenomenex, Torrance, CA). THF was used as the mobile phase at a flow rate of 1.0 mL/min. The GPC columns were calibrated with polystyrene standards with a range of 1.78 kDa to 205 kDa. A 100  $\mu\text{L}$  injection volume was used with a target PLGA concentration of 2 mg/mL. The PLGA number- and weight-averaged MWs ( $MW_n$  and  $MW_w$ ) and the polydispersity index (PDI) were estimated from the GPC chromatograms and polystyrene standard calibration data.

### 6.2.10 Confocal Fluorescence Microscopy

The dextran was labeled with FITC using the methods described above. Dry rods were imaged using confocal fluorescence microscopy (CFM) both as received (Day 0) and after 7 weeks of *in vitro* release. The rods were immersed in freezing medium (Electron Microscopy Sciences Tissue Freezing Medium 72592, Hatfield, PA) and immediately frozen in liquid nitrogen. The rods in the frozen blocks were cross-sectioned into 10  $\mu\text{m}$  slices using a Leica CM3050 S Cryostat (Wetzlar, Germany) in combination with Surgipath Adhesive Coated Slides from the Leica CryoJane™ Tape-Transfer System. After transfer of the slices onto the slides, they

were directly exposed to nitrogen gas to sublimate water from the freezing medium. Slices on the slides were then suspended in immersion oil (Zeiss Immersol 518F, refractive index 1.52) and imaged on a Zeiss LSM 710 laser scanning confocal microscope (Jena, Germany). The optical resolution of the instrument was approximately 0.15  $\mu\text{m}$ , while the pixel size was below 0.14  $\mu\text{m}$  in the focal plane (x/y-direction) and below 0.4  $\mu\text{m}$  out of the focal plane (z-direction) for all images. Zen Blue Edition software was used to reconstruct detailed images of the rod cross-sections from 25 individual tile images and to obtain maximum-intensity projections from image stacks in the z-direction. The particle fraction in the cross-sectional images was determined by using the default *Binary* function in combination with the *Analyze Particle* function in Fiji (ImageJ 1.52c) [138].

### **6.3 Results and Discussion**

The two experimental systems are discussed in the following order. First, model parameters obtained in the previous chapter for the solvent depot system were used in conjunction with the parallel tempering algorithm (PTA) to develop an experimental system that shows a specific release profile. The broad applicability and underlying mechanisms of the mathematical model were then tested using a model system of PLGA rods.

#### **6.3.1 Designing a Linear Release Profile**

A hypothetical linear (zeroth-order) release profile with continuous release for 100 days is shown in Figure 6.1. To obtain insight into how to create a PLGA-based solvent depot that releases drug according to this profile, the mathematical model

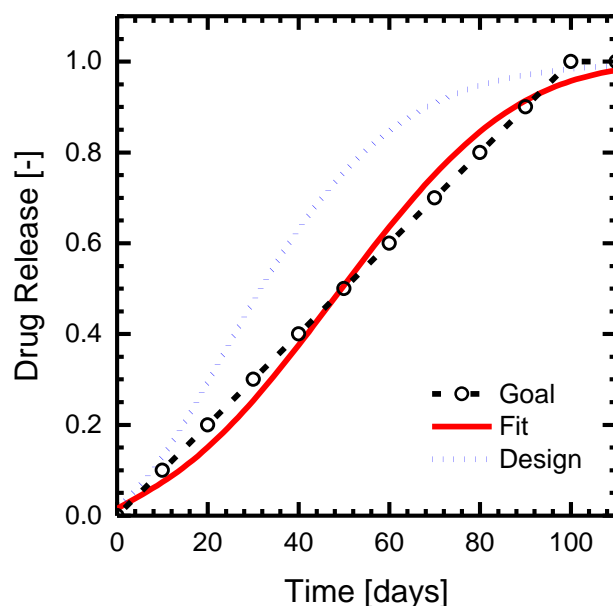


Figure 6.1: Comparison between the desired release profile, which is linear (zeroth-order) over a period of 100 days (black symbols and dashed line), and the optimized release profile obtained from a fit of the model and parallel tempering algorithm (red solid line). The actual experimental design (blue dotted line) is based on the design principles of the optimal fit but is limited by the PLGA polymers available for this study.

(Section 5.2.1) is fit to the release profile with the PTA following the methodology described in Chapter 5, with initial values obtained from the model fits to the published solvent depot data for the 41 kDa PLGA (first column in Table 6.4) [91]. The PTA algorithm was run multiple times from the same initial values, with one of the results shown by the red solid line in Figure 6.1 and the corresponding optimal parameter values included in Table 6.4. In general, all optimized runs showed only small changes in the rod radius and the polymer molecular weight at release, and fluctuating but relatively minor variations in the drug diffusivity. However, all runs

showed a significant increase in the initial polymer molecular weight ( $MW_0$ ) and a decrease in the polymer degradation rate constant, which is consistent with the model's attempt to reach the long 100-day release time.

More interesting is that all optimization runs showed a large increase in the polymer standard deviation (SD) at release ( $\sigma_r$ ), with the particular design feature that the ratio between the polymer SD at release and the average initial polymer MW ( $\sigma_r/MW_0$ ) is approximately 0.32. This observation points towards the requirements to obtain a linear release profile in the model. The polymer SD indicates the degree of polydispersity of the polymer within the solvent depot. As the rate of drug release in the model is directly related to rod erosion, and rod erosion is linked to the fraction of the polymer MW that has reached the MW of release (Equation 5.4), a large polydispersity will generally lead to increased drug release. If the SD is relatively high compared to the average initial polymer MW, a large fraction of the polymer will have sufficiently low MW to be eroded from the onset, and the drug will experience fast, first-phase burst release. Conversely, if the SD is relatively low, the polymer will have to degrade for a certain period of time before a significant fraction of the polymer will have reached the MW of release, leading to an initial lag and a sigmoidal release profile. The observation that all optimization runs show a  $\sigma_r/MW_0$  of approximately 0.32 indicates that to reach a linear release profile, the formulation needs to maintain a tight balance between a sufficiently high SD to allow drug release from the onset and a sufficiently low SD to prevent burst release. From a formulation development perspective, the formulation needs to have a high, but precise, polydispersity index (PDI). This insight reflects the ability to develop a constant rate of release by using a spectrum of polymer molecular weights sufficiently broad, so as to permit sufficient

short time release by the more rapid degradation of the smaller MW fraction while maintaining release throughout the time duration by the degradation of progressively higher MW fractions. However, how accurately this insight from the mathematical model applies to the real-life solvent depot systems must be evaluated experimentally.

Table 6.4: Model parameters to obtain linear release profiles in solvent depot systems. Bold values in green were fit with the parallel tempering algorithm, while italic values in blue were adjusted manually.

Parameter	Units	Fit	Design	Predictions		
				1:8:1	2:6:2	4:2:4
Drug diffusivity	$\left[10^{-13} \frac{\text{m}^2}{\text{s}}\right]$	<b>5.32</b>	1.12	1.12	1.12	1.12
Initial drug concentration	[kg/m <sup>3</sup> ]	195	195	195	195	195
Water diffusivity	$\left[10^{-12} \frac{\text{m}^2}{\text{s}}\right]$	1.00	1.00	1.00	1.00	1.00
Maximum water concentration	[kg/m <sup>3</sup> ]	988	988	988	988	988
Occlusion radius	[10 <sup>-8</sup> m]	1.00	1.00	1.00	1.00	1.00
System radius	[10 <sup>-3</sup> m]	<b>1.23</b>	1.00	1.00	1.00	1.00
Initial polymer MW	[Da]	<b>72795</b>	20000	19100	18300	12600
Polymer MW at release	[Da]	<b>2326</b>	2879	4120	4120	4120
Polymer degradation rate constant	$\left[\frac{10^{-10}}{\text{s}(\text{kg}/\text{m}^3)}\right]$	<b>1.72</b>	3.96	3.96	3.96	3.96
Polymer MW SD at release	[Da]	<b>21989</b>	6400	6112	<i>10586</i>	<i>18336</i>

The accuracy of this design was validated by comparison with experimental measurements on release from Fab1-loaded solvent depots. High PDIs were achieved by mixing commercially-available PLGA polymers with broadly varying MWs. An advantage of this approach is the ability to directly control the degree of polydispersity, but a potential complication lies in the fact that the polymer MW distribution becomes multimodal, while the mathematical model assumes a continuous, monomodal distribution. Note that the mathematical model only uses the mean and polydispersity, and so mixing components can generally match these two design parameters and approximate the continuous distribution. The degradation rate constant of the PLGA can be controlled by changing the lactic/glycolic molar ratio (L/G). The degradation rate constant of  $1.72 \times 10^{-10} [\text{s}(\text{kg}/\text{m}^3)]^{-1}$ , proposed by the model fitting (Table 6.4), is expected from an L/G of 85:15. However, due to limitations in the available materials, and to keep these experiments consistent with the solvent depot systems used to train the model in Chapter 5, the three PLGA grades used to create the mixed solvent depots are the same as those fit in Chapter 5 (with a small change to the lowest MW PLGA, see Section 6.2.2). As these PLGAs have an L/G of 75:25, they will degrade faster, and mixtures of these PLGAs will have average MW below those suggested by the model fit. Consequently, the overall lifetime of the experimental drug release system is expected to be lower than 100 days. However, following the semi-empirical design rule  $\sigma_r/MW_0 = 0.32$  should maintain the linear release profile. The model parameters for this system were directly adopted from the fits to the solvent depot system (Table 5.5), with an average initial number-averaged MW of 20 kDa to take mixing into account and a polymer MW SD at release of 6400 as obtained from the design rule (second column in Table 6.4). As

expected, following the rule leads to a fairly linear predicted release profile, but the duration of release is decreased to approximately 60 days (blue dotted line in Figure 6.1).

As the translation of the high polydispersity of the model to the experimental system is not straightforward, particularly due to the change in MW distribution, three formulations with different mixing ratios were created to probe the effect of the PDI. The three formulations contain mass ratios of 1:8:1, 2:6:2, and 4:2:4 of the low (7 kDa), medium (36 kDa), and high (55 kDa) number-averaged MW PLGA and are listed in Table 6.1, along with general properties. Note that the relative ratios of the polymer grades keep the weight-average MW fairly constant among the three formulations, so that the increase in PDI among the formulations is the main parameter investigated. Release profiles for the Fab1-loaded pure PLGAs were also obtained as controls.

The experimental release profiles for the three mixed formulations (closed symbols) and the three pure PLGAs (open symbols) are shown in Figure 6.2. The 1:8:1 formulation, with a PDI of 3.2, follows a nearly linear release profile for a period of about 60 days, as predicted by the model design. Clearly, the semi-empirical design principle obtained from the mathematical model is successful for creating the desired release profile *in vivo*. The other two formulations have higher PDIs that lead to an increasing amount of first-phase release, but they still show a reasonable monotonicity for the subsequent release.

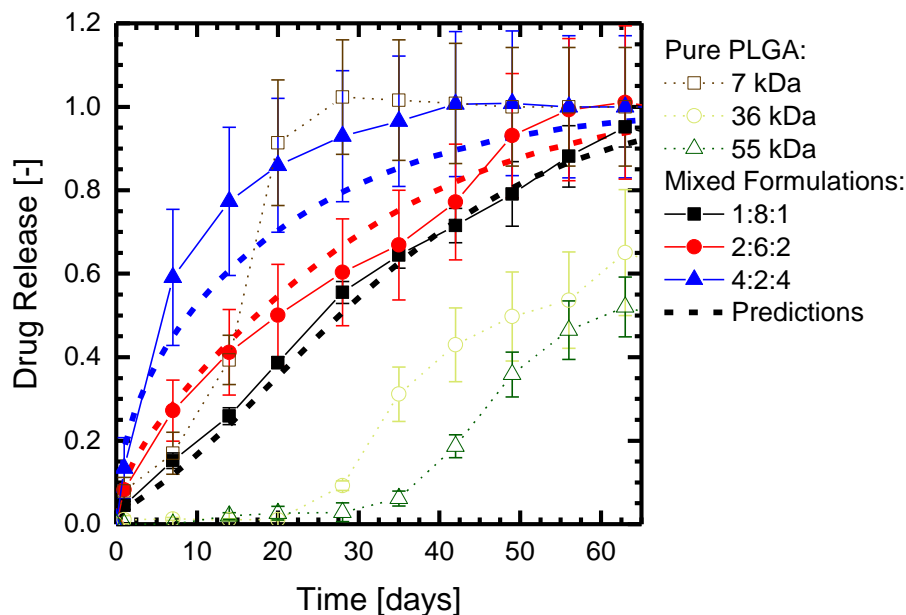


Figure 6.2: Comparison between model predictions (dashed lines) and experimental data (closed symbols) for the mixed PLGA solvent depot system with varying mass fraction compositions of the pure PLGAs (pure PLGA release shown in open symbols). The lines connecting the symbols are a guide to the eye. Error bars indicate the standard deviation.

Actual formulation properties, listed in Table 6.1, were used to update the model parameters for these three formulations (last three columns in Table 6.4). For the 1:8:1 formulation, the initial polymer MW was used in conjunction with the  $\sigma_r/MW_0 = 0.32$  design rule to calculate the SD at release, which was then used to calculate the polymer MW at release from the PDI (Equation 6.1). With these accurate parameters, the model predicts the experimental release very well (black dashed line in Figure 6.2). Note that there are no fitted parameters of the model to the experimental mixed solvent depot data; all parameter values were obtained from the pure PLGAs, the mixing ratios, and the design rule. For the two other formulations, the polymer SD

was manually increased to simulate the effect of increasing PDI. The model results qualitatively capture the change of the release profiles to increased burst release, confirming the mechanical interpretation of the design rule (red and blue dashed lines in Figure 6.2). The procedure followed here does not only illustrate how insights from mathematical models can inform model development, leading to a desired release profile in a clinically relevant biotherapeutic system, it also validates the use of the specific model here as being capable of accurately describing the underlying mechanisms in these systems.

### **6.3.2 Predicting the Release of PLGA Rods**

Based on the design of the nine PLGA rod formulations (Table 6.2), predictions of drug release, average polymer MW, and water uptake with time were obtained from the mathematical model. Model parameters, listed in Table 6.5, were either directly adapted from known information about the rod system or estimated based on model fits to the microsphere and solvent depot systems (Chapter 5). Specifically, the rod radius, occlusion radius, and initial polymer MW were obtained directly from the formulation specifications; the drug diffusivity and polymer MW at release were estimated based on published correlations [121]; and other parameter values were estimated based on model fits to the previous datasets. For the polymer degradation rate constant, only the differences in L/G ratio were initially taken into account, and not the effects of the acid end groups of some of the PLGA grades. While some of these estimates might not perfectly transpose to the polymer rod system, one goal of this study is to validate how well the model performs with incomplete information.

Table 6.5: Initial model parameters to predict PLGA rod behavior for the nine formulations. Bold values in red indicate variations from the reference formulation A.

Parameter	Units	Formulations								
		A. Ref	B. R+	C. MW <sub>0-</sub>	D. MW <sub>0+</sub>	E. C <sub>D,0-</sub>	F. C <sub>D,0+</sub>	G. MW <sub>D-</sub>	H. L/G-	I. L/G+
Drug diffusivity	$\left[10^{-13} \frac{\text{m}^2}{\text{s}}\right]$	0.59	<b>2.86</b>	0.59	0.59	0.59	0.59	0.59	0.59	0.59
Initial drug concentration	[kg/m <sup>3</sup> ]	195	195	195	195	<b>65</b>	<b>325</b>	195	195	195
Water diffusivity	$\left[10^{-14} \frac{\text{m}^2}{\text{s}}\right]$	5.00	5.00	5.00	5.00	5.00	5.00	5.00	5.00	5.00
Maximum water concentration	[kg/m <sup>3</sup> ]	650	650	650	650	650	650	650	650	650
Occlusion radius	[μm]	5.00	5.00	5.00	5.00	5.00	5.00	5.00	5.00	5.00
System radius	[10 <sup>-3</sup> m]	0.25	<b>0.50</b>	0.25	0.25	0.25	0.25	0.25	0.25	0.25
Initial polymer MW	[Da]	60000	60000	<b>50000</b>	<b>110000</b>	60000	60000	60000	60000	60000
Polymer MW at release	[Da]	5000	5000	5000	5000	5000	5000	<b>10000</b>	5000	5000
Polymer degradation rate constant	$\left[\frac{10^{-10}}{\text{s}(\text{kg}/\text{m}^3)}\right]$	6.40	6.40	6.40	6.40	6.40	6.40	6.40	<b>12.0</b>	<b>3.31</b>
Polymer MW SD at release	[Da]	10000	10000	10000	10000	10000	10000	10000	10000	10000

An overview of the predicted drug release profiles is shown in Figure 6.3. In general, all formulations show a sigmoidal release profile, with lifetimes between approximately 30 and 80 days. Certain parameter variations are expected to lead to faster release, while others lead to slower release as compared to the reference. Note that the drug loading only affects the absolute amount of release in the model, with no effect on the relative release. Similarly, the change in rod radius has a limited effect on

the release profile. This is due to the fact that water uptake is expected to be rapid, and hence polymer degradation will be fairly homogeneous throughout the rods.

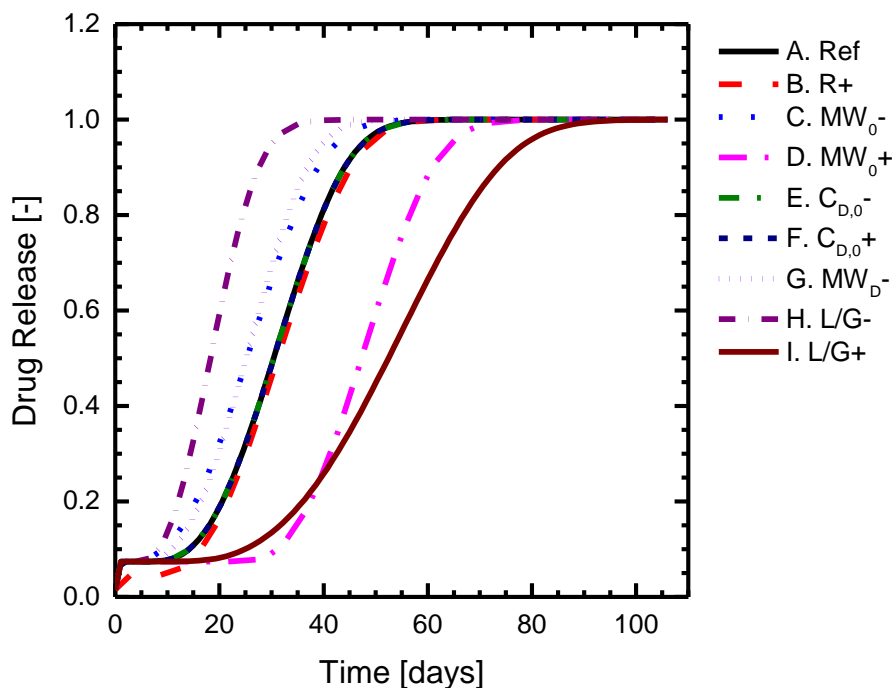


Figure 6.3: Initial model predictions for the cumulative drug release of the nine formulations.

### 6.3.3 Experimental Results for the PLGA Rods

Experimental results for the nine PLGA rod formulations, including drug release, rod erosion, average polymer MW, polymer PDI, and water uptake over time, are shown in Figure 6.4. Several interesting observations can be made from these data. First, most formulations showed a significant amount of first-phase “burst” release and several formulations did not reach complete release within the time frame of the experiment (Figure 6.4a). Second, polymer degradation of the formulation with the

higher L/G ratio (H) was expected to be slower than that of the reference formulation (A), but it was similar if not faster (Figure 6.4c), indicating that the acid end groups affected the degradation rate sufficiently to counteract the effect of increasing L/G ratio. This also affected formulation C ( $MW_{0-}$ ), leading to faster degradation than expected. Third, formulations started to show significant decreases in rod mass when they reached low average MW, as expected due to rod erosion, while other formulations maintained most of their mass (Figure 6.4b). Fourth, the mass that was lost by most formulations correlates with the amount of drug released during the first phase (Figure 6.4a and b), as expected. For example, formulation F ( $C_{D,0+}$ ) lost 20% of its mass in the first couple of weeks, but this corresponds to the approximately 25% of loaded drug that was lost during that time. Fifth, water uptake of most rods happened quickly and the amount taken up remained fairly constant between 20 and 60% of the original rod weight (Figure 6.4f). However, when rods started eroding (formulations C, H, and I), they showed significant increases in water uptake, up to several times their original weight (Figure 6.4e), which was enabled by swelling of the polymer rods (visual observations, data not shown). Note that the sudden decreases in water uptake for formulations C and H are artifacts due to loss of rod mass. Lastly, the PDI of all formulations remains constant around a value of 2 throughout the time frame of the experiment, even though the average MW decreased significantly.

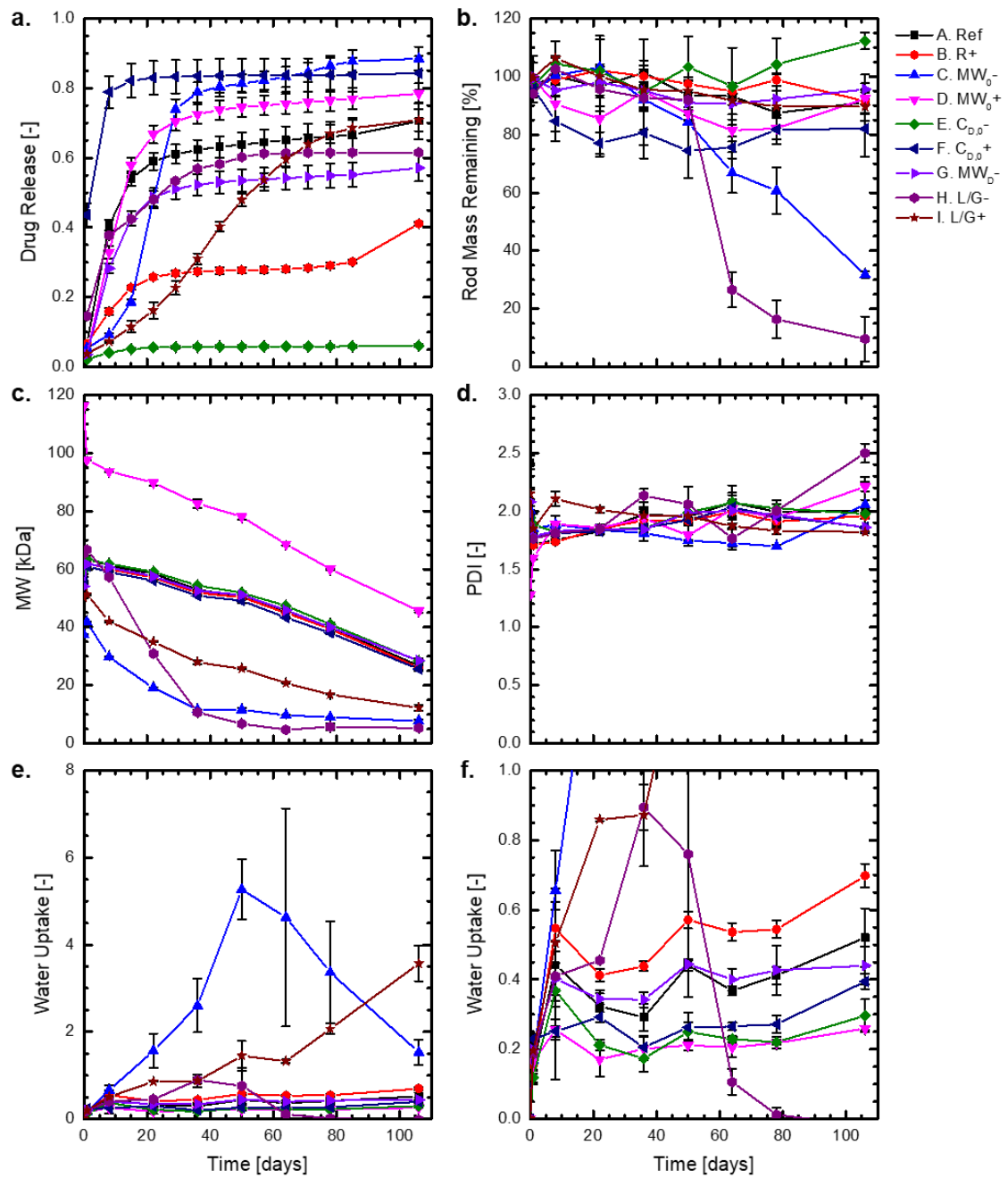


Figure 6.4: Experimental data for the PLGA rod system, including drug release, remaining rod mass, PLGA MW, PDI, and water uptake at two different scales. The lines connecting the symbols are a guide to the eye. Error bars indicate the standard deviation.

Comparisons of the drug release, average polymer MW, and water uptake for the formulations that appear to reach complete release and the initial model predictions are shown in Figure 6.5, while comparisons for the formulations that do not reach complete release are included in Figure 6.6. For the formulations that do reach complete release, the experimental release profiles are scaled to reach 100% release at week 15 to allow fair comparison with the model predictions. In addition, water uptake in these figures is shown as a fraction of maximum water uptake, and for the formulations that show significant water uptake due to erosion and swelling, only the first few data points, before swelling, are included in the water uptake profile.

Although the model did not predict the first-phase release, it predicts the overall release and average MW profiles of the formulations that reach complete release quite well (Figure 6.5). Particularly impressive are the close predictions for formulations C, H (disregarding first-phase release), and I. The main reason that the model did not accurately predict the drug release of the other formulations appears to be the fact that the polymer degradation rate is much slower than anticipated (second column in Figure 6.6). This could be due to a difference in the apparent degradation rate of PLGA in solvent depots and rods. Consequently, the degradation rate constant for these formulations should be adjusted to follow the experimental average MW data.

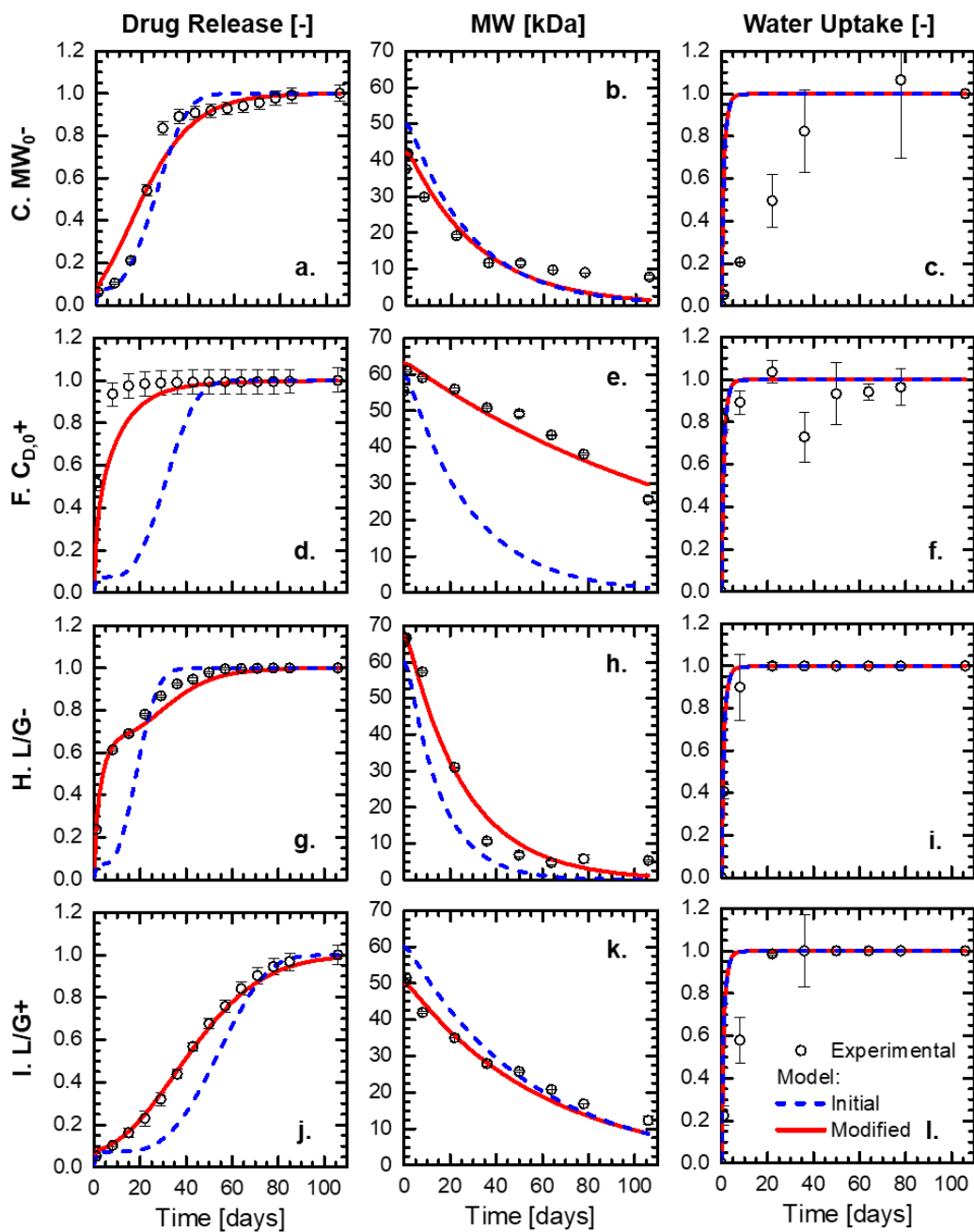


Figure 6.5: Comparison between model predictions (dashed blue lines) and experimental data (symbols) for the PLGA rods that exhibited apparent complete release. The experimental cumulative drug release was scaled to reach complete release (1.0) after 15 weeks. Model results with modified parameter values based on observed phenomena are shown by the red lines.

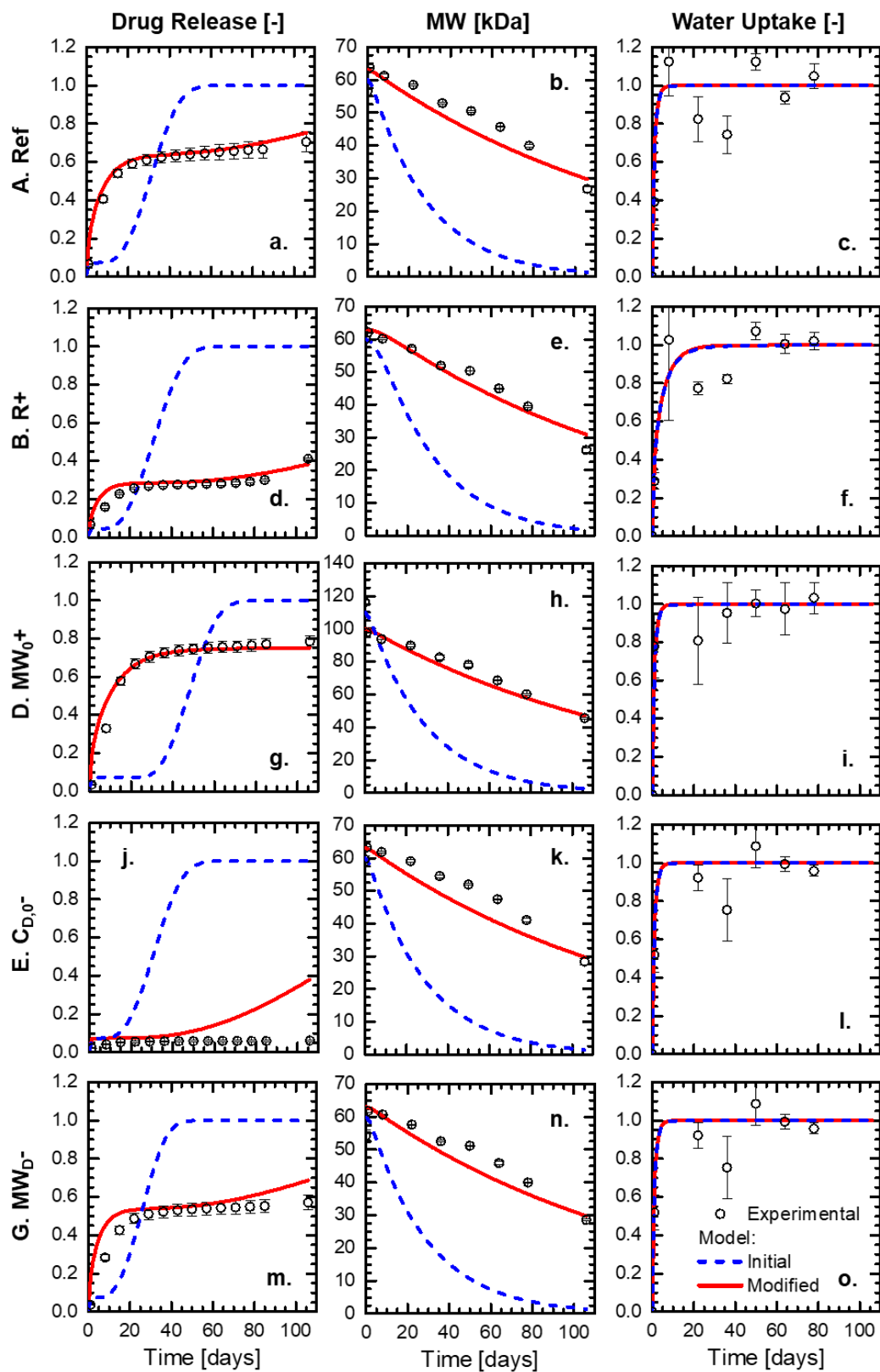


Figure 6.6: Comparison between model predictions (dashed blue lines) and experimental data (symbols) for the PLGA rods that exhibited incomplete release. Model results with modified parameter values based on observed phenomena are shown by the red lines.

#### 6.3.4 Relation between Rod Microstructure and First-Phase Release

A significant discrepancy between the model predictions and the experimental release profiles is the underprediction of the extent of the first-phase release observed experimentally. As mentioned in the solvent depot discussion, the model predicts fast, first-phase release when the polymer MW standard deviation is high compared to the initial MW, leading to rapid erosion and drug release. In this case, drug release is expected to reach 100% quickly, but this is not realized for any of the formulations showing first-phase release other than formulation F ( $C_{D,0+}$ , Figure 6.5d). However, for this formulation the onset of erosion is clearly not reached, as there is no rod erosion, low MW, or significant water uptake. Another way the model incorporates first-phase release is burst release through the occlusion radius, which takes into account drug that is quickly released from a particle surface layer that is expected to have a thickness the size of the drug particle radius (approximately 5  $\mu\text{m}$  here). Clearly this factor alone does not explain the degree of burst release observed here.

Instead, we hypothesize that the more extensive first-phase release seen experimentally is caused by percolation of the drug particles within the rods. Percolation refers to the interconnectivity of clusters, pores, or particles in space. For a system of infinite size, the percolation threshold occurs at a volume fraction of percolating objects that depends on the geometry of the voids, but not on their size. For spherical particles forming a 3D continuous network, the percolation threshold is 0.29 (allowing overlap) or 0.20 (without overlap, jammed) [139,140]. Consequently,

the drug particles within the rods are expected to form an interconnected network when the volume fraction of drug particles has a value close to 0.20 or above, presumably leading to fast water penetration and pore formation. When the volume fraction approaches this value, the probability of finding larger and larger networks within the rods increases. For comparison, FITC-dextran starts releasing from porous polylactic acid (PLA) microspheres when the matrix porosity reaches a value between 0.26 and 0.34 [141].

The existence of a percolated network would explain why there is rapid burst release from formulation F ( $C_{D,0+}$ ), which has a particle mass fraction of 25%, while formulation E ( $C_{D,0-}$ ), with 5% mass fraction, shows no significant burst release besides that expected from its drug particle size. However, it is not clear why there would be significant differences in burst release among the other formulations that all have 15% particle loading. The stochastic nature of the percolation process for volume fractions below the percolation threshold is not a sufficient explanation, as the variations between samples within a formulation are extremely limited.

To investigate this further, confocal fluorescence microscopy (CFM) images were taken of the rod cross-sections to probe the distribution of the spray-dried FITC-dextran particles within the rods. Figure 6.7 shows a detail of a cross-section of the reference sample (A). The spray-dried particles appear fairly spherical, and many are clearly hollow, corresponding to observations made for spray-dried mAb and Fabs in Chapter 3 (Figure 3.2). The fact that the particles are hollow means that the volume fraction of the particles in the rods can be significantly higher than their mass fraction, even accounting for density differences. Consequently, formulations might be closer to the percolation threshold than expected from the reported mass fractions used for

drug loading. Overall, while particle loading is high, the particles are well-dispersed and no clear large clusters or network are evident, which can be more clearly seen from the binary image inset in Figure 6.7.

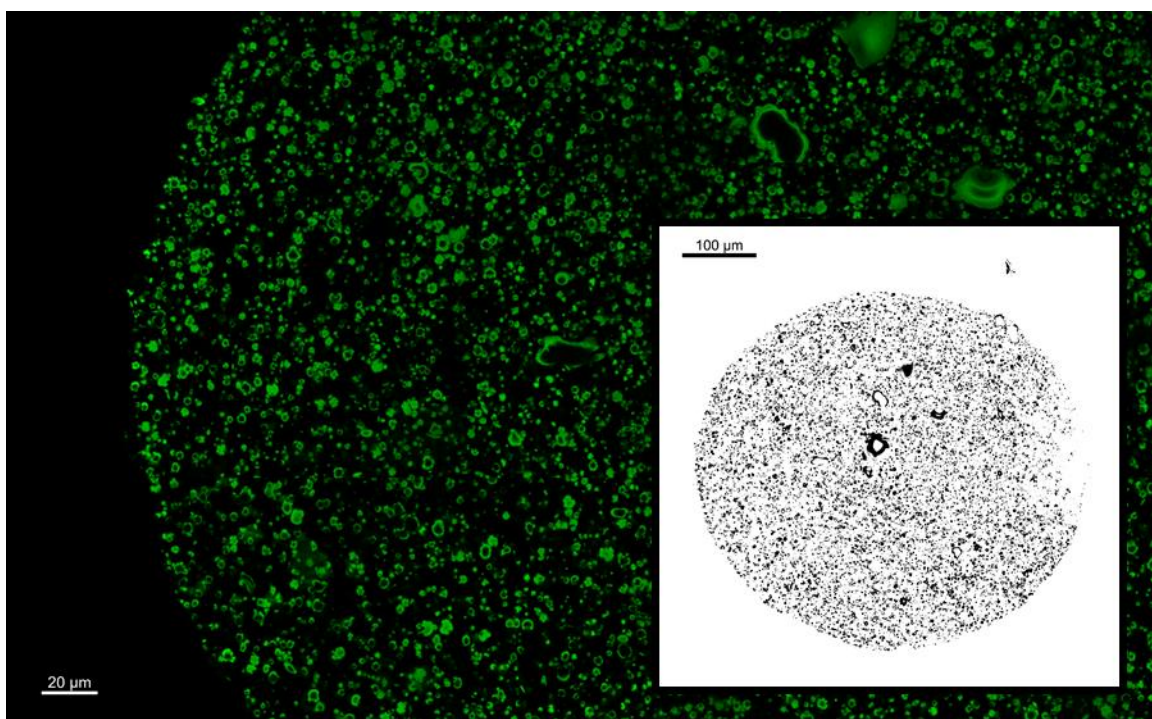


Figure 6.7: Detail of a CFM cross-section of the reference formulation (A), showing the distribution of spray-dried FITC-dextran particles. The inset shows a binary transformation of the whole cross-section used to determine the particle fraction, where black represents the particles.

Cross-sectional images of all the formulations are compared in Figure 6.8. Note that the overall image intensities cannot be directly compared among the different images. While formulation E ( $C_{D,0-}$ ) shows the expected decrease in particle density and formulation F ( $C_{D,0+}$ ) an increase with particularly high densities at the

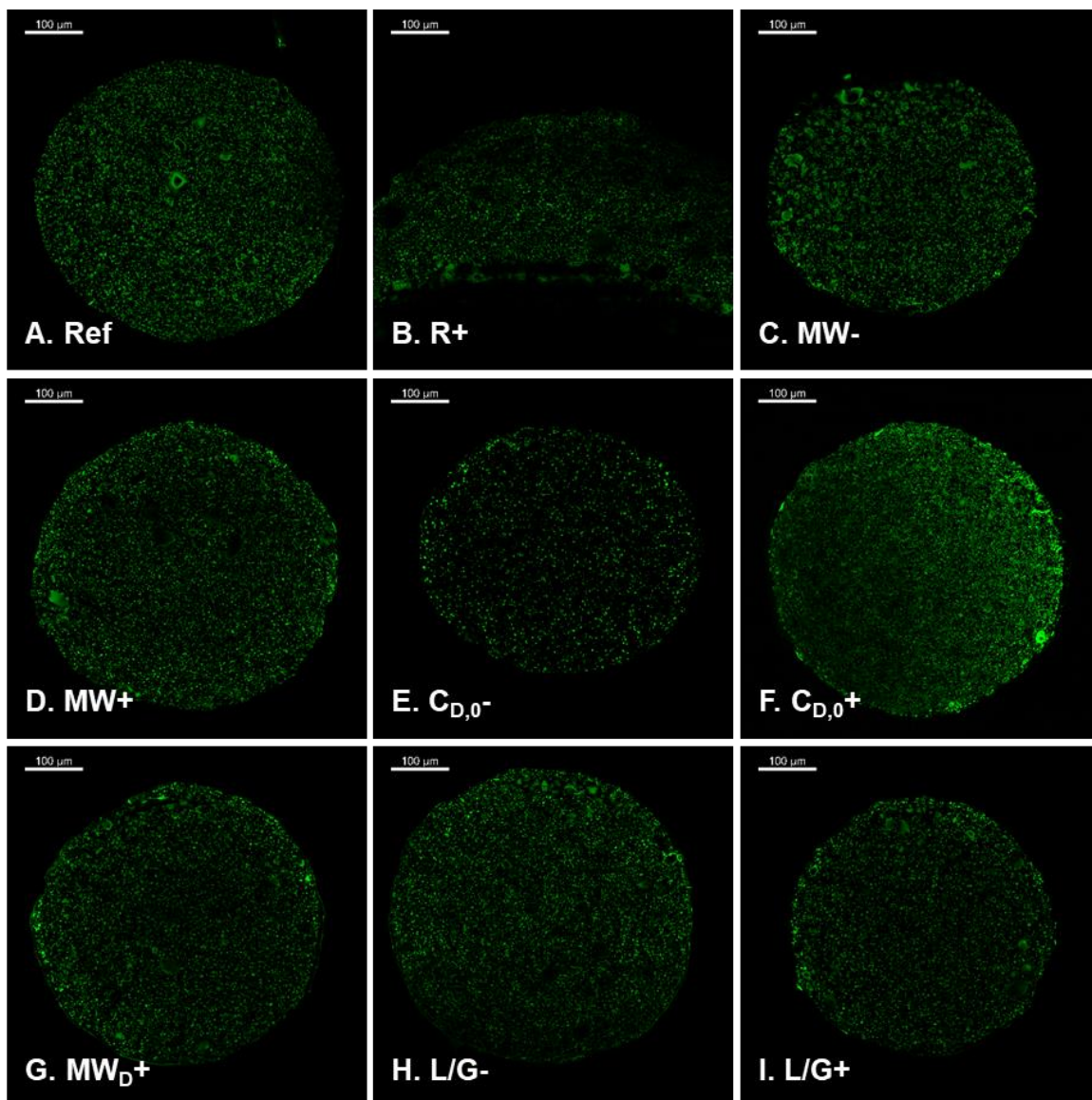


Figure 6.8: Comparison between FITC-dextran particle distributions in the nine rod formulations at Day 0. For formulation B, the lower section of the rod is out of focus.

rod edges, all other formulations are similar to the reference formulation, with homogeneous particle distributions. Note that areas that appear faded in Figure 6.8 are generally out of focus and are not areas with lower particle densities. Binary

transformations of the cross-sectional images, like the inset in Figure 6.7, were analyzed with Fiji to calculate the apparent volume fraction of particles in the rods for each of the formulations [138]. Note that these volume fractions do not take the hollow nature of the spray-dried particles into account, so that the actual volume fractions might be even higher than those reported here. The volume fractions are compared to the amount of first-phase release in Figure 6.9. Although all formulations besides E and F are designed to have 15% loading, there is some spread in the loadings determined from the cross-sectional images. Interestingly, the drug loading seems to be correlated to the amount of first-phase release, supporting the percolation hypothesis. However, the PLGA grade affects this relationship, with the formulations with acid end groups (C and I) showing no significant burst release and the formulation with higher initial molecular weight (D) showing relatively high burst release. Consequently, while the first-phase release might be explained to some extent by percolation within the rods, there are additional factors that affect this release.

Additional cross-sectional images obtained after 7 weeks of release, when the release profiles had reached a plateau, are compared to the images from Day 0 for the three formulations with varying drug loading (A, E, and F) in Figure 6.10. While the absolute intensities among images cannot be directly compared, the images at Week 7 show distinct differences in particle intensity within the image, indicating regions where the drug had been depleted. Formulation F ( $C_{D,0+}$ ) is particularly affected, as expected from the fact that it had released almost 100% at Week 7. It is remarkable that even faded particles seem to retain their shape, which implies that particles do not fully dissolve, and that the local polymer morphology remains fairly intact upon drug release.

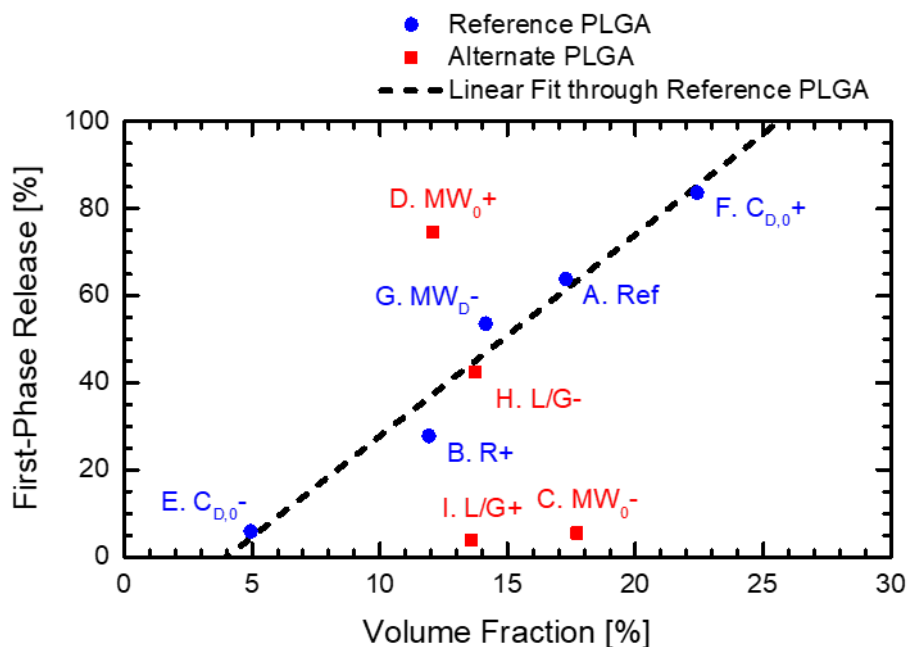


Figure 6.9: Relation between the particle volume fraction, as measured from the cross-sectional images, and the amount of first-phase release for the nine rod formulations. Note that the volume fraction here does not take into account the fact that most particles are hollow. The formulations using the same PLGA grade as the reference formulation are shown by blue circles, while formulations using other PLGA grades are shown by red squares.

The rod radii show significant increases after seven weeks, which is hypothesized to be caused by swelling due to water uptake. Moreover, macroscopic pores are observed after seven weeks, as indicated by the blue dotted boxes in Figure 6.10. These pores can be clearly observed in Figure 6.11, which shows maximum-intensity projections of z-direction image stacks of 10  $\mu\text{m}$  thick cross-sections of the reference formulation (A) at Day 0 and Week 7. Note the homogeneous intensity distribution at Day 0, while intensity differences and faded particles are apparent at

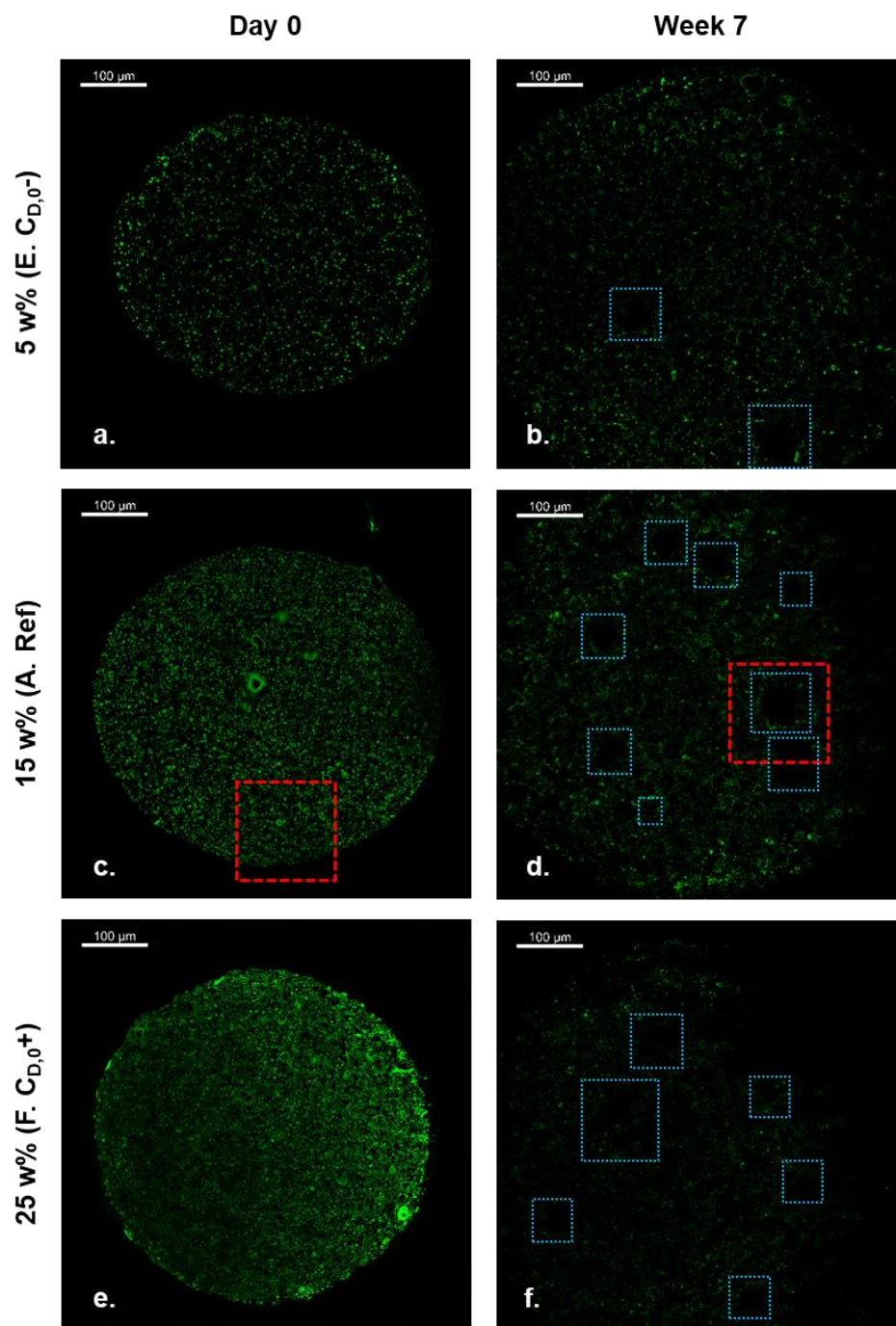


Figure 6.10: Comparison among particle distributions in the formulations with different amounts of drug loading. The blue dotted boxes indicate the presence of macroscopic pores in the rods, while the red dashed boxes show the positions of the images in Figure 6.11.

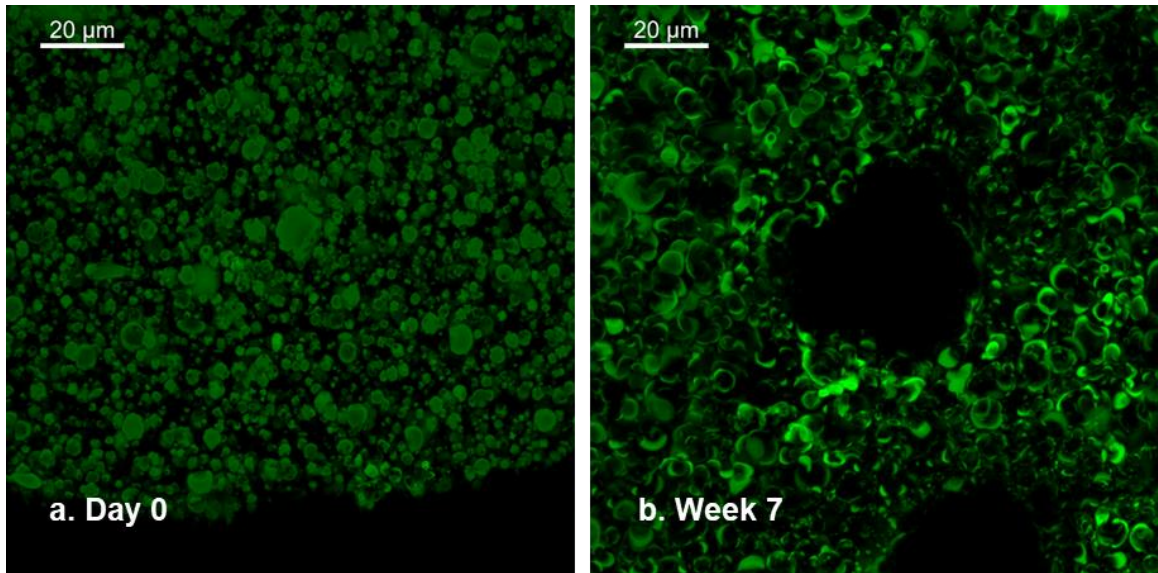


Figure 6.11: Comparison between the maximum-intensity projections of the particle distribution in the reference formulation (A) at Day 0 and Week 7.

Week 7. The pores appear throughout the rods and are much more common in the 15 and 25% formulations (A and F), indicating that their formation might be promoted by higher particle loadings. However, we hypothesize that these pores are formed mainly due to the uptake of water and the swelling of the rods. As water uptake occurs fairly rapidly in these rods, the formation of these pores will lead to a large amount of additional (internal) surface area within the particles from which drug can diffuse rapidly, particularly if limited particle percolation already exists within the rods. Different PLGA grades might not be as susceptible to this pore formation, limiting the amount of first-phase release. Additional images of the other formulations and at earlier times can support this alternate hypothesis.

### 6.3.5 Capturing First-Phase Release

Based on the previous observations, the model parameters can be adapted to take these effects into account. Table 6.6 shows modified model parameters, including changes to the initial polymer MWs and polymer degradation rate constants to correspond to those experimentally determined. The first-phase release is simulated by the model through an increase in the occlusion radius, which can consequently be interpreted as a penetration length into the particle of a network that allows rapid drug release or, similarly, a normalized volume of the rod that is accessible by the formation of system-spanning water pores. For the formulations that show no significant burst release (C, E, and I), this parameter is around 5  $\mu\text{m}$ , the size of the spray-dried particles, while for the percolated formulation F, the occlusion radius spans practically the entire cross-section of the rod.

As elucidated from the PTA fits to the solvent depot data in the previous chapter, a strong correlation exists between the drug diffusivity and the polymer MW at release during parameter estimation (Table 5.4). By measuring the PDI of the polymer, the MW at release can be estimated from the polymer MW SD at release (Equation 6.1), allowing independent determination of the two parameters. The expected MW at release as determined from the SD is approximately 20 kDa, significantly higher than that first estimated from correlations in the literature (Table 6.6) [121]. Consequently, new values for the drug diffusivity are determined to capture the drug release profiles, with separate values for the formulations that reached complete release (Figure 6.5) and the formulations that did not (Figure 6.6), to mitigate the lack of a porosity factor in the equation for burst release due to the occlusion radius (Equation 5.5). Note that the modified drug diffusivities are more than an order of magnitude lower than those initially determined (Table 6.5).

Table 6.6: Modified model parameter values to capture first-phase release and differences in PLGA grade in the nine rod formulations. Bold values in red indicate variations from the initial values in Table 6.5.

Parameter	Units	Formulations								
		A. Ref	B. R+	C. MW <sub>0-</sub>	D. MW <sub>0+</sub>	E. C <sub>D,0-</sub>	F. C <sub>D,0+</sub>	G. MW <sub>D-</sub>	H. L/G-	I. L/G+
Drug diffusivity	$\left[10^{-15} \frac{\text{m}^2}{\text{s}}\right]$	<b>2.36</b>	<b>2.36</b>	<b>5.91</b>	<b>2.36</b>	<b>2.36</b>	<b>5.91</b>	<b>2.36</b>	<b>5.91</b>	<b>5.91</b>
Initial drug concentration	[kg/m <sup>3</sup> ]	195	195	195	195	65	325	195	195	195
Water diffusivity	$\left[10^{-14} \frac{\text{m}^2}{\text{s}}\right]$	5.00	5.00	5.00	5.00	5.00	5.00	5.00	5.00	5.00
Maximum water concentration	[kg/m <sup>3</sup> ]	650	650	650	650	650	650	650	650	650
Occlusion radius	[μm]	<b>71.9</b>	<b>51.4</b>	<b>5.26</b>	<b>91.5</b>	<b>4.97</b>	<b>201</b>	<b>56.3</b>	<b>80.9</b>	<b>4.44</b>
System radius	[10 <sup>-3</sup> m]	0.25	0.50	0.25	0.25	0.25	0.25	0.25	0.25	0.25
Initial polymer MW	[Da]	<b>63000</b>	<b>63000</b>	<b>42000</b>	<b>100000</b>	<b>63000</b>	<b>63000</b>	<b>63000</b>	<b>67000</b>	<b>50000</b>
Polymer MW at release	[Da]	<b>20000</b>	<b>20000</b>	<b>20000</b>	<b>20000</b>	<b>20000</b>	<b>20000</b>	<b>20000</b>	<b>20000</b>	<b>20000</b>
Polymer degradation rate constant	$\left[\frac{10^{-10}}{\text{s}(\text{kg}/\text{m}^3)}\right]$	<b>1.28</b>	<b>1.28</b>	<b>5.76</b>	<b>1.28</b>	<b>1.28</b>	<b>1.28</b>	<b>1.28</b>	<b>7.06</b>	<b>2.98</b>
Polymer MW SD at release	[Da]	10000	10000	10000	10000	10000	10000	10000	10000	10000

The model results with these modified parameters are shown in the red solid lines in Figures 6.5 and 6.6, and capture the experimental data well. With a shared set of model parameters, which are varied only to acknowledge physical differences among the formulations, the model is capable of describing most of the features of the drug release and average MW profiles of all the formulations, some of them quite intricate. Notice in particular how the model anticipates the double, early shoulder in formulation H (L/G-); follows the extended release profile of formulation I (L/G+)

exactly; and predicts the onset of second-phase release in formulations A (Ref) and B (R+).

A few discrepancies between the model and the experimental results are still clear. For example, the model predicts the onset of second-phase release in formulation E but this is absent in the experimental system, indicating that certain effects related to drug loading are still not fully incorporated within the model. In addition to the fact that high loading leads to fast release due to pore formation and percolation, in the opposite limit of low loading, drug release is suppressed relative to what is predicted by the model. Nonetheless, the model performs remarkably well in predicting these complex release profiles observed for a totally independent experimental system *a priori*, and as such, is validated as a design tool. Upon inclusion of certain unexpected factors, the refined model accurately captures the observed release behavior across a broad range of systems. Consequently, the underlying physical mechanisms that constitute the model appear to be sufficiently representative of the *in vitro* system and the model is validated to be used on similar systems, given incorporation of the lessons learned here.

#### **6.4 Conclusions**

A mathematical model for drug release from literature was used in conjunction with a parallel tempering algorithm (PTA) to predict the drug release behavior from two distinct model systems *a priori*: solvent depots composed of mixed PLGA polymers and solid PLGA rods. The former system highlights the potential of the mathematical model to aid in the development of novel formulations: a desirable linear release profile was obtained experimentally by creating solvent depots from mixtures of PLGA polymers with different molecular weights, a design inspired by

parameter estimates from model-and-PTA fits to the theoretical profile. For the latter system, model predictions were compared to experimental formulations of FITC-labeled dextran, a model surrogate for biopharmaceutical drugs, in PLGA rods with a broad range of varying parameters. While the model was capable of predicting the release for several model formulations, it did not take into account effects related to significant first-phase drug release observed in other formulations. Supported by cross-sectional images of the drug distribution within the rods, this unexpected release was attributed to a combination of factors: (1) percolation of the drug particles, (2) swelling and pore formation due to water uptake, and (3) the specific chemistry of the PLGA polymer. These observations indicate the importance of careful selection of the PLGA polymer grade when designing drug release systems. Adapting model parameters, without modifying the model itself, enabled accurate fitting of the experimental data for all formulations, highlighting the wide applicability of the model.

## Chapter 7

### CONCLUSIONS AND RECOMMENDATIONS

“A conclusion is the place where you got tired thinking.”

Martin H. Fischer - *Encore: A Continuing Anthology* (March 1945)

In this dissertation, novel methodologies were developed and used to enable the investigation of a range of biopharmaceutical dense protein systems in three key areas of biopharmaceutical processing: separations, formulation, and drug delivery. As a result, the dissertation has provided the first quantitative measurements of the multiscale structure in a variety of dense protein systems, resulting in new insights into the behavior of these systems in applications relevant for biopharmaceutical development. This chapter is structured similarly to the dissertation’s aims in Section 1.4, with the conclusions and recommendations for each of the three key areas discussed consecutively, where the recommendations always follow the conclusions in a separate paragraph.

In separations, the use of small-angle neutron scattering (SANS) to characterize chromatographic resins has provided a new perspective on the architecture of these resins and the protein distribution within, with the observation of characteristic length scales on the order of nanometers. Observed features are smaller than those observed previously by electron microscopy techniques [34,36], indicating

that these techniques suffer from insufficient resolution or significant structural changes during sample processing. Furthermore, based on our results, we hypothesize that crowding of large proteins in highly cross-linked chromatographic resins may be entropically favored due to depletion or excluded-volume forces, instead of solely size-exclusion effects. Such entropic effects have been demonstrated previously to lead to specific ordering of colloid-polymer systems [70–72], but have not been associated with the partitioning of proteins in materials such as these chromatographic resins.

As compared to our previous work on a cellulose-based resin [42], the investigation of the agarose-based resins has provided critical new insights into their distinct architecture. Naturally, the extension of this methodology to other resins with different architectures, for example those with tentacular, grafted polymer modifications, ceramic base matrices, or protein A ligands could prove to be of particular interest [29,30,142]. Besides the study of commercially-available, established resins, the systematic study of specifically designed resins can further enrich our understanding of the influence of certain material parameters on the protein distribution, with the goal of engineering novel, high-performance resins. The SANS methodology can also be applied to alternative, exploratory purification processes like membrane chromatography, flocculation, and charged ultrafiltration [143]. As the architecture of the resins is expected to affect not only the protein distribution, but also the protein transport behavior, the use of dynamic neutron scattering techniques such as neutron spin echo (NSE) to characterize the nanoscale protein diffusion within these materials would also be an interesting topic of future investigation.

With regard to formulation, novel methodologies based on confocal fluorescence microscopy (CFM) and SANS were combined to characterize the distribution of biotherapeutics in solid-state formulations and to show that there is no direct connection between the static microstructure on either particle or protein length scales and the degree of protein degradation in the form of irreversible aggregation. While process conditions can have a significant effect on the particle-scale protein distribution, protein distributions are similar on the molecular scale. SANS is capable of detecting the formation of reversibly self-associated aggregates in solid-state formulations, possibly in the form of protein dimers. As these reversible aggregates dissociate after reconstitution, their presence in the solid state does not lead directly to the formation of irreversible aggregates in solution. Moreover, our findings suggest that irreversible protein aggregation does not occur in the solid state but occurs upon reconstitution of solid-state formulations.

The characterization in this dissertation was limited to initially stable solid-state formulations, which all included sufficient amounts of excipient. The characterization of formulations with low amounts of stabilizers would be of interest in future work, as it would allow verification of the presence of protein clusters and their effect on long-term protein stability. Due to limitations of the vapor cell, the solid-state formulations were exposed to humidity levels that led to plasticization of the solid-state material. The development of a more advanced vapor cell with controllable humidity would allow the study of the effect of humidity levels below the limit that leads to plasticization. In addition, a higher temperature range limit of the vapor cell would allow *in situ* characterization of microstructural changes during accelerated stability studies at high temperatures around and above the glass transition

temperature of the solid matrix. With a more advanced vapor cell, VC-SANS can aid in understanding the fundamental mechanisms of why fast protein dynamics are good predictors of long-term stability. This is possible because VC-SANS combines aspects of both solid-state hydrogen-deuterium exchange with mass spectrometry (ssHDX-MS) and neutron backscattering (NB), two techniques that have demonstrated correlations between long-term formulation stability and molecular dynamics [22,102–106].

In the area of drug delivery, meta-data obtained from the parallel tempering algorithm (PTA) for parameter estimation allow quantitative evaluation of a particular's model suitability to describe a certain experimental data set. The practical methodology can support rational decision-making on (1) the selection and development of predictive models and (2) experiment and formulation design. The methodology was used to adapt and validate a predictive model for the release of biopharmaceuticals from PLGA sustained-release systems. A custom, desirable zeroth-order release profile was replicated in an experimental solvent depot system designed based on model calculations. Moreover, the model was capable of predicting the degradation kinetics and drug release of a specifically designed experimental PLGA solid rod system remarkably well. However, model predictions did not incorporate significant first-phase release, which was observed for certain experimental formulations. This release is hypothesized to be caused by structural changes in the rod morphology during water uptake, based on observations of rod swelling and macroscopic pore formation.

Future investigation of these effects using the techniques presented in this dissertation, particularly during the first few days of drug release, when the first-phase

release occurs, is warranted. Depending on the validation of these effects, the model can be adapted to incorporate these processes as part of other suggested model improvements, such as (1) modifications to the concept of an inclusion radius to account for macroscopic pore formation and percolation, (2) the incorporation of an effective drug diffusivity during the first-phase release to account for the porosity, and (3) extension of the model to account for multicomponent PLGA blends. The latter is particularly important in the design of the linear drug release profiles, as the PLGA blends required to achieve such a linear profile are currently modeled as a single polymer with a large molecular weight polydispersity. PLGA rod studies in this work were limited to using a surrogate drug in the form of fluorescently labeled dextran. Future investigations should compare our findings with those for biotherapeutics such as monoclonal antibodies, for example a model drug such as the NISTmAb [144–146].

In general, this dissertation highlights the broad range of phenomena that can influence dense protein systems, and emphasizes the value in bringing soft matter expertise to this field to better understand these systems. The tools and methods developed in this dissertation, including small-angle neutron scattering, confocal fluorescence microscopy, and mathematical modeling, will be invaluable in the study of the structure-function relationship of these and other dense protein systems throughout the biopharmaceutical field.

## BIBLIOGRAPHY

- [1] S.N. Cohen, DNA cloning: A personal view after 40 years, *Proc. Natl. Acad. Sci.* 110 (2013) 15521–15529. doi:10.1073/pnas.1313397110.
- [2] E. Russo, The birth of biotechnology, *Nature*. 421 (2003) 456–7. doi:10.1038/nj6921-456a.
- [3] S.N. Cohen, A.C.Y. Chang, H.W. Boyer, R.B. Helling, Construction of Biologically Functional Bacterial Plasmids In Vitro, *Proc. Natl. Acad. Sci.* 70 (1973) 3240–3244. doi:10.1073/pnas.70.11.3240.
- [4] A.C.Y. Chang, S.N. Cohen, Genome Construction Between Bacterial Species In Vitro: Replication and Expression of Staphylococcus Plasmid Genes in *Escherichia coli*, *Proc. Natl. Acad. Sci.* 71 (1974) 1030–1034. doi:10.1073/pnas.71.4.1030.
- [5] J.F. Morrow, S.N. Cohen, A.C.Y. Chang, H.W. Boyer, H.M. Goodman, R.B. Helling, Replication and Transcription of Eukaryotic DNA in *Escherichia coli*, *Proc. Natl. Acad. Sci.* 71 (1974) 1743–1747. doi:10.1073/pnas.71.5.1743.
- [6] U. Gottschalk, K. Brorson, A.A. Shukla, Innovation in biomanufacturing: the only way forward, *Pharm. Bioprocess.* 1 (2013) 141–157. doi:10.4155/pbp.13.17.
- [7] S. Mitragotri, P.A. Burke, R. Langer, Overcoming the challenges in administering biopharmaceuticals: formulation and delivery strategies, *Nat. Rev. Drug Discov.* 13 (2014) 655–672. doi:10.1038/nrd4363.
- [8] G. Walsh, Biopharmaceutical benchmarks 2014, *Nat. Biotechnol.* 32 (2014) 992–1000. doi:10.1038/nbt.3040.
- [9] E. Moorkens, N. Meuwissen, I. Huys, P. Declerck, A.G. Vulto, S. Simoons, The Market of Biopharmaceutical Medicines: A Snapshot of a Diverse Industrial Landscape, *Front. Pharmacol.* 8 (2017). doi:10.3389/fphar.2017.00314.
- [10] M. Pohlscheidt, R. Kiss, U. Gottschalk, An Introduction to „Recent Trends in

the Biotechnology Industry: Development and Manufacturing of Recombinant Antibodies and Proteins“, in: *Adv. Biochem. Eng. Biotechnol.*, 2018: pp. 127–141. doi:10.1007/10\_2017\_39.

- [11] U. Gottschalk, K. Brorson, A.A. Shukla, The need for innovation in biomanufacturing, *Nat. Biotechnol.* 30 (2012) 489–92. doi:10.1038/nbt.2263.
- [12] D.M. Ecker, S.D. Jones, H.L. Levine, The therapeutic monoclonal antibody market, *MAbs.* 7 (2015) 9–14. doi:10.4161/19420862.2015.989042.
- [13] A.L. Daugherty, R.J. Mersny, Formulation and delivery issues for monoclonal antibody therapeutics, *Adv. Drug Deliv. Rev.* 58 (2006) 686–706. doi:10.1016/j.addr.2006.03.011.
- [14] H. Kaplon, J.M. Reichert, Antibodies to watch in 2018, *MAbs.* 10 (2018) 183–203. doi:10.1080/19420862.2018.1415671.
- [15] M. Suzuki, C. Kato, A. Kato, Therapeutic antibodies: their mechanisms of action and the pathological findings they induce in toxicity studies, *J. Toxicol. Pathol.* 28 (2015) 133–139. doi:10.1293/tox.2015-0031.
- [16] C.J. Roberts, Protein aggregation and its impact on product quality, *Curr. Opin. Biotechnol.* 30 (2014) 211–217. doi:10.1016/j.copbio.2014.08.001.
- [17] H.J. Lee, A. McAuley, K.F. Schilke, J. McGuire, Molecular origins of surfactant-mediated stabilization of protein drugs, *Adv. Drug Deliv. Rev.* 63 (2011) 1160–1171. doi:10.1016/j.addr.2011.06.015.
- [18] D.G. Greene, The formation and structure of precipitated protein phases, University of Delaware, 2016.
- [19] P.G. Vekilov, Dense Liquid Precursor for the Nucleation of Ordered Solid Phases from Solution, *Cryst. Growth Des.* 4 (2004) 671–685. doi:10.1021/cg049977w.
- [20] T.M. Przybycien, N.S. Pujar, L.M. Steele, Alternative bioseparation operations: life beyond packed-bed chromatography., *Curr. Opin. Biotechnol.* 15 (2004) 469–78. doi:10.1016/j.copbio.2004.08.008.
- [21] N. Hammerschmidt, B. Hintersteiner, N. Lingg, A. Jungbauer, Continuous precipitation of IgG from CHO cell culture supernatant in a tubular reactor, *Biotechnol. J.* 10 (2015) 1196–1205. doi:10.1002/biot.201400608.
- [22] M.T. Cicerone, M.J. Pikal, K.K. Qian, Stabilization of proteins in solid form,

- Adv. Drug Deliv. Rev. 93 (2015) 14–24. doi:10.1016/j.addr.2015.05.006.
- [23] J.M. Angelo, A.M. Lenhoff, Determinants of protein elution rates from preparative ion-exchange adsorbents, *J. Chromatogr. A*. 1440 (2016) 94–104. doi:10.1016/j.chroma.2016.02.048.
- [24] M.E.M. Cromwell, E. Hilario, F. Jacobson, Protein aggregation and bioprocessing., *AAPS J.* 8 (2006) E572–E579. doi:10.1208/aapsj080366.
- [25] S.H.S. Koshari, N.J. Wagner, A.M. Lenhoff, Effects of Resin Architecture and Protein Size on Nanoscale Protein Distribution in Ion-Exchange Media, *Langmuir*. 34 (2018) 673–684. doi:10.1021/acs.langmuir.7b03289.
- [26] J. Thömmes, Investigations on protein adsorption to agarose-dextran composite media, *Biotechnol. Bioeng.* 62 (1999) 358–362. doi:10.1002/(SICI)1097-0290(19990205)62:3<358::AID-BIT12>3.0.CO;2-9.
- [27] C.L. Cooper, P.L. Dubin, A.B. Kayitmazer, S. Turksen, Polyelectrolyte–protein complexes, *Curr. Opin. Colloid Interface Sci.* 10 (2005) 52–78. doi:10.1016/j.cocis.2005.05.007.
- [28] H.-O. Johansson, J.M. Van Alstine, Modeling of Protein Interactions with Surface-Grafted Charged Polymers. Correlations between Statistical Molecular Modeling and a Mean Field Approach, *Langmuir*. 22 (2006) 8920–8930. doi:10.1021/la060941a.
- [29] A.M. Lenhoff, Protein adsorption and transport in polymer-functionalized ion-exchangers, *J. Chromatogr. A*. 1218 (2011) 8748–8759. doi:10.1016/j.chroma.2011.06.061.
- [30] E. Müller, Properties and Characterization of High Capacity Resins for Biochromatography, *Chem. Eng. Technol.* 28 (2005) 1295–1305. doi:10.1002/ceat.200500161.
- [31] Y. Yao, A.M. Lenhoff, Pore size distributions of ion exchangers and relation to protein binding capacity, *J. Chromatogr. A*. 1126 (2006) 107–119. doi:10.1016/j.chroma.2006.06.057.
- [32] B.D. Bowes, H. Koku, K.J. Czymmek, A.M. Lenhoff, Protein adsorption and transport in dextran-modified ion-exchange media. I: Adsorption., *J. Chromatogr. A*. 1216 (2009) 7774–84. doi:10.1016/j.chroma.2009.09.014.
- [33] B.D. Bowes, A.M. Lenhoff, Protein adsorption and transport in dextran-modified ion-exchange media. III. Effects of resin charge density and dextran

- content on adsorption and intraparticle uptake, *J. Chromatogr. A.* 1218 (2011) 7180–7188. doi:10.1016/j.chroma.2011.08.039.
- [34] H. Koku, *Microstructure-based analysis and simulation of flow and mass transfer in chromatographic stationary phases*, University of Delaware, 2011.
- [35] J.M. Angelo, A. Cvetkovic, R. Gantier, A.M. Lenhoff, Characterization of cross-linked cellulosic ion-exchange adsorbents: 1. Structural properties, *J. Chromatogr. A.* 1319 (2013) 46–56. doi:10.1016/j.chroma.2013.10.003.
- [36] J.M. Angelo, A. Cvetkovic, R. Gantier, A.M. Lenhoff, Characterization of cross-linked cellulosic ion-exchange adsorbents: 2. Protein sorption and transport, *J. Chromatogr. A.* 1438 (2016) 100–112. doi:10.1016/j.chroma.2016.02.019.
- [37] R. Hahn, Methods for characterization of biochromatography media, *J. Sep. Sci.* 35 (2012) 3001–3032. doi:10.1002/jssc.201200770.
- [38] Y. Yao, A.M. Lenhoff, Determination of pore size distributions of porous chromatographic adsorbents by inverse size-exclusion chromatography, *J. Chromatogr. A.* 1037 (2004) 273–282. doi:10.1016/j.chroma.2004.02.054.
- [39] Y. Tao, G. Carta, G. Ferreira, D. Robbins, Adsorption of deamidated antibody variants on macroporous and dextran-grafted cation exchangers: I. Adsorption equilibrium, *J. Chromatogr. A.* 1218 (2011) 1519–1529. doi:10.1016/j.chroma.2011.01.049.
- [40] A.R. Ubiera, G. Carta, Radiotracer measurements of protein mass transfer: Kinetics in ion exchange media, *Biotechnol. J.* 1 (2006) 665–674. doi:10.1002/biot.200600023.
- [41] P. DePhillips, A.M. Lenhoff, Pore size distributions of cation-exchange adsorbents determined by inverse size-exclusion chromatography, *J. Chromatogr. A.* 883 (2000) 39–54. doi:10.1016/S0021-9673(00)00420-9.
- [42] S.H.S. Koshari, N.J. Wagner, A.M. Lenhoff, Characterization of lysozyme adsorption in cellulosic chromatographic materials using small-angle neutron scattering, *J. Chromatogr. A.* 1399 (2015) 45–52. doi:10.1016/j.chroma.2015.04.042.
- [43] S. Krueger, A.P. Andrews, R. Nossal, Small angle neutron scattering studies of structural characteristics of agarose gels, *Biophys. Chem.* 53 (1994) 85–94. doi:10.1016/0301-4622(94)00079-4.

- [44] D.I. Svergun, M.H.J. Koch, Small-angle scattering studies of biological macromolecules in solution, *Reports Prog. Phys.* 66 (2003) 1735–1782. doi:10.1088/0034-4885/66/10/R05.
- [45] I. Grillo, Small-Angle Neutron Scattering and Applications in Soft Condensed Matter, in: R. Borsali, R. Pecora (Eds.), *Soft-Matter Charact.*, LXXII, Springer Netherlands, Dordrecht, 2008: pp. 723–782. doi:10.1007/978-1-4020-4465-6\_13.
- [46] B. Hammouda, *Probing Nanoscale Structures - The SANS Toolbox*, Gaithersburg, MD, 2010. [http://www.ncnr.nist.gov/staff/hammouda/the\\_SANS\\_toolbox.pdf](http://www.ncnr.nist.gov/staff/hammouda/the_SANS_toolbox.pdf).
- [47] D.S. Sivia, *Elementary Scattering Theory*, First ed., Oxford University Press, New York, 2011.
- [48] S.H.S. Koshari, *Characterization of Lysozyme Adsorption in Cellulosic Chromatographic Materials Using Small-Angle Neutron Scattering*, University of Delaware, 2014.
- [49] B.D. Bowes, S.J. Traylor, S.M. Timmick, K.J. Czymmek, A.M. Lenhoff, Insights into Protein Sorption and Desorption on Dextran-Modified Ion-Exchange Media, *Chem. Eng. Technol.* 35 (2012) 91–101. doi:10.1002/ceat.201100304.
- [50] C. Harinarayan, J. Mueller, A. Ljunglöf, R. Fahrner, J. Van Alstine, R. van Reis, An exclusion mechanism in ion exchange chromatography, *Biotechnol. Bioeng.* 95 (2006) 775–787. doi:10.1002/bit.21080.
- [51] M.M. Castellanos, A. McAuley, J.E. Curtis, Investigating Structure and Dynamics of Proteins in Amorphous Phases Using Neutron Scattering, *Comput. Struct. Biotechnol. J.* 15 (2017) 117–130. doi:10.1016/j.csbj.2016.12.004.
- [52] C.J. Glinka, J.G. Barker, B. Hammouda, S. Krueger, J.J. Moyer, W.J. Orts, The 30 m Small-Angle Neutron Scattering Instruments at the National Institute of Standards and Technology, *J. Appl. Crystallogr.* 31 (1998) 430–445. doi:10.1107/S0021889897017020.
- [53] S.R. Kline, Reduction and analysis of SANS and USANS data using IGOR Pro, *J. Appl. Crystallogr.* 39 (2006) 895–900. doi:10.1107/S0021889806035059.
- [54] B. Hammouda, A new Guinier–Porod model, *J. Appl. Crystallogr.* 43 (2010) 716–719. doi:10.1107/S0021889810015773.

- [55] A. Guinier, G. Fournet, *Small-Angle Scattering of X-rays*, First Edit, John Wiley and Sons, New York, 1955.
- [56] D.I. Svergun, S. Richard, M.H.J. Koch, Z. Sayers, S. Kuprin, G. Zaccai, Protein hydration in solution: Experimental observation by x-ray and neutron scattering, *Proc. Natl. Acad. Sci.* 95 (1998) 2267–2272. doi:10.1073/pnas.95.5.2267.
- [57] H.M. Berman, J. Westbrook, Z. Feng, G. Gilliland, T.N. Bhat, H. Weissig, I.N. Shindyalov, P.E. Bourne, The Protein Data Bank, *Nucleic Acids Res.* 28 (2000) 235–242. [www.rcsb.org](http://www.rcsb.org).
- [58] R. Diamond, Real-space refinement of the structure of hen egg-white lysozyme, *J. Mol. Biol.* 82 (1974) 371–391. doi:10.1016/0022-2836(74)90598-1.
- [59] E.A.J. Thomassen, H.A. van Veen, P.H.C. van Berkel, J.H. Nuijens, J.P. Abrahams, The protein structure of recombinant human lactoferrin produced in the milk of transgenic cows closely matches the structure of human milk-derived lactoferrin., *Transgenic Res.* 14 (2005) 397–405. doi:10.2210/pdb2bjj/pdb.
- [60] L.J. Harris, S.B. Larson, K.W. Hasel, A. McPherson, Refined structure of an intact IgG2a monoclonal antibody., *Biochemistry.* 36 (1997) 1581–97. doi:10.1021/bi962514+.
- [61] V.F. Sears, Neutron scattering lengths and cross sections, *Neutron News.* 3 (1992) 26–37. doi:10.1080/10448639208218770.
- [62] P. Kienzle, Neutron activation and scattering calculator, NIST Cent. Neutron Res. (2014). <http://www.ncnr.nist.gov/resources/activation/>.
- [63] D. Svergun, C. Barberato, M. Koch, CRY SOL - a Program to Evaluate X-ray Solution Scattering of Biological Macromolecules from Atomic Coordinates, *J. Appl. Crystallogr.* 28 (1995) 768–773. <http://scripts.iucr.org/cgi-bin/paper?li5001> (accessed January 23, 2014).
- [64] S. Arnott, A. Fulmer, W.E. Scott, I.C.M. Dea, R. Moorhouse, D.A. Rees, The agarose double helix and its function in agarose gel structure, *J. Mol. Biol.* 90 (1974) 269–284. doi:10.1016/0022-2836(74)90372-6.
- [65] S.A. Foord, E.D.Y. Atkins, New x-ray diffraction results from agarose: Extended single helix structures and implications for gelation mechanism, *Biopolymers.* 28 (1989) 1345–1365. doi:10.1002/bip.360280802.

- [66] S.E. Schafer, E.S. Stevens, A Reexamination of the Double-helix model for agarose gels using optical rotation, *Biopolymers*. 36 (1995) 103–108.
- [67] J.-M. Guenet, C. Rochas, Agarose Sols and Gels Revisited, *Macromol. Symp.* 242 (2006) 65–70. doi:10.1002/masy.200651011.
- [68] A. Amsterdam, Z. Er-El, S. Shaltiel, Ultrastructure of beaded agarose, *Arch. Biochem. Biophys.* 171 (1975) 673–677. doi:10.1016/0003-9861(75)90079-X.
- [69] A.G. Ogston, The spaces in a uniform random suspension of fibres, *Trans. Faraday Soc.* 54 (1958) 1754. doi:10.1039/tf9585401754.
- [70] M. Adams, Z. Dogic, S.L. Keller, S. Fraden, Entropically driven microphase transitions in mixtures of colloidal rods and spheres, *Nature*. 393 (1998) 349–352. doi:10.1038/30700.
- [71] Z. Dogic, S. Fraden, Ordered phases of filamentous viruses, *Curr. Opin. Colloid Interface Sci.* 11 (2006) 47–55. doi:10.1016/j.cocis.2005.10.004.
- [72] H.-X. Zhou, G. Rivas, A.P. Minton, Macromolecular Crowding and Confinement: Biochemical, Biophysical, and Potential Physiological Consequences, *Annu. Rev. Biophys.* 37 (2008) 375–397. doi:10.1146/annurev.biophys.37.032807.125817.
- [73] J.E. Curtis, H. Nanda, S. Khodadadi, M. Cicerone, H.J. Lee, A. McAuley, S. Krueger, Small-angle neutron scattering study of protein crowding in liquid and solid phases: lysozyme in aqueous solution, frozen solution, and carbohydrate powders, *J. Phys. Chem. B.* 116 (2012) 9653–67. doi:10.1021/jp304772d.
- [74] M.M. Castellanos, N.J. Clark, M.C. Watson, S. Krueger, A. McAuley, J.E. Curtis, Role of Molecular Flexibility and Colloidal Descriptions of Proteins in Crowded Environments from Small-Angle Scattering, *J. Phys. Chem. B.* 120 (2016) 12511–12518. doi:10.1021/acs.jpcc.6b10637.
- [75] W.L. DeLano, *The PyMOL Molecular Graphics System*, (2002). <http://www.pymol.org>.
- [76] J.M. Angelo, *Mechanisms underlying protein sorption and transport within polysaccharide-based stationary phases for ion-exchange chromatography*, University of Delaware, 2016.
- [77] S.H.S. Koshari, J.L. Ross, P.K. Nayak, I.E. Zarraga, K. Rajagopal, N.J. Wagner, A.M. Lenhoff, Characterization of Protein–Excipient Microheterogeneity in Biopharmaceutical Solid-State Formulations by

Confocal Fluorescence Microscopy, *Mol. Pharm.* 14 (2017) 546–553.  
doi:10.1021/acs.molpharmaceut.6b00940.

- [78] A.M. Abdul-Fattah, V. Truong-Le, L. Yee, L. Nguyen, D.S. Kalonia, M.T. Cicerone, M.J. Pikal, Drying-induced variations in physico-chemical properties of amorphous pharmaceuticals and their impact on stability (I): Stability of a monoclonal antibody, *J. Pharm. Sci.* 96 (2007) 1983–2008.  
doi:10.1002/jps.20859.
- [79] M.J. Pikal, D. Rigsbee, M.L. Roy, D. Galreath, K.J. Kovach, B. (Stuart) Wang, J.F. Carpenter, M.T. Cicerone, Solid state chemistry of proteins: II. The correlation of storage stability of freeze-dried human growth hormone (hGH) with structure and dynamics in the glassy solid, *J. Pharm. Sci.* 97 (2008) 5106–5121. doi:10.1002/jps.21374.
- [80] J. Park, K. Nagapudi, C. Vergara, R. Ramachander, J.S. Laurence, S. Krishnan, Effect of pH and Excipients on Structure, Dynamics, and Long-Term Stability of a Model IgG1 Monoclonal Antibody upon Freeze-Drying, *Pharm. Res.* 30 (2013) 968–984. doi:10.1007/s11095-012-0933-z.
- [81] B. Gikanga, R. Turok, a. Hui, M. Bowen, O.B. Stauch, Y.-F. Maa, Manufacturing of High-Concentration Monoclonal Antibody Formulations via Spray Drying--the Road to Manufacturing Scale, *PDA J. Pharm. Sci. Technol.* 69 (2015) 59–73. doi:10.5731/pdajpst.2015.01003.
- [82] D. Devineni, C. Gonschorek, M.T. Cicerone, Y. Xu, J.F. Carpenter, T.W. Randolph, Storage stability of keratinocyte growth factor-2 in lyophilized formulations: Effects of formulation physical properties and protein fraction at the solid-air interface., *Eur. J. Pharm. Biopharm.* 88 (2014) 332–41.  
doi:10.1016/j.ejpb.2014.05.012.
- [83] Y. Xu, P. Grobelny, A. Von Allmen, K. Knudson, M. Pikal, J.F. Carpenter, T.W. Randolph, Protein quantity on the air-solid interface determines degradation rates of human growth hormone in lyophilized samples, *J. Pharm. Sci.* 103 (2014) 1356–1366. doi:10.1002/jps.23926.
- [84] T.W. Patapoff, O. Esue, Polysorbate 20 prevents the precipitation of a monoclonal antibody during shear, *Pharm. Dev. Technol.* 14 (2009) 659–664.
- [85] V. Ragoonanan, A. Aksan, Heterogeneity in desiccated solutions: implications for biostabilization., *Biophys. J.* 94 (2008) 2212–27.  
doi:10.1529/biophysj.107.110684.
- [86] A. Millqvist-Fureby, M. Malmsten, B. Bergenståhl, Surface characterisation of

- freeze-dried protein/carbohydrate mixtures, *Int. J. Pharm.* 191 (1999) 103–114. doi:10.1016/S0378-5173(99)00285-9.
- [87] A. Millqvist-Fureby, M. Malmsten, B. Bergenståhl, Spray-drying of trypsin - Surface characterisation and activity preservation, *Int. J. Pharm.* 188 (1999) 243–253. doi:10.1016/S0378-5173(99)00226-4.
- [88] M. Adler, M. Unger, G. Lee, Surface composition of spray-dried particles of bovine serum albumin/trehalose/surfactant, *Pharm. Res.* 17 (2000) 863–870. doi:10.1023/A:1007568511399.
- [89] M. Bowen, N. Armstrong, Y.-F. Maa, Investigating high-concentration monoclonal antibody powder suspension in nonaqueous suspension vehicles for subcutaneous injection., *J. Pharm. Sci.* 101 (2012) 4433–43. doi:10.1002/jps.23324.
- [90] M. Bowen, R. Turok, Y.-F. Maa, Spray Drying of Monoclonal Antibodies: Investigating Powder-Based Biologic Drug Substance Bulk Storage, *Dry. Technol.* 31 (2013) 1441–1450. doi:10.1080/07373937.2013.796968.
- [91] D.P. Chang, V.K. Garripelli, J. Rea, R. Kelley, K. Rajagopal, Investigation of Fragment Antibody Stability and Its Release Mechanism from Poly(Lactide-co-Glycolide)-Triacetin Depots for Sustained-Release Applications, *J. Pharm. Sci.* 104 (2015) 3404–3417. doi:10.1002/jps.24546.
- [92] J. Dong, A. Hubel, J.C. Bischof, A. Aksan, Freezing-induced phase separation and spatial microheterogeneity in protein solutions., *J. Phys. Chem. B.* 113 (2009) 10081–7. doi:10.1021/jp809710d.
- [93] A.M. Padilla, M.J. Pikal, The study of phase separation in amorphous freeze-dried systems, part 2: Investigation of raman mapping as a tool for studying amorphous phase separation in freeze-dried protein formulations, *J. Pharm. Sci.* 100 (2011) 1467–1474. doi:10.1002/jps.22380.
- [94] J. Clauss, K. Schmidt-Rohr, H.W. Spiess, Determination of domain sizes in heterogeneous polymers by solid-state NMR, *Acta Polym.* 44 (1993) 1–17. doi:10.1002/actp.1993.010440101.
- [95] N. Panchuk-Voloshina, R.P. Haugland, J. Bishop-Stewart, M.K. Bhalgat, P.J. Millard, F. Mao, W.Y. Leung, R.P. Haugland, Alexa dyes, a series of new fluorescent dyes that yield exceptionally bright, photostable conjugates., *J. Histochem. Cytochem.* 47 (1999) 1179–1188. doi:10.1177/002215549904700910.

- [96] R. Vehring, W.R. Foss, D. Lechuga-Ballesteros, Particle formation in spray drying, *J. Aerosol Sci.* 38 (2007) 728–746. doi:10.1016/j.jaerosci.2007.04.005.
- [97] C.S. Handscomb, M. Kraft, Simulating the structural evolution of droplets following shell formation, *Chem. Eng. Sci.* 65 (2010) 713–725. doi:10.1016/j.ces.2009.09.025.
- [98] J. Bahadur, D. Sen, S. Mazumder, S. Bhattacharya, H. Frielinghaus, G. Goerigk, Origin of buckling phenomenon during drying of micrometer-sized colloidal droplets, *Langmuir*. 27 (2011) 8404–14. doi:10.1021/la200827n.
- [99] G.L. Lin, J.A. Pathak, D.H. Kim, M. Carlson, V. Riguero, Y.J. Kim, J.S. Buff, G.G. Fuller, Interfacial dilatational deformation accelerates particle formation in monoclonal antibody solutions, *Soft Matter*. 12 (2016) 3293–3302. doi:10.1039/C5SM02830B.
- [100] S.H.S. Koshari, P.K. Nayak, S. Burra, I.E. Zarraga, K. Rajagopal, Y. Liu, N.J. Wagner, A.M. Lenhoff, In situ characterization of the microstructural evolution of biopharmaceutical solid-state formulations with implications for protein stability, *Mol. Pharm.* Submitted (2018).
- [101] M.A. Mensink, H.W. Frijlink, K. van der Voort Maarschalk, W.L.J. Hinrichs, How sugars protect proteins in the solid state and during drying (review): Mechanisms of stabilization in relation to stress conditions, *Eur. J. Pharm. Biopharm.* 114 (2017) 288–295. doi:10.1016/j.ejpb.2017.01.024.
- [102] B.S. Moorthy, I.E. Zarraga, L. Kumar, B.T. Walters, P. Goldbach, E.M. Topp, A. Allmendinger, Solid-State Hydrogen–Deuterium Exchange Mass Spectrometry: Correlation of Deuterium Uptake and Long-Term Stability of Lyophilized Monoclonal Antibody Formulations, *Mol. Pharm.* 15 (2018) 1–11. doi:10.1021/acs.molpharmaceut.7b00504.
- [103] A.M. Sophocleous, J. Zhang, E.M. Topp, Localized hydration in lyophilized myoglobin by hydrogen-deuterium exchange mass spectrometry. 1. Exchange mapping, *Mol. Pharm.* 9 (2012) 718–26. doi:10.1021/mp3000088.
- [104] B.S. Moorthy, S.G. Schultz, S.G. Kim, E.M. Topp, Predicting protein aggregation during storage in lyophilized solids using solid state amide hydrogen/deuterium exchange with mass spectrometric analysis (ssHDX-MS), *Mol. Pharm.* 11 (2014) 1869–79. doi:10.1021/mp500005v.
- [105] K.K. Qian, P.J. Grobelny, M. Tyagi, M.T. Cicerone, Using the Fluorescence Red Edge Effect to Assess the Long-Term Stability of Lyophilized Protein Formulations, *Mol. Pharm.* 12 (2015) 1141–1149. doi:10.1021/mp500641f.

- [106] B. Wang, S. Tchessalov, M.T. Cicerone, N.W. Warne, M.J. Pikal, Impact of sucrose level on storage stability of proteins in freeze-dried solids: II. Correlation of aggregation rate with protein structure and molecular mobility, *J. Pharm. Sci.* 98 (2009) 3145–3166. doi:10.1002/jps.21622.
- [107] C.K. Shelton, R.L. Jones, J.A. Dura, T.H. Epps, Tracking Solvent Distribution in Block Polymer Thin Films during Solvent Vapor Annealing with in Situ Neutron Scattering, *Macromolecules.* 49 (2016) 7525–7534. doi:10.1021/acs.macromol.6b02046.
- [108] E.J. Yearley, P.D. Godfrin, T. Perevozchikova, H. Zhang, P. Falus, L. Porcar, M. Nagao, J.E. Curtis, P. Gawande, R. Taing, I.E. Zarraga, N.J. Wagner, Y. Liu, Observation of small cluster formation in concentrated monoclonal antibody solutions and its implications to solution viscosity, *Biophys. J.* 106 (2014) 1763–70. doi:10.1016/j.bpj.2014.02.036.
- [109] L.R. Winther, J. Qvist, B. Halle, Hydration and Mobility of Trehalose in Aqueous Solution, *J. Phys. Chem. B.* 116 (2012) 9196–9207. doi:10.1021/jp304982c.
- [110] A.M. Sophocleous, E.M. Topp, Localized hydration in lyophilized myoglobin by hydrogen-deuterium exchange mass spectrometry. 2. Exchange kinetics, *Mol. Pharm.* 9 (2012) 727–33. doi:10.1021/mp2004093.
- [111] H.K. Makadia, S.J. Siegel, Poly Lactic-co-Glycolic Acid (PLGA) as Biodegradable Controlled Drug Delivery Carrier, *Polymers (Basel).* 3 (2011) 1377–1397. doi:10.3390/polym3031377.
- [112] G. Tiwari, R. Tiwari, S. Bannerjee, L. Bhati, S. Pandey, P. Pandey, B. Sriwastawa, Drug delivery systems: An updated review, *Int. J. Pharm. Investig.* 2 (2012) 2. doi:10.4103/2230-973X.96920.
- [113] S. Fredenberg, M. Wahlgren, M. Reslow, A. Axelsson, The mechanisms of drug release in poly(lactic-co-glycolic acid)-based drug delivery systems--a review., *Int. J. Pharm.* 415 (2011) 34–52. doi:10.1016/j.ijpharm.2011.05.049.
- [114] T. Casalini, F. Rossi, S. Lazzari, G. Perale, M. Masi, Mathematical modeling of PLGA microparticles: From polymer degradation to drug release, *Mol. Pharm.* 11 (2014) 4036–4048. doi:10.1021/mp500078u.
- [115] C. Raman, A.J. McHugh, A model for drug release from fast phase inverting injectable solutions, *J. Control. Release.* 102 (2005) 145–157. doi:10.1016/j.jconrel.2004.09.022.

- [116] J. Siepmann, K. Elkharraz, F. Siepmann, D. Klose, How Autocatalysis Accelerates Drug Release from PLGA-Based Microparticles: A Quantitative Treatment, *Biomacromolecules*. 6 (2005) 2312–2319. doi:10.1021/bm050228k.
- [117] A.N. Ford Versypt, D.W. Pack, R.D. Braatz, Mathematical modeling of drug delivery from autocatalytically degradable PLGA microspheres - A review, *J. Control. Release*. 165 (2013) 29–37. doi:10.1016/j.jconrel.2012.10.015.
- [118] S.N. Rothstein, S.R. Little, A “tool box” for rational design of degradable controlled release formulations, *J. Mater. Chem.* 21 (2011) 29–39. doi:10.1039/C0JM01668C.
- [119] Y. Xu, C.S. Kim, D.M. Saylor, D. Koo, Polymer degradation and drug delivery in PLGA-based drug-polymer applications: A review of experiments and theories, *J. Biomed. Mater. Res. - Part B Appl. Biomater.* (2016) 1692–1716. doi:10.1002/jbm.b.33648.
- [120] M.J. Armstrong, A.N. Beris, N.J. Wagner, An adaptive parallel tempering method for the dynamic data-driven parameter estimation of nonlinear models, *AIChE J.* 63 (2017) 1937–1958. doi:10.1002/aic.15577.
- [121] S.N. Rothstein, W.J. Federspiel, S.R. Little, A simple model framework for the prediction of controlled release from bulk eroding polymer matrices, *J. Mater. Chem.* 18 (2008) 1873. doi:10.1039/b718277e.
- [122] S.N. Rothstein, W.J. Federspiel, S.R. Little, A unified mathematical model for the prediction of controlled release from surface and bulk eroding polymer matrices, *Biomaterials*. 30 (2009) 1657–1664. doi:10.1016/j.biomaterials.2008.12.002.
- [123] T.D. Knab, S.R. Little, R.S. Parker, A systems approach to modeling drug release from polymer microspheres to accelerate in vitro to in vivo translation, *J. Control. Release*. 211 (2015) 74–84. doi:10.1016/j.jconrel.2015.04.045.
- [124] G. Jiang, B.H. Woo, F. Kang, J. Singh, P.P. DeLuca, Assessment of protein release kinetics, stability and protein polymer interaction of lysozyme encapsulated poly(D,L-lactide-co-glycolide) microspheres, *J. Control. Release*. 79 (2002) 137–145. doi:10.1016/S0168-3659(01)00533-8.
- [125] K. Rajagopal, J. Wood, B. Tran, T.W. Patapoff, T. Nivaggioli, Trehalose Limits BSA Aggregation in Spray-Dried Formulations at High Temperatures: Implications in Preparing Polymer Implants for Long-Term Protein Delivery, *J. Pharm. Sci.* 102 (2013) 2655–2666. doi:10.1002/jps.23634.

- [126] L. Lu, S.J. Peter, M. D. Lyman, H.-L. Lai, S.M. Leite, J.A. Tamada, S. Uyama, J.P. Vacanti, Robert Langer, A.G. Mikos, In vitro and in vivo degradation of porous poly(dl-lactic-co-glycolic acid) foams, *Biomaterials*. 21 (2000) 1837–1845. doi:10.1016/S0142-9612(00)00047-8.
- [127] L. Lu, C.A. Garcia, A.G. Mikos, In vitro degradation of thin poly(DL-lactic-co-glycolic acid) films, *J. Biomed. Mater. Res.* 46 (1999) 236–244. doi:10.1002/(SICI)1097-4636(199908)46:2<236::AID-JBM13>3.0.CO;2-F.
- [128] M.G. Kendall, *The Advanced Theory of Statistics*, 4th Ed., Macmillan, 1979.
- [129] S.S. Lee, P. Hughes, A.D. Ross, M.R. Robinson, Biodegradable implants for sustained drug release in the eye, *Pharm. Res.* 27 (2010) 2043–2053. doi:10.1007/s11095-010-0159-x.
- [130] A. Patel, T. Ansari, P. Vimal, M. Goyani, A. Deshmukh, B. Akbari, A Review on PLGA Based Solvent Induced In-situ Forming Implant, *Inventi*. 2015 (2015).
- [131] D.N. Kapoor, A. Bhatia, R. Kaur, R. Sharma, G. Kaur, S. Dhawan, PLGA: a unique polymer for drug delivery, *Ther. Deliv.* 6 (2015) 41–58. doi:10.4155/tde.14.91.
- [132] X. Huang, C.S. Brazel, On the importance and mechanisms of burst release in matrix-controlled drug delivery systems, *J. Control. Release.* 73 (2001) 121–136. doi:10.1016/S0168-3659(01)00248-6.
- [133] R.A. Jain, The manufacturing techniques of various drug loaded biodegradable poly(lactide-co-glycolide) (PLGA) devices, *Biomaterials*. 21 (2000) 2475–2490. doi:10.1016/S0142-9612(00)00115-0.
- [134] J. Siepman, F. Siepman, Modeling of diffusion controlled drug delivery, *J. Control. Release.* 161 (2012) 351–362. doi:10.1016/j.jconrel.2011.10.006.
- [135] A.N. Ford, D.W. Pack, R.D. Braatz, Multi-Scale Modeling of PLGA Microparticle Drug Delivery Systems, in: *Comput. Aided Chem. Eng.*, 2011: pp. 1475–1479. doi:10.1016/B978-0-444-54298-4.50074-X.
- [136] K.J. Brodbeck, S. Pushpala, A.J. McHugh, Sustained release of human growth hormone from PLGA solution depots, *Pharm. Res.* 16 (1999) 1825–9. doi:10.1023/A:1018943107688.
- [137] S.S. Rane, P. Choi, Polydispersity Index: How Accurately Does It Measure the Breadth of the Molecular Weight Distribution?, *Chem. Mater.* 17 (2005) 926–

926. doi:10.1021/cm048594i.

- [138] J. Schindelin, I. Arganda-Carreras, E. Frise, V. Kaynig, M. Longair, T. Pietzsch, S. Preibisch, C. Rueden, S. Saalfeld, B. Schmid, J.-Y. Tinevez, D.J. White, V. Hartenstein, K. Eliceiri, P. Tomancak, A. Cardona, Fiji: an open-source platform for biological-image analysis, *Nat. Methods*. 9 (2012) 676–682. doi:10.1038/nmeth.2019.
- [139] M.D. Rintoul, S. Torquato, Precise determination of the critical threshold and exponents in a three-dimensional continuum percolation model, *J. Phys. A: Math. Gen.* 30 (1997) L585–L592. doi:10.1088/0305-4470/30/16/005.
- [140] R.M. Ziff, S. Torquato, Percolation of disordered jammed sphere packings, *J. Phys. A: Math. Theor.* 50 (2017) 085001. doi:10.1088/1751-8121/aa5664.
- [141] T. Ehtezazi, C. Washington, Controlled release of macromolecules from PLA microspheres: using porous structure topology, *J. Control. Release*. 68 (2000) 361–372. doi:10.1016/S0168-3659(00)00270-4.
- [142] S. Hober, K. Nord, M. Linhult, Protein A chromatography for antibody purification, *J. Chromatogr. B*. 848 (2007) 40–47. doi:10.1016/j.jchromb.2006.09.030.
- [143] J. Thömmes, M. Etzel, Alternatives to chromatographic separations., *Biotechnol. Prog.* 23 (2007) 42–5. doi:10.1021/bp0603661.
- [144] M.M. Castellanos, K. Mattison, S. Krueger, J.E. Curtis, Characterization of the NISTmAb Reference Material using small-angle scattering and molecular simulation - Part II: Concentrated protein solutions, *Anal. Bioanal. Chem.* 410 (2018) 2161–2171. doi:10.1007/s00216-018-0869-1.
- [145] M.M. Castellanos, S.C. Howell, D.T. Gallagher, J.E. Curtis, Characterization of the NISTmAb Reference Material using small-angle scattering and molecular simulation, *Anal. Bioanal. Chem.* 410 (2018) 2141–2159. doi:10.1007/s00216-018-0868-2.
- [146] J.E. Schiel, A. Turner, T. Mouchahoir, K. Yandrowski, S. Telikepalli, J. King, P. DeRose, D. Ripple, K. Phinney, The NISTmAb Reference Material 8671 value assignment, homogeneity, and stability, *Anal. Bioanal. Chem.* 410 (2018) 2127–2139. doi:10.1007/s00216-017-0800-1.
- [147] E. Mylonas, D. Svergun, Accuracy of molecular mass determination of proteins in solution by small-angle X-ray scattering, *J. Appl. Crystallogr.* 40 (2007) s245–s249. <http://scripts.iucr.org/cgi-bin/paper?sm6016> (accessed January 14,

2014).

- [148] T. Creighton, *Proteins: Structures and Molecular Properties*, 2nd ed., W. H. Freeman, New York, 1992.

## Appendix A

### SMALL-ANGLE NEUTRON SCATTERING DATA FOR PROTEIN ADSORPTION ON CHROMATOGRAPHIC RESINS

This appendix contains the scattering patterns and fitting values for each of the 64 investigated resin-protein combinations in Chapter 2, at each total ionic strength. Details of the sample preparation, small-angle neutron scattering (SANS) data collection, and fitting models are included in the main article, but some additional details are elaborated on here. Scattering patterns and model fits for each resin are shown in Figure A.1 through Figure A.2. Corresponding fitting values and ranges are included in Table A.1 through Table A.4.

#### A.1 Selection of Structural Models

The mathematical expressions used to fit the SANS patterns are of the same format as Equation 2.2, but are specifically derived based on certain assumptions about the sample structure, which allows mathematical formulation of the form factor  $P(Q)$  and/or effective structure factor  $S(Q)$  as a function of the structural parameters. Fitting of the experimental scattering patterns to an appropriate model consequently allows determination of these structural parameters.

A wide variety of both empirical and theoretical models was compared to the experimental data to determine which models best capture the architectural features of the resins. The simplest models that were still capable of describing the full scattering patterns were ultimately used for data analysis: (1) the generalized Guinier-Porod

model for the cellulose-based resin and (2) the polydisperse cylinder model for the agarose-based resins.

## **A.2 Model Fitting Ranges in Protein-Laden Resins**

The same structural models used for the neat protein resins still provide good fits to the resins after protein adsorption, indicating that while some structural parameters might change due to protein adsorption, the underlying resin architecture remains the same. However, in the high- $Q$  region, an additional shoulder or peak appears in the scattering pattern due to the presence of protein monomers (Figure A.1 through Figure A.4), similar to what has been observed before in HyperCel-lysozyme systems. Since this contribution is due mainly to the scattering from the inherent protein monomer structure, the structural models cannot capture this scattering feature.

Instead, this region in the scattering pattern was excluded from the structural model fit but directly compared to the expected form factor scattering from the protein monomers. The structural models were still fit to the background scattering and the low- $Q$  region, up to the  $Q$ -value where the protein presence caused an inflection in the scattering pattern, typically around  $0.03 \text{ \AA}^{-1}$ . Specific fitting ranges for each pattern are included in Table A.1 through Table A.4.

## **A.3 Model Parameters in Protein-Laden Resins**

Values for the model parameters are included in Table A.1 through Table A.4. As for the neat HyperCel, no parameters of the generalized Guinier-Porod model were fixed during the fitting process for protein-laden HyperCel, unless otherwise specified. For the polydisperse cylinder model for agarose-based resins, the cylinder length, the volume fraction, and the solvent SLD value were fixed during fitting. As for the neat

agarose-based resins, the cylinder length was fixed at 10000 Å. As the volume fraction and the scattering length density difference are perfectly correlated (Equation 2.9), either the volume fraction or the scattering length densities have to be held fixed during model fitting. As the adsorption of protein can significantly change the SLD of the solid cylinder phase, this parameter was fit to the experimental data. Instead, the cylinder volume fraction was calculated by adding the volume fraction of the neat resin cylinders, obtained from neat resin measurements, to the volume fraction of adsorbed protein, obtained from the amount of adsorbed protein,  $q$  (Equation 2.1). For this calculation, the proteins were assumed to have an average, effective specific volume of 0.74 cm<sup>3</sup>/g (or density of 1.35 g/mL) that is independent of total ionic strength. This specific volume was based on SAXS measurements [147] and tabulated data [148] and was verified for each protein by calculating the aggregated atomic volumes from the respective PDB files listed in Chapter 2, as described by Svergun *et al.* [63]. The SLD of the solvent was calculated for each sample based on the D<sub>2</sub>O:H<sub>2</sub>O ratio in the sample.

#### **A.4 Protein Contribution in Protein-Laden Resins**

The contribution of protein monomers to the scattering pattern at high  $Q$  can be described by a form factor and a structure factor contribution (Equation 2.2). Although this formalism is well-studied in protein solutions, it is more complicated to apply to resin-protein systems. First, while several models exist to describe protein-protein interactions and the resulting structure factor in protein solutions, protein-protein interactions in condensed protein systems are far more challenging to model. Additionally, in the case of proteins adsorbed to resins at extremely high local concentrations, not only protein-protein interactions but also protein-resin interactions

can affect the structure factor. Second, the protein form factor can change from that measured in dilute solution, as the protein structure can change during protein adsorption to the resin.

Consequently, in this work the scattering features at high  $Q$  were directly compared to the expected form factor scattering from the protein monomers, as if they were in dilute solution. All deviations from this behavior were attributed to an effective structure factor, which includes effects of (1) changes to the protein structure due to adsorption, (2) protein-protein interactions due to high local concentrations, and (3) protein-resin interactions. The protein form factor was obtained from the experimental measurements in dilute solution (Figure 2.2) and scaled to the actual protein concentration inside the resins, taking into account both adsorbed protein and protein in solution in the pore and inter-particle space. In addition, the change in SLD of the protein and solvent due to the addition of H<sub>2</sub>O was taken into account.

### **A.5 Low- $Q$ Upturn in Protein-Laden Resins**

Adsorption of larger proteins in HyperCel and Capto shows one additional characteristic scattering feature: at the smallest accessed  $Q$ -values, an upturn can be observed in the scattering pattern (Figure 2.5a). This upturn is indicative of the presence of larger scattering objects outside of the accessible length scales, *i.e.*, they are larger than 1  $\mu\text{m}$ . Hence, lactoferrin and mAb adsorption in HyperCel apparently also leads to a change of the structure on length scales much larger than those characteristic of the pore structure. One hypothesis is that this upturn is caused by the positioning of these proteins in the larger pores of the resin, leading to larger dense areas within the network that do not affect the fractal structure at smaller length scales.

However, as the nature of this change cannot be directly observed by SANS, such hypotheses are preliminary, but they might be verified with techniques such as ultra-small-angle neutron scattering (USANS), which can access smaller  $Q$ -ranges.

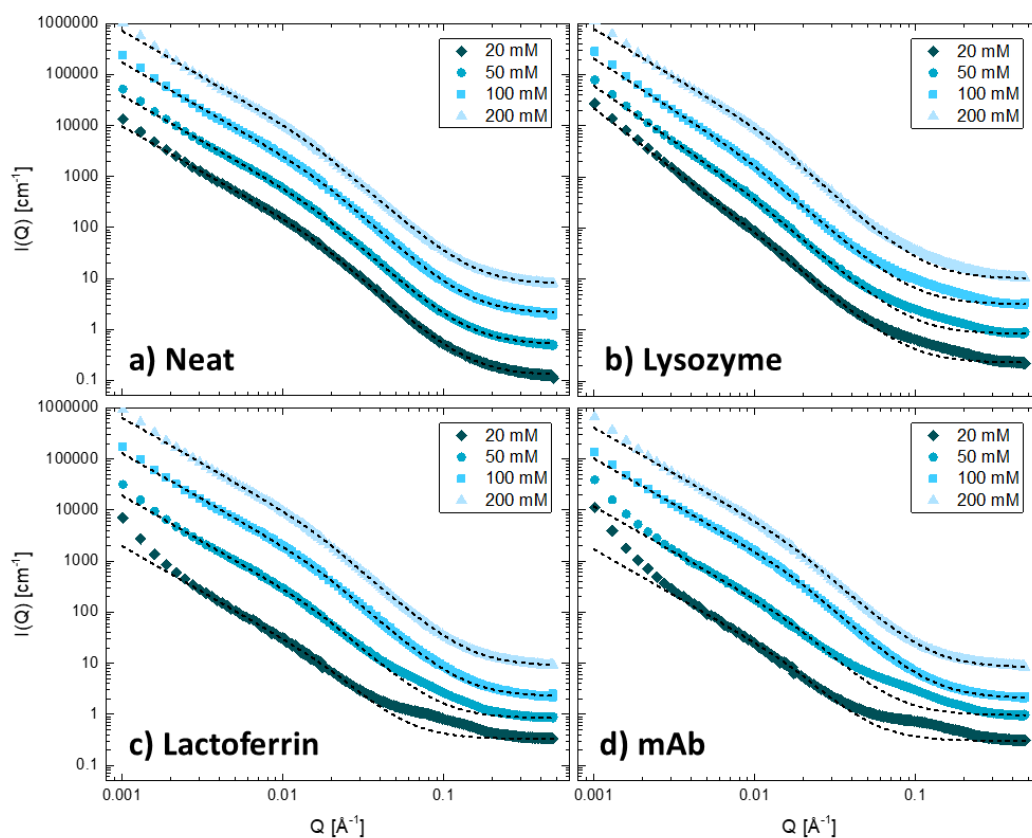


Figure A.1: Scattering patterns of neat and protein-laden S HyperCel. Error bars are generally smaller than the symbol size. Successive curves are offset by a factor of 4. Structural model fits are shown by the dashed lines, and were fit only to the background scattering and the low- $Q$  region, up to the  $Q$ -value where the presence of the protein caused an inflection in the scattering pattern. Specific fitting ranges are included in Table A.1.

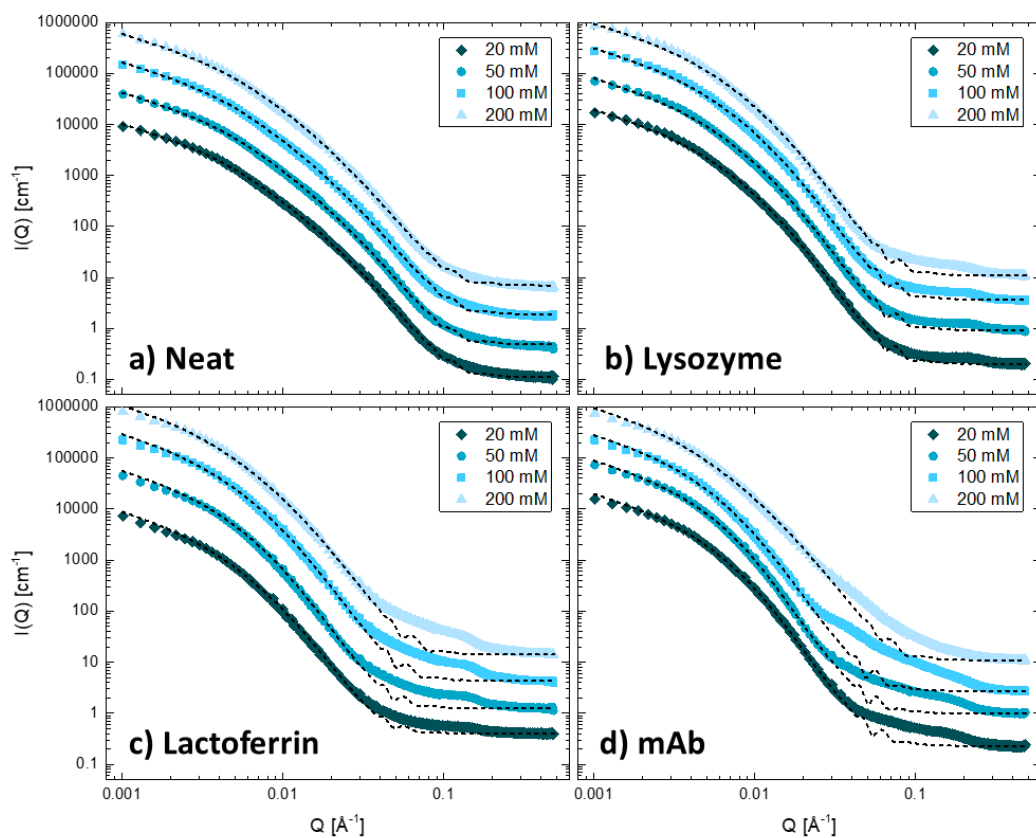


Figure A.2: Scattering patterns of neat and protein-laden SP Sepharose FF. Error bars are generally smaller than the symbol size. Successive curves are offset by a factor of 4. Structural model fits are shown by the dashed lines, and were fit only to the background scattering and the low- $Q$  region, up to the  $Q$ -value where the presence of the protein caused an inflection in the scattering pattern. Specific fitting ranges are included in Table A.2.

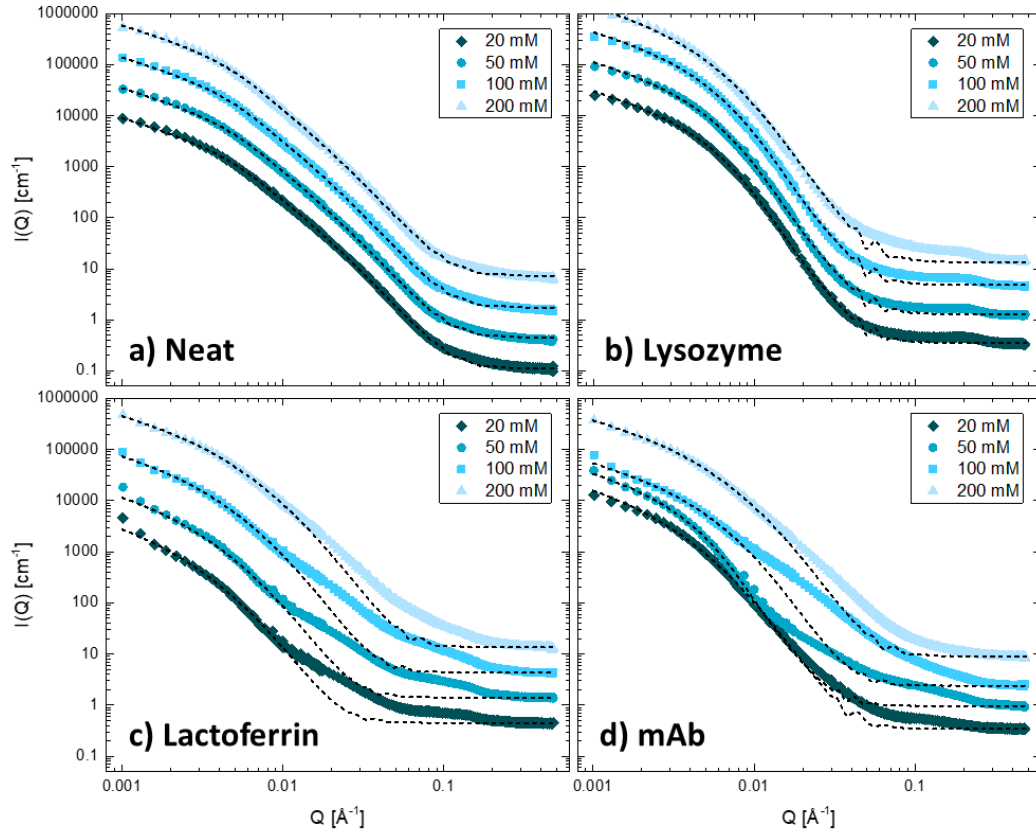


Figure A.3: Scattering patterns of neat and protein-laden SP Sepharose XL. Error bars are generally smaller than the symbol size. Successive curves are offset by a factor of 4. Structural model fits are shown by the dashed lines, and were fit only to the background scattering and the low- $Q$  region, up to the  $Q$ -value where the presence of the protein caused an inflection in the scattering pattern. Specific fitting ranges are included in Table A.3.

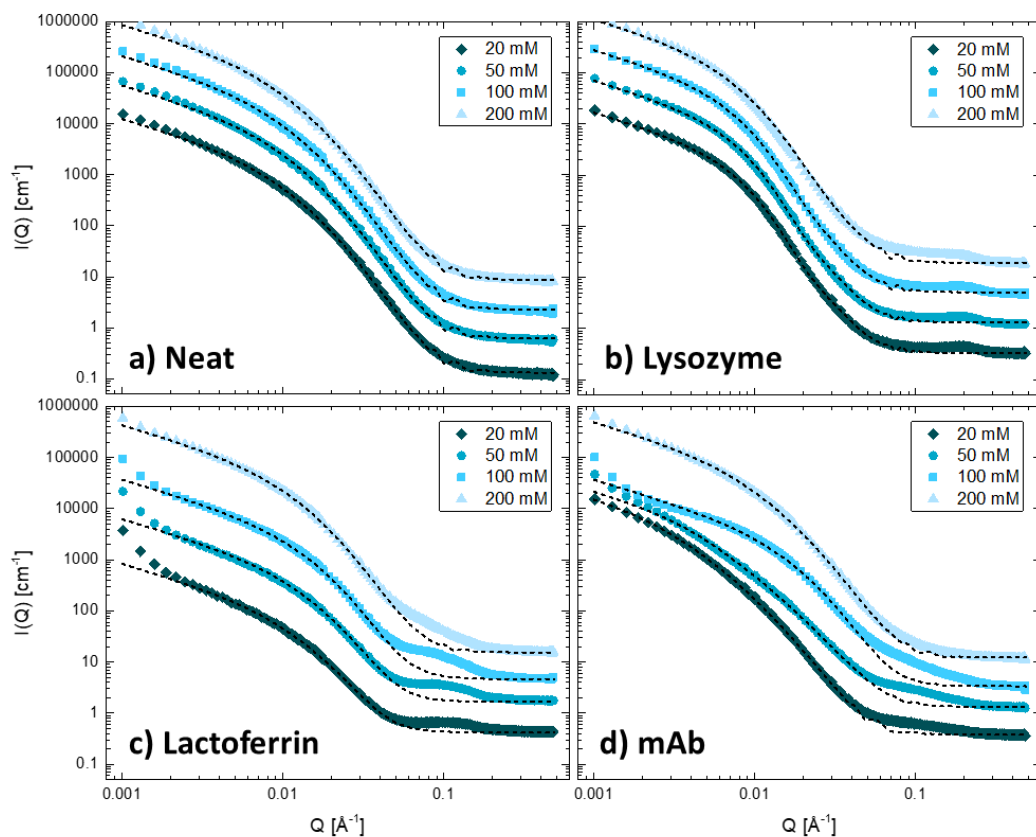


Figure A.4: Scattering patterns of neat and protein-laden Captos. Error bars are generally smaller than the symbol size. Successive curves are offset by a factor of 4. Structural model fits are shown by the dashed lines, and were fit only to the background scattering and the low- $Q$  region, up to the  $Q$ -value where the presence of the protein caused an inflection in the scattering pattern. Specific fitting ranges are included in Table A.4.

Table A.1: Fitting parameters of the generalized Guinier-Porod model and fitting values for neat and protein-laden S HyperCel. Lower and upper limits of the fitting range are also included. Values that were held fixed during fitting are indicated by an asterisk.

	Neat				Lysozyme			
	20 mM	50 mM	100 mM	200 mM	20 mM	50 mM	100 mM	200 mM
Scale $G$ [-]	0.041	0.040	0.040	0.040	0.001	0.005	0.011	0.027
Radius of gyration $R_g$ [Å]	33.9	33.5	32.2	34.3	15.9	35.9	45.4	42.6
Dimension variable $s$ [-]	1.79	1.79	1.81	1.82	2.42	2.17	2.03	1.88
Porod exponent $m$ [-]	2.72	2.72	2.73	2.69	2.65	2.65	2.68	2.78
Background $B$ [cm <sup>-1</sup> ]	0.13	0.13	0.13	0.12	0.23	0.21	0.20	0.16
Lower fitting range* [Å <sup>-1</sup> ]	0.001	0.001	0.001	0.001	0.001	0.001	0.002	0.002
Upper fitting range* [Å <sup>-1</sup> ]	0.5	0.5	0.5	0.5	0.04	0.04	0.04	0.04

	Lactoferrin				mAb			
	20 mM	50 mM	100 mM	200 mM	20 mM	50 mM	100 mM	200 mM
Scale $G$ [-]	0.008	0.019	0.032	0.040	0.007	0.012	0.025	0.025
Radius of gyration $R_g$ [Å]	29.3	33.4	32.8	34.1	34.1	31.2	31.3	33.3
Dimension variable $s^*$ [-]	1.80	1.80	1.80	1.80	1.80	1.80	1.80	1.80
Porod exponent $m^*$ [-]	2.70	2.70	2.70	2.70	2.70	2.70	2.70	2.70
Background $B$ [cm <sup>-1</sup> ]	0.33	0.21	0.14	0.14	0.30	0.24	0.13	0.13
Lower fitting range* [Å <sup>-1</sup> ]	0.003	0.002	0.002	0.002	0.003	0.003	0.002	0.002
Upper fitting range* [Å <sup>-1</sup> ]	0.03	0.03	0.06	0.5	0.03	0.03	0.5	0.5

Table A.2: Fitting parameters of the polydisperse cylinder model and fitting values for neat and protein-laden SP Sepharose FF. Lower and upper limits of the fitting range are also included. Values that were held fixed during fitting are indicated by an asterisk.

	Neat				Lysozyme			
	20 mM	50 mM	100 mM	200 mM	20 mM	50 mM	100 mM	200 mM
Volume fraction $\varphi$ [-]	0.033	0.034	0.033	0.031	0.101*	0.099*	0.093*	0.082*
Mean cylinder radius $R$ [Å]	13.6	13.8	13.8	17.3	72.6	69.3	67.4	64.7
Radial polydispersity $\sigma$ [-]	0.93	0.92	0.93	0.87	0.60	0.61	0.62	0.62
Cylinder length $L^*$ [Å]	10000	10000	10000	10000	10000	10000	10000	10000
SLD cylinder $\rho_{cyl}$ [ $10^{-6} \text{Å}^{-2}$ ]	2.22*	2.22*	2.22*	2.22*	3.51	3.46	3.43	3.60
SLD solvent $\rho_{solv}^*$ [ $10^{-6} \text{Å}^{-2}$ ]	6.33	6.33	6.33	6.33	5.72	5.74	5.77	5.87
Background $B$ [ $\text{cm}^{-1}$ ]	0.11	0.12	0.12	0.11	0.20	0.23	0.23	0.17
Lower fitting range* [Å <sup>-1</sup> ]	0.001	0.001	0.001	0.001	0.001	0.001	0.001	0.001
Upper fitting range* [Å <sup>-1</sup> ]	0.5	0.5	0.5	0.5	0.04	0.04	0.04	0.04

	Lactoferrin				mAb			
	20 mM	50 mM	100 mM	200 mM	20 mM	50 mM	100 mM	200 mM
Volume fraction $\varphi$ [-]	0.113*	0.113*	0.088*	0.077*	0.108*	0.124*	0.098*	0.053*
Mean cylinder radius $R$ [Å]	86.5	108.9	88.4	60.9	118.6	144.5	121.2	43.0
Radial polydispersity $\sigma$ [-]	0.63	0.57	0.62	0.69	0.52	0.48	0.54	0.76
Cylinder length $L^*$ [Å]	10000	10000	10000	10000	10000	10000	10000	10000
SLD cylinder $\rho_{cyl}$ [ $10^{-6} \text{Å}^{-2}$ ]	3.49	3.66	3.66	3.64	3.90	4.19	4.38	3.46
SLD solvent $\rho_{solv}^*$ [ $10^{-6} \text{Å}^{-2}$ ]	4.57	4.98	5.46	5.65	5.61	5.74	5.94	5.96
Background $B$ [ $\text{cm}^{-1}$ ]	0.40	0.31	0.27	0.22	0.23	0.25	0.17	0.17
Lower fitting range* [Å <sup>-1</sup> ]	0.001	0.001	0.001	0.001	0.001	0.001	0.001	0.001
Upper fitting range* [Å <sup>-1</sup> ]	0.03	0.03	0.03	0.03	0.03	0.03	0.02	0.02

Table A.3: Fitting parameters of the polydisperse cylinder model and fitting values for neat and protein-laden SP Sepharose XL. Lower and upper limits of the fitting range are also included. Values that were held fixed during fitting are indicated by an asterisk.

	Neat				Lysozyme			
	20 mM	50 mM	100 mM	200 mM	20 mM	50 mM	100 mM	200 mM
<b>Volume fraction <math>\varphi</math> [-]</b>	0.027	0.025	0.024	0.025	0.129*	0.140*	0.128*	0.103*
<b>Mean cylinder radius <math>R</math> [Å]</b>	3.9	3.2	3.0	2.8	167.4	169.8	161.9	121.9
<b>Radial polydispersity <math>\sigma</math> [-]</b>	1.21	1.26	1.28	1.30	0.47	0.44	0.46	0.54
<b>Cylinder length <math>L^*</math> [Å]</b>	10000	10000	10000	10000	10000	10000	10000	10000
<b>SLD cylinder <math>\rho_{cyl}</math> [<math>10^{-6} \text{Å}^{-2}</math>]</b>	2.22*	2.22*	2.22*	2.22*	3.67	3.87	3.86	3.99
<b>SLD solvent <math>\rho_{solv}^*</math> [<math>10^{-6} \text{Å}^{-2}</math>]</b>	6.33	6.33	6.33	6.33	5.36	5.42	5.48	5.67
<b>Background <math>B</math> [<math>\text{cm}^{-1}</math>]</b>	0.11	0.11	0.11	0.11	0.35	0.32	0.30	0.21
<b>Lower fitting range* [Å<sup>-1</sup>]</b>	0.001	0.001	0.001	0.001	0.001	0.001	0.001	0.001
<b>Upper fitting range* [Å<sup>-1</sup>]</b>	0.5	0.5	0.5	0.5	0.03	0.03	0.03	0.03

	Lactoferrin				mAb			
	20 mM	50 mM	100 mM	200 mM	20 mM	50 mM	100 mM	200 mM
<b>Volume fraction <math>\varphi</math> [-]</b>	0.144*	0.118*	0.082*	0.048*	0.067*	0.126*	0.068*	0.034*
<b>Mean cylinder radius <math>R</math> [Å]</b>	115.2	97.2	83.8	58.1	112.0	251.1	109.5	70.5
<b>Radial polydispersity <math>\sigma</math> [-]</b>	0.66	0.66	0.65	0.67	0.63	0.41	0.54	0.62
<b>Cylinder length <math>L^*</math> [Å]</b>	10000	10000	10000	10000	10000	10000	10000	10000
<b>SLD cylinder <math>\rho_{cyl}</math> [<math>10^{-6} \text{Å}^{-2}</math>]</b>	4.00	4.36	4.42	3.85	3.55	4.80	5.09	3.94
<b>SLD solvent <math>\rho_{solv}^*</math> [<math>10^{-6} \text{Å}^{-2}</math>]</b>	4.37	4.85	5.32	5.72	5.01	5.47	6.00	5.99
<b>Background <math>B</math> [<math>\text{cm}^{-1}</math>]</b>	0.45	0.35	0.27	0.21	0.34	0.24	0.15	0.14
<b>Lower fitting range* [Å<sup>-1</sup>]</b>	0.002	0.002	0.001	0.001	0.001	0.001	0.001	0.001
<b>Upper fitting range* [Å<sup>-1</sup>]</b>	0.01	0.01	0.01	0.01	0.01	0.01	0.01	0.01

Table A.4: Fitting parameters of the polydisperse cylinder model and fitting values for neat and protein-laden Capto S. Lower and upper limits of the fitting range are included. Values that were held fixed during fitting are indicated by an asterisk.

	Neat				Lysozyme			
	20 mM	50 mM	100 mM	200 mM	20 mM	50 mM	100 mM	200 mM
Volume fraction $\varphi$ [-]	0.043	0.049	0.045	0.045	0.148*	0.177*	0.166*	0.150*
Mean cylinder radius $R$ [Å]	50.9	52.0	51.3	51.3	159.8	161.3	150.8	119.6
Radial polydispersity $\sigma$ [-]	0.58	0.57	0.58	0.58	0.33	0.33	0.37	0.45
Cylinder length $L^*$ [Å]	10000	10000	10000	10000	10000	10000	10000	10000
SLD cylinder $\rho_{cyl}$ [ $10^{-6} \text{Å}^{-2}$ ]	2.22*	2.22*	2.22*	2.22*	3.77	3.95	3.92	3.90
SLD solvent $\rho_{solv}$ [ $10^{-6} \text{Å}^{-2}$ ]	6.33	6.33	6.33	6.33	5.36	5.42	5.41	5.54
Background $B$ [ $\text{cm}^{-1}$ ]	0.13	0.15	0.14	0.14	0.33	0.33	0.32	0.30
Lower fitting range* [Å <sup>-1</sup> ]	0.001	0.001	0.001	0.001	0.001	0.001	0.001	0.001
Upper fitting range* [Å <sup>-1</sup> ]	0.5	0.5	0.5	0.5	0.05	0.05	0.05	0.05

	Lactoferrin				mAb			
	20 mM	50 mM	100 mM	200 mM	20 mM	50 mM	100 mM	200 mM
Volume fraction $\varphi$ [-]	0.178*	0.169*	0.116*	0.072*	0.107*	0.156*	0.116*	0.059*
Mean cylinder radius $R$ [Å]	44.4	46.2	49.8	50.5	48.9	12.1	42.9	42.0
Radial polydispersity $\sigma$ [-]	0.56	0.53	0.50	0.55	0.78	0.99	0.51	0.63
Cylinder length $L^*$ [Å]	10000	10000	10000	10000	10000	10000	10000	10000
SLD cylinder $\rho_{cyl}$ [ $10^{-6} \text{Å}^{-2}$ ]	3.60	3.83	3.85	3.09	3.37	4.04	4.16	3.03
SLD solvent $\rho_{solv}$ [ $10^{-6} \text{Å}^{-2}$ ]	4.23	4.78	5.25	5.72	4.84	5.21	5.74	5.90
Background $B$ [ $\text{cm}^{-1}$ ]	0.42	0.42	0.29	0.24	0.38	0.33	0.21	0.19
Lower fitting range* [Å <sup>-1</sup> ]	0.003	0.002	0.002	0.001	0.001	0.002	0.002	0.001
Upper fitting range* [Å <sup>-1</sup> ]	0.04	0.04	0.04	0.04	0.04	0.04	0.04	0.04

## **Appendix B**

### **CONFOCAL FLUORESCENCE MICROSCOPY IMAGES OF ADDITIONAL SAMPLES**

Figure B.1 shows a compilation of maximum-intensity projections of CFM image stacks for Fab1 and mAb1 formulations with different drying processes, sugar-to-protein ratios (S/P) and sugar types (Chapter 3). Importantly, all freeze-dried formulations show a homogeneous protein distribution. As these are maximum-intensity projections, which is virtually a summation of the whole image stack, areas where the particles are thicker in the z-direction do show up as slightly brighter. The bright speck in Figure B.1c is a drop of water that was probably absorbed from the atmosphere by the hygroscopic powder before submersion in immersion oil.

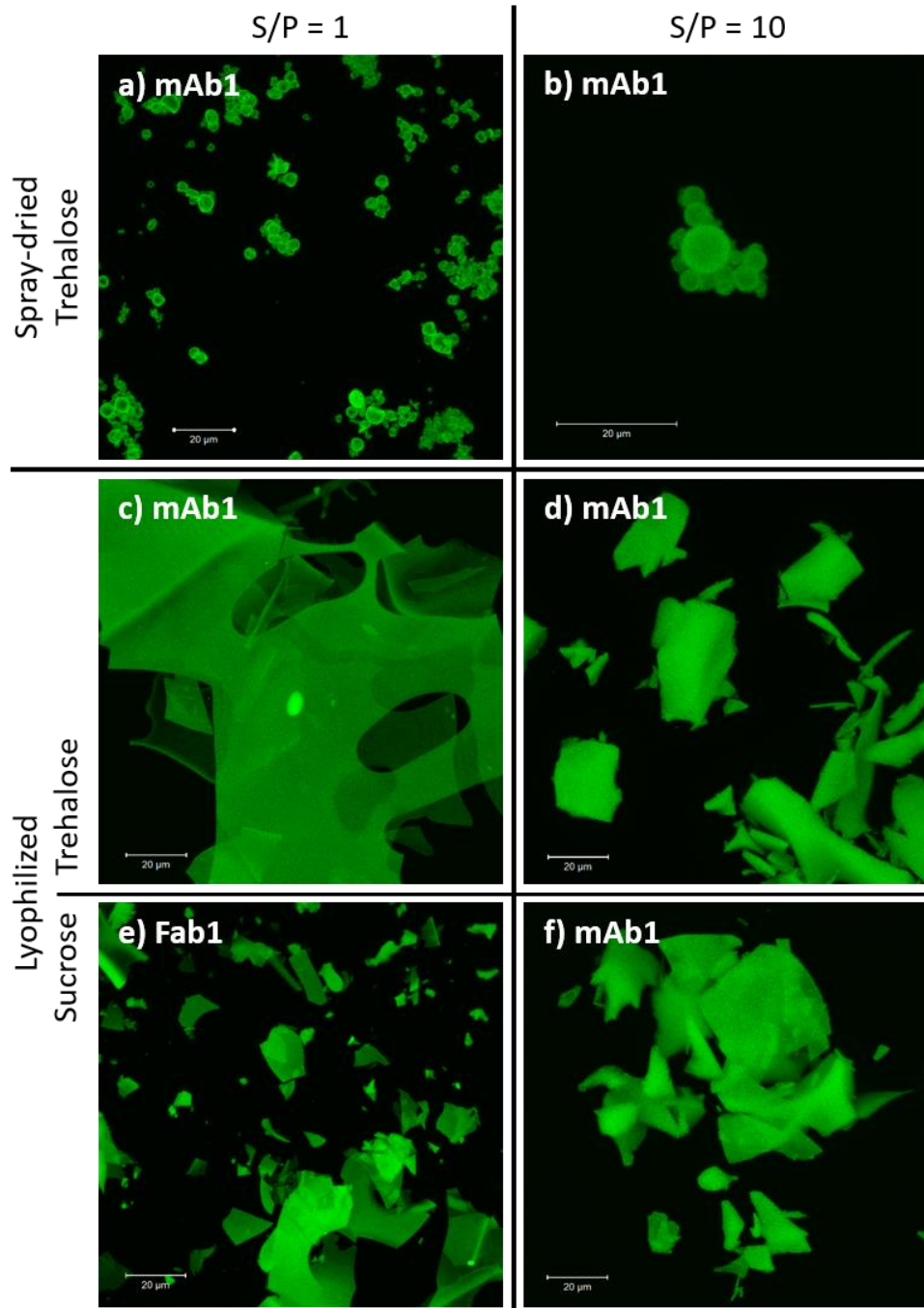


Figure B.1: Maximum-intensity projections of the CFM image stacks for one Fab1 and five mAb1 formulations. Spray-dried formulations show protein-exipient microheterogeneity, while freeze-dried particles show homogeneous distribution.

## Appendix C

### FULL-RANGE SMALL-ANGLE NEUTRON SCATTERING PATTERNS FOR SOLID-STATE FORMULATIONS IN A VAPOR CELL

This appendix contains the small-angle neutron scattering (SANS) patterns over the full  $q$ -range for two formulations: a lyophilized monoclonal antibody (mAb) in deuterated sucrose (Formulation 2, Figure C.1) and a spray-dried fragment antibody (Fab) in trehalose (Formulation 5, Figure C.2). Figure C.1 illustrates that the scattering behavior at low  $q$ -values remains the same throughout the course of the experiment, indicating that the powders retain their solid morphology when exposed to water vapor. Changes in intensity can be attributed to contrast variation due to the uptake of H<sub>2</sub>O or D<sub>2</sub>O. Indeed, compared to the initial scattering intensity (red), the intensity decreases with H<sub>2</sub>O exposure (purple) and increases with D<sub>2</sub>O exposure (blue), as expected from the corresponding scattering length densities. In addition, Figure C.2 highlights that for a spray-dried formulation, no significant microstructural features are observed in the range of 300 to 1600 Å, although spray-dried formulations exhibit microheterogeneity on the particle scale (Figure 3.2). Hence, this particle-scale microheterogeneity does not originate from major changes in protein-scale microstructure, but rather can occur by a redistribution of the excipient between the protein molecules.

Videos of the evolution of the SANS patterns with time for each of the five formulations are available online [100]. In these videos, the dashed lines are guides to the eye.

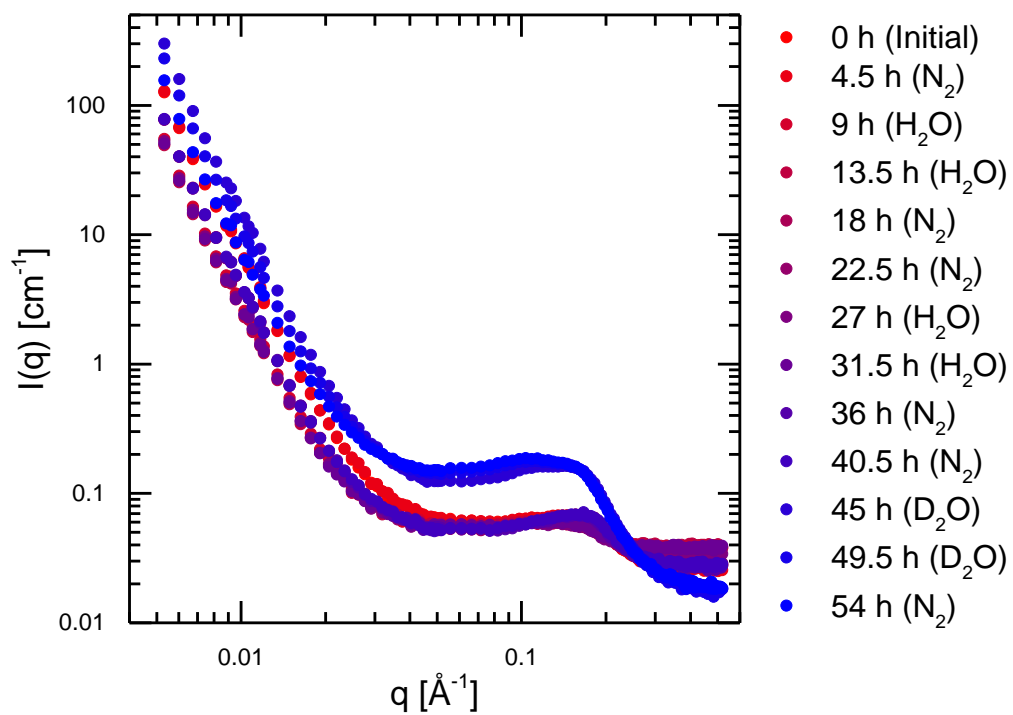


Figure C.1: Full  $q$ -range SANS patterns of a lyophilized mAb in deuterated sucrose (Formulation F2) as a function of time under cycles of alternating nitrogen and water vapor flows.

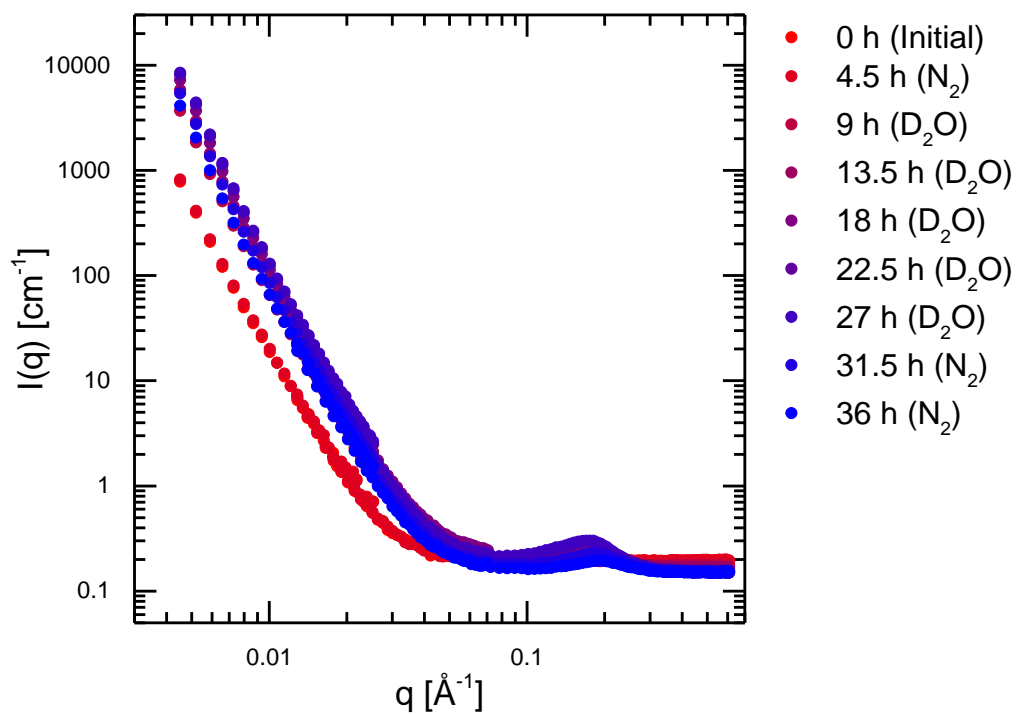


Figure C.2: Full  $q$ -range SANS patterns of a spray-dried Fab in trehalose (Formulation F5) as a function of time under alternating nitrogen and water vapor flows.

## Appendix D

### OPTIMAL PARAMETER VALUES FOR PARALLEL TEMPERING ALGORITHM

This appendix contains additional tables with optimal parameter solutions as obtained from multiple runs of the parallel tempering algorithm (PTA).

Table D.1: Optimal parameter values and corresponding objective functions for the mathematical model fit to the solvent depot data set when seven parameters are fit, as obtained from twenty different runs of the PTA. Red and green highlights indicate the range of the objective function values.

	Drug diffusivity $\left[10^{-16} \frac{\text{m}^2}{\text{s}}\right]$	Water diffusivity $\left[10^{-12} \frac{\text{m}^2}{\text{s}}\right]$	Occlusion radius [ $10^{-6}$ m]	Initial polymer MW [Da]	Polymer MW at release [Da]	Polymer degradation rate constant $\left[\frac{10^{-10}}{\text{s}(\text{kg}/\text{m}^3)}\right]$	Polymer MW SD at release [Da]	Objective Value [-]
Initial	5.00	1.00	1.00	41000	3000	6.00	10000	0.877
Run 1	5.86	1.50	1.01	43630	3855	4.46	9676	0.513
Run 2	6.53	1.52	0.65	43810	2682	4.50	10045	0.495
Run 3	6.16	1.84	0.62	43990	3204	4.49	9981	0.493
Run 4	6.02	2.31	1.25	44280	3496	4.47	10065	0.491
Run 5	5.81	1.95	0.79	44300	3613	4.51	10100	0.492
Run 6	5.67	1.45	2.45	43860	4133	4.50	9583	0.493
Run 7	6.53	1.52	0.65	43810	2682	4.50	10045	0.495
Run 8	6.02	2.31	1.25	44280	3496	4.47	10065	0.492
Run 9	5.81	1.95	0.79	44300	3613	4.51	10100	0.492
Run 10	5.90	2.69	1.24	44330	3555	4.47	10109	0.491
Run 11	5.76	1.60	1.33	44110	3726	4.50	9997	0.493
Run 12	4.84	38.75	0.30	45090	5753	4.47	9550	0.489
Run 13	6.07	2.12	1.16	44230	3323	4.50	10050	0.492
Run 14	6.21	1.90	1.04	44200	2965	4.49	10257	0.493
Run 15	6.23	2.78	1.12	44450	3123	4.48	10178	0.492
Run 16	5.72	1.67	2.21	44150	3894	4.52	9751	0.492

Run 17	6.44	1.90	0.87	44190	2660	4.49	10262	0.493
Run 18	6.79	1.97	0.48	44120	2392	4.48	10203	0.494
Run 19	5.98	2.55	0.53	44320	3311	4.48	10257	0.492
Run 20	5.98	1.64	1.11	44210	3186	4.52	10188	0.493
Average	<b>6.02</b>	<b>3.80</b>	<b>1.04</b>	<b>44200</b>	<b>3430</b>	<b>4.49</b>	<b>10050</b>	
CV ( $\sigma/\mu$ )	<b>7%</b>	<b>217%</b>	<b>51%</b>	<b>1%</b>	<b>21%</b>	<b>0%</b>	<b>4%</b>	

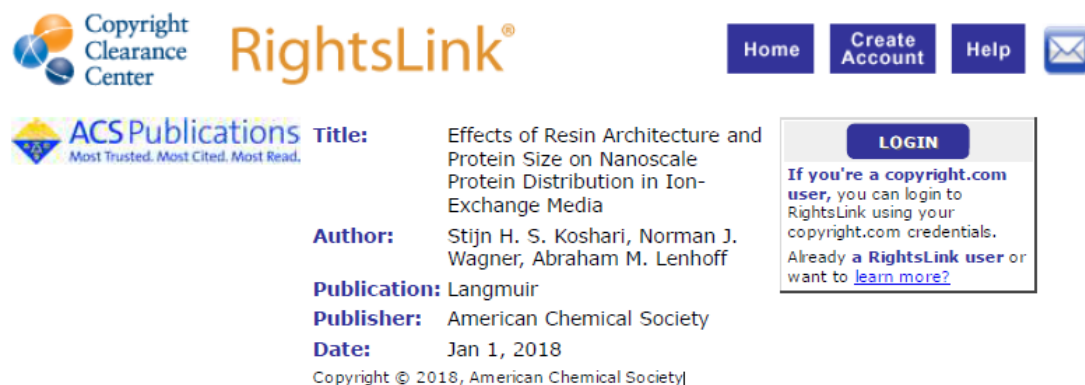
Table D.2: Optimal parameter values and corresponding objective functions for the mathematical model fit to the solvent depot data set when five parameters are fit, as obtained from twelve different runs of the PTA. Red and green highlights indicate the range of the objective function values.

	Drug diffusivity $\left[10^{-16} \frac{\text{m}^2}{\text{s}}\right]$	Initial polymer MW [Da]	Polymer MW at release [Da]	Polymer degradation rate constant $\left[\frac{10^{-10}}{\text{s}(\text{kg}/\text{m}^3)}\right]$	Polymer MW SD at release [Da]	Objective Value [-]
Initial	5.00	41000	3000	6.00	10000	0.877
Run 1	9.24	42870	2676	4.39	8876	0.400
Run 2	9.11	43090	2805	4.42	8767	0.400
Run 3	9.21	42790	2741	4.38	8801	0.400
Run 4	9.18	42960	2501	4.42	9035	0.401
Run 5	8.92	42820	2954	4.38	8894	0.401
Run 6	8.87	42940	2834	4.41	8933	0.401
Run 7	9.07	43000	2677	4.38	9009	0.401
Run 8	9.61	42780	2463	4.37	8849	0.400
Run 9	10.00	42840	2067	4.41	8855	0.400
Run 10	9.67	43120	2317	4.42	8913	0.400
Run 11	8.87	42930	2970	4.36	9006	0.402
Run 12	9.14	42880	2751	4.40	8862	0.401
Average	<b>9.24</b>	<b>42900</b>	<b>2650</b>	<b>4.40</b>	<b>8899</b>	
CV ( $\sigma/\mu$ )	<b>4%</b>	<b>0%</b>	<b>10%</b>	<b>0%</b>	<b>2%</b>	

## Appendix E

### PERMISSIONS

#### E.1 Chapter 2 Reprint Permission



The screenshot shows the Copyright Clearance Center RightsLink interface. At the top left is the Copyright Clearance Center logo. To its right is the RightsLink logo. Further right are navigation buttons for Home, Create Account, Help, and an email icon. Below the logos is the ACS Publications logo with the tagline "Most Trusted. Most Cited. Most Read." The main content area displays the following information:

**Title:** Effects of Resin Architecture and Protein Size on Nanoscale Protein Distribution in Ion-Exchange Media  
**Author:** Stijn H. S. Koshari, Norman J. Wagner, Abraham M. Lenhoff  
**Publication:** Langmuir  
**Publisher:** American Chemical Society  
**Date:** Jan 1, 2018

Below this information is a "LOGIN" button and a text box that reads: "If you're a copyright.com user, you can login to RightsLink using your copyright.com credentials. Already a RightsLink user or want to [learn more?](#)"

At the bottom of the interface, there are two buttons: "BACK" and "CLOSE WINDOW".

#### PERMISSION/LICENSE IS GRANTED FOR YOUR ORDER AT NO CHARGE

This type of permission/license, instead of the standard Terms & Conditions, is sent to you because no fee is being charged for your order. Please note the following:

- Permission is granted for your request in both print and electronic formats, and translations.
- If figures and/or tables were requested, they may be adapted or used in part.
- Please print this page for your records and send a copy of it to your publisher/graduate school.
- Appropriate credit for the requested material should be given as follows: "Reprinted (adapted) with permission from (COMPLETE REFERENCE CITATION). Copyright (YEAR) American Chemical Society." Insert appropriate information in place of the capitalized words.
- One-time permission is granted only for the use specified in your request. No additional uses are granted (such as derivative works or other editions). For any other uses, please submit a new request.

BACK

CLOSE WINDOW

Copyright © 2018 Copyright Clearance Center, Inc. All Rights Reserved. [Privacy statement](#). [Terms and Conditions](#).  
Comments? We would like to hear from you. E-mail us at [customercare@copyright.com](mailto:customercare@copyright.com)

## E.2 Chapter 3 Reprint Permission



RightsLink®

Home

Create Account

Help



**Title:** Characterization of Protein-Excipient Microheterogeneity in Biopharmaceutical Solid-State Formulations by Confocal Fluorescence Microscopy

**Author:** Stijn H. S. Koshari, Jean L. Ross, Purnendu K. Nayak, et al

**Publication:** Molecular Pharmaceutics

**Publisher:** American Chemical Society

**Date:** Feb 1, 2017

Copyright © 2017, American Chemical Society

LOGIN

If you're a **copyright.com user**, you can login to RightsLink using your copyright.com credentials. Already a **RightsLink user** or want to [learn more?](#)

### PERMISSION/LICENSE IS GRANTED FOR YOUR ORDER AT NO CHARGE

This type of permission/license, instead of the standard Terms & Conditions, is sent to you because no fee is being charged for your order. Please note the following:

- Permission is granted for your request in both print and electronic formats, and translations.
- If figures and/or tables were requested, they may be adapted or used in part.
- Please print this page for your records and send a copy of it to your publisher/graduate school.
- Appropriate credit for the requested material should be given as follows: "Reprinted (adapted) with permission from (COMPLETE REFERENCE CITATION). Copyright (YEAR) American Chemical Society." Insert appropriate information in place of the capitalized words.
- One-time permission is granted only for the use specified in your request. No additional uses are granted (such as derivative works or other editions). For any other uses, please submit a new request.

BACK

CLOSE WINDOW

Copyright © 2018 Copyright Clearance Center, Inc. All Rights Reserved. [Privacy statement](#), [Terms and Conditions](#). Comments? We would like to hear from you. E-mail us at [customer@copyright.com](mailto:customer@copyright.com)